2. NUMERICAL TOWING TANK SYMPOSIUM

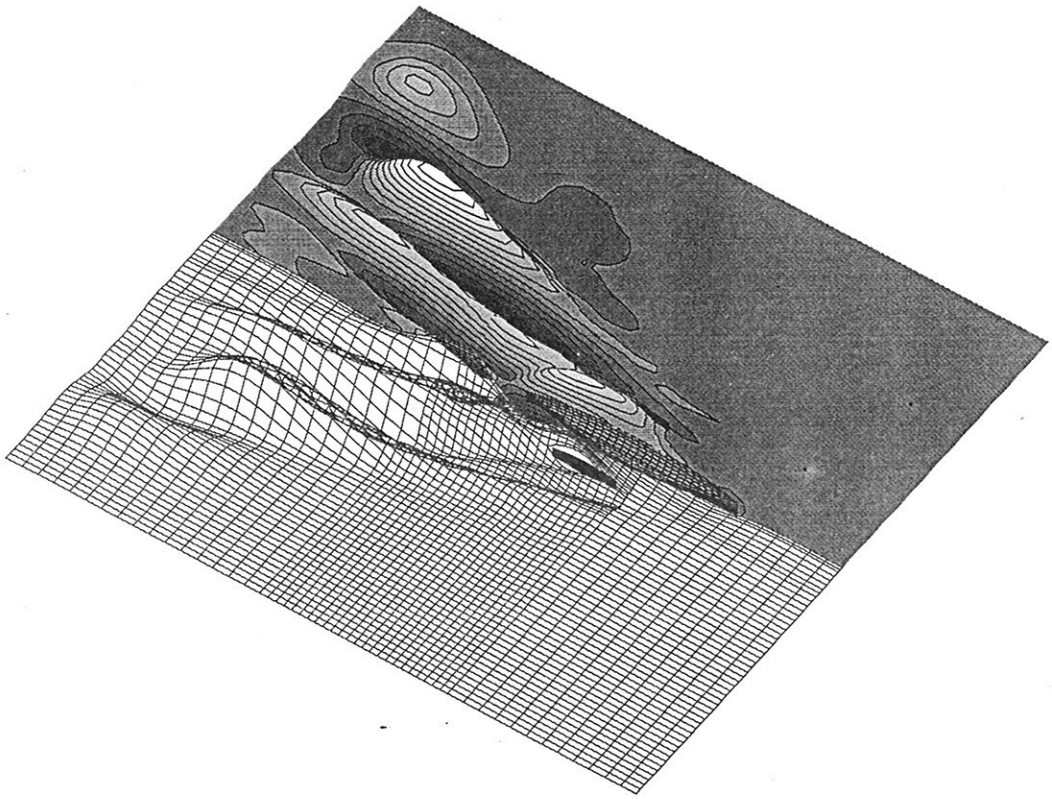

INSEAN

Rome, 2 - 3 August 1999

NuTTS'99

Rome, 2.-3. August 1999

NuTTS'99 was supported by Rolla S.P. and the unbureaucratic decision by an industry sponsor is deeply appreciated.

NuTTS'99 was supported by INSEAN in many ways. Without the financial support, the good scientific contribution and the great help of the 'belle ragazze' this event would not have been possible.

NuTTS'99 was supported by the Office of Naval Research International Field Office Europe under contract number N00014-99-1-1063. The content of the information does not necessarily reflect the position or the policy of the United States Government and no official endorsement should be inferred.

Volker Bertram

Volker Bertram

Application of a RANS-Method to Investigate Scale Effects on the Performance of Modern Propulsion Systems

M. Abdel-Maksoud

1. INTRODUCTION

The prediction of the full scale performance of propellers is of major interest to propulsion system manufacturers. The available experience of scale effects for open water tests is not sufficient for the safe prediction of the performance of modern pod propulsion systems. Experimental investigations of scale effects require full scale tests, which are not only too expensive but also in many cases not available. Furthermore, the results are less informative due to variation of the environmental conditions during the tests. Therefore, the interest of employing viscous flow methods for the analysis of the full scale performance of propulsion systems has increased during the last years.

Improvement of the efficiency of a pod propulsion system requires detailed information on the flow around the propeller and the pod as well as on the interaction between them. The inflow of the propeller is affected by the geometry of the pod. This is not only true for the case where the pod is located in front of the propeller but also, in the reverse arrangement. The thrust distribution on the propeller blades is directly influenced by effect of the inflow velocity distribution caused by the pod. The induced velocities from the propeller change also the flow around the pod. The most important aspects of the interaction between the load distribution on the propeller blades, the propeller inflow and the flow around the pod can be investigated by using a viscous flow method. The application of the fully three-dimensional Reynolds-Averaged Navier-Stokes (RANS) techniques for analysing the flow around ship propellers for open water test conditions was successfully applied by many research groups [1-4]. The propeller flow behind a ship form was investigated by [4]. The calculated effective wake field of a propeller was presented for different angular positions of the propeller blades also in [4].

Many numerical investigations were presented for the application of CFD-methods for computing the full scale flow field around ship forms and propellers. In practice, computations of full scale ship flows are still limited for special applications such as naval and large passenger vessels. The effect of the Reynolds number on the viscous flow around ship forms has been investigated by many scientists, see [5]. The scale effect on a 3 and 5 bladed propeller has been investigated in [6]. The calculated numerical thrust and the torque coefficients of the propeller at full scale were higher than the calculated values for model scale.

The scale effect on the flow around a twin propeller pod system of the SIEMENS SCHOTTEL Propulsor (SSP) is investigated in the framework of the Reynolds-Averaged Navier-Stokes (RANS) equations. The purpose of the present study is not to present a grid converged solution for the propulsion problem, but to demonstrate the applicability of a numerical method for the solution of pod propulsion systems (technology demonstrator).

2. Numerical Method

The numerical computations are carried out for a pod system with two propellers. The calculation domain is divided into one stationary and two rotating parts. The stationary part includes the inflow and outflow areas and the flow around the gondola and the strut. The rotating parts located in front and behind the pod include the blades and the hubs of the propellers. In the stationary part a Cartesian co-ordinate system is employed. The flow around the propellers is computed in a rotating co-ordinate system attached to the propellers. The two rotating parts have the same rotation speed and axis. The RANS equations in a rotating co-ordinate system involve additional terms compared to those in an inertial system. The effects of turbulence are modelled by the standard k-ε model. Wall function boundary conditions are used.

The solver method is based on the conservative finite volume method CFX-TASCflow [7]. The code has been optimised and intensively tested for propeller in uniform, homogeneous flow and in so called "behind ship condition". The investigations are carried out within a joint research project between the Potsdam Model Basin GmbH and AEA Technology GmbH, and is funded by the German Ministry for Education, Research and Technology [4].

The numerical method includes fully conservative stage capabilities to simulate the interaction of the pod and the propeller. The space discretisation is based on a block-structured finite volume grid around the propulsion system and the blades of the propeller. A non-matching sliding grid interface is applied at the interfaces between the numerical grids in the rotating and the stationary frame. The next chapter demonstrates the application of the numerical method for the simulation of flows around pod propulsors.

3. Numerical computation

SCHOTTEL GmbH & Co. KG and SIEMENS AG, Marine Engineering have developed a new podded azimuthing system, which is called SSP. The improved efficiency of the SSP pod systems is achieved by reducing the thrust loading of the propeller. The required thrust is distributed on two propellers, one in front and the other behind the pod. Another advantage of this solution is the reduction of the required propeller diameter. The development of the SSP pod system is supported by extensive numerical and experimental investigations. The aim of the numerical investigation is the computation of the flow around the full scale propulsor. The computations are carried out at model and full scale with different grades of grid refinement (precision). The numerical computations are carried for quasi-stationary (one angular position) and instationary cases. Some of the results of the quasi-stationary case are discussed below.

A 3D solid CAD model was used for the grid generation. Special attention was given to surfaces at the connection between pod and fins as well as between gondola and strut. For model and full scale, a rough and a fine grid was generated. The detailed geometry of all propeller blades was used without any simplification. The coarse numerical grid for the model scale consists of 75 blocks and 530000 control volumes. A high grade of resolution is employed for the full scale numerical grid especially near the wall area. Therefore the number of blocks of the numerical grid were increased to 115, which contain 560 000 control volumes. The fine grid of model and full scale consist of around 90 blocks and more than one million control volumes. The numerical computations of the presented results were carried out using the coarse grid for model and full scale. The Reynolds numbers for model and full scale are 4×10^5 and 2.98×10^7 respectively.

4. Results

The investigation was carried out for one angular position and one operation condition J= 0.633. As shown in Figure 1, one blade of the front propeller is located directly in front of the strut. The rear propeller is running in phase with the front propeller. Therefore, the blade of the rear propeller passes the strut later than the front propeller. As shown below, many details of the flow can be captured by the numerical results in spite of the inadequate grade of refinement of the applied grid.

The calculated thrust coefficient of the full scale for the front and rear propellers are higher than for the model scale. The scale effect of the front propeller is much higher than for the rear propeller due to the intense interaction between the strut and the propeller blades. The calculated thrust coefficient of the rear propeller is 3.5 % higher for the full scale in comparison to the model scale for the operation parameters of this example. The torque coefficient is about 4 % lower than the related value of the model. The total resistance coefficient of the gondola and the strut of the full scale is about 9 % lower than the model value. The stream lines around the SSP model show the effect of the front propeller on the inflow of the rear one, see Figure 1. Figure 2 shows the contour of the axial velocity component in model and full scale in the cross section of the rear propeller. The results show the different thickness of the boundary layer on the gondola and the different velocity distribution between the propeller blades and in the tip vortex area in model and full scale.

5. REFERENCES

1. Abdel-Maksoud, M., Menter, F. R., Wuttke, H.: Viscous Flow Simulations for Conventional and High Skew Marine Propellers, Ship Technology Research, Vol. 45, No. 2, 1998

2. Chen, B. , Stern, F.: Computational Fluid Dynamics for Four-Quadrant Marine Propeller, Proceeding of FED'98, FED SM 98-4872, ASME, 1998

3. Sanchez-Caja, A., Rautaheimo, P., Salminen, E., Siikonen, T.,: Computation of the Incompressible Viscous Flow Around a Tractor Thruster Using a Sliding-Mesh Technique, will be presented in 7th International Conference on Numerical Ship Hydrodynamics, Nantes, France, July 1999.

4. Abdel-Maksoud, M., Menter, F. R., Wuttke, H.: Numerical Computation of the Viscous Flow around the Series 60 C_B = 0.6 Ship with Rotating Propeller, 3rd Osaka Colloquium on Advanced CFD Applications to Ship and Hull Form Design, Osaka, May 1998

5. Watson, S. J., Bull, P. W.: The Scaling of High Reynolds Number Viscous Flow Predictions Using CFD Techniques , 3rd Osaka Colloquium on Advanced CFD Applications to Ship and Hull Form Design, Osaka, May 1998

6. Stainer, M.,: The Application of RANS Code to Investigate Propeller Scale Effects, 22nd Symposium on Naval Hydrodynamics, Washington DC, Aug. 1998

7. Raw, M. J.: A Coupled Algebraic Multigrid Method for the 3D Navier-Stokes Equations in Fast Solvers for the Flow Problems, ed. W. Hackebusch, G. Wittum, Notes on Numerical Fluid Mechanics, Vol. 49, 1995

6. ACKNOWLEDGEMENT

The author would like to thank the Company SCHOTTEL GmbH & Co. KG for the good co-operation and the kind agreement for publishing some results of the numerical investigation.

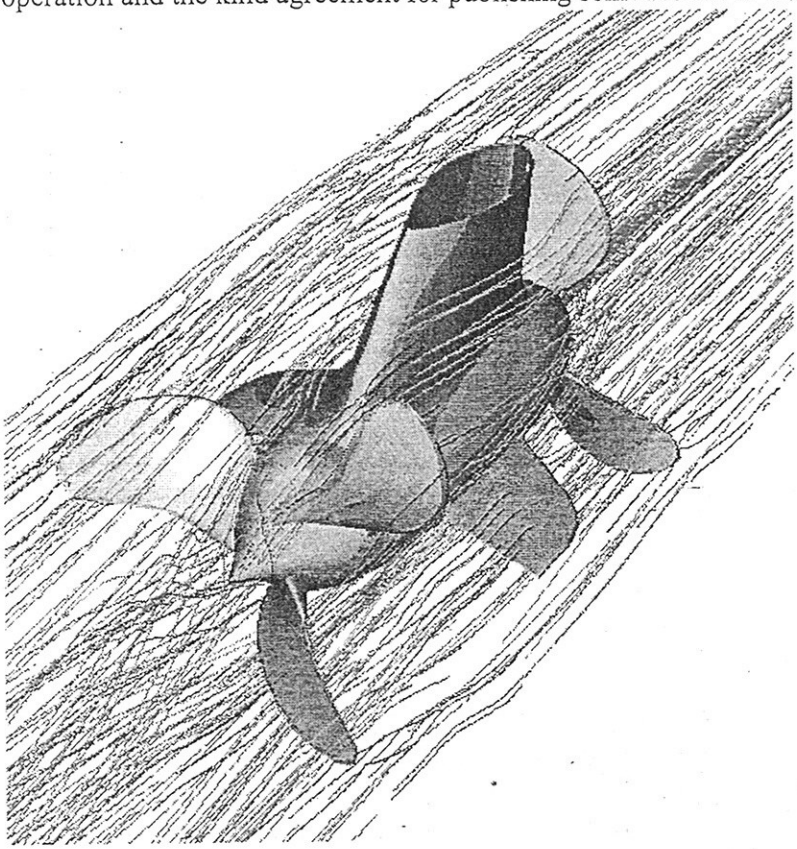

Figure 1: Stream lines around SSP Propulsor

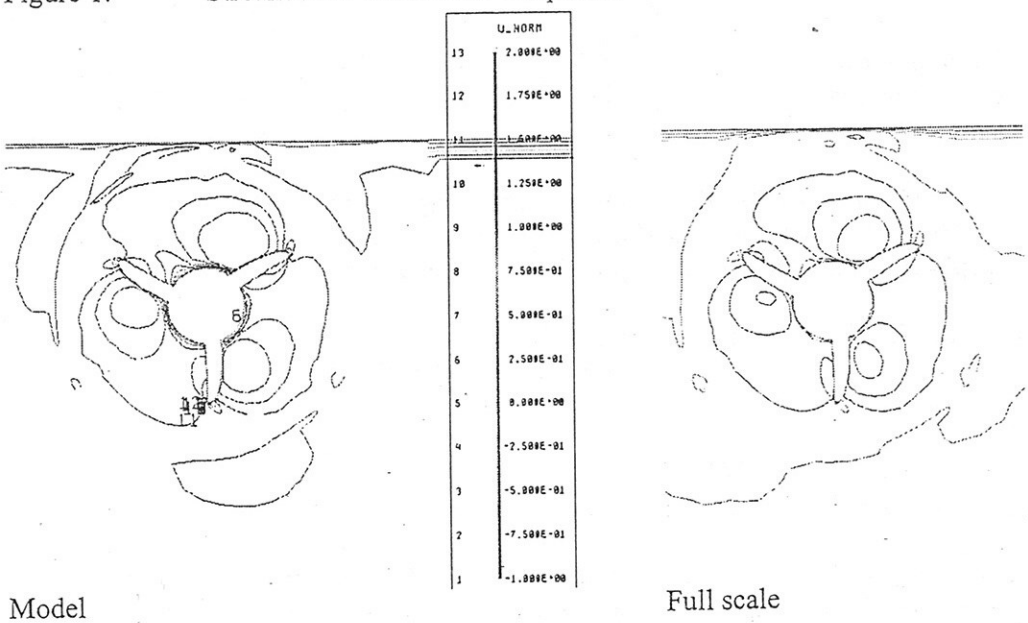

Model Full scale

Figure 2: Velocity distribution in the plane of rear propeller

Parallelization of a panel method in SMP environment

Giorgio Amati * Federico Massaioli † Sergio Parisi ‡

1 Extended Abstract

We present some results concerning the parallelization of a panel method code in a SMP (Symmetric Multi Processor) environment using OpenMP directives.
Panel methods give rise to heavy computational kernels. They are $O(n^2)$ models where n is the number of unknowns, as a consequence it is practically impossible to use a great number of panels on a serial machine. Furthermore in sea-keeping simulations we have to look at different combinations of parameters like Froude number, initial conditions and various time steps. So arises the need to minimize turn around time of every computation.
In the following a very short description of the computational kernels is presented, with a brief description of SMP parallel computing. After that we present a simple way to parallelize a panel method and some results about speedup and efficiency. Finally some concluding remarks will be done.

1.1 Panel method: main computational aspects

Panel methods are numerical schemes used in naval idrodynamics for the simulation of free surface - hull interaction. For a complete description of the scheme used see [1]. A panel method is essentially built from two different computational kernels

- Assembly of the mutual interactions matrix in which the interaction between each panel and the other $n-1$ panels has to be computed.
- Solution of a $n \times n$ linear system.

Both kernels have a $O(n^2)$ computational costs, where n is the number of panels and are apllied to compute source densities and their derivatives for each panel. Table 1 shows how the computing time grows with the number of panels. Moreover a typical sea-keeping problem requires different simulations with various initial conditions and Froude numbers to be completed. Each simulation can lasts about 20-40 hours on a serial machine. This justifies the need of parallel computing in order to reduce elapsed and turn-around time.

1.2 SMP and OpenMP

Symmetric Multi Processors are Shared Memory parallel machine, i.e. each processor can access to every memory location. Technological evolution makes such kind of machines widely available, even in the form of commodity multiprocessor PCs. Moreover this architecture does not require explicit data movement from a processor to an other like in message passing architectures (e.g. cluster of workstation), thus allowing for significant code simplification, better performance and more sophisticated algorithms. On the other hand, technological and economical issues limit the number of available processors (usually less then $32-64$) and care have to be exercised to manage simultaneous accesses and modifications to the same memory location by

*CASPUR - University of Rome *La Sapienza* – *e-mail* g.amati@caspur.it
†CASPUR - University of Rome *La Sapienza* – *e-mail* f.massaioli@caspur.it
‡INSEAN - Italian Ship Model Basin – *e-mail* sergios@rios5.insean.it

different processors (read-write conflicts). It is the programmer's responsibility to correctly sinchronize data access between processors.
For the present work we adopted OpenMP directives [2], an industry standard that hides in an effective manner the complexity of managing more than one independent thread of execution in the same application, simplifies debugging, allows for seamless portability from system to system. The parallel directives are in the form of fortran comments (e.g. C$OMP), so that the parallel code can be used also for serial computing: a standard compiler reads a directive as a comment, while a parallel compiler is able to detect it and to produce parallel a executable. It is important to carefully cathegorize variables, to distinguish between data that are local to each processor (*local variables*: a private copy for each processor) and those common to all processors (*shared variables*: a single copy accessed by every processor).
We also tested a different approach, namely the use of parallel numerical libraries from a serial program. When a program heavily relying on numerical algebra operations calls a standard BLAS routine, a special parallel version can be transparently used if the executable has been linked to a vendor supplied parallel library. Usually, these libraries don't present a good speedup (i.e. the increase of velocity execution using more then 1 processor) but they are very easy to use, even if they actually present some problems of compatibility with OpenMP directives.
Of course, all the burden of parallelization makes sense and is profitable only when applied to a previously optimized code.

1.3 Parallelization in SMP environment

In this section we present and discuss the performances exhibited by two parallel codes. The first one was dominated by the assembly of the interaction matrix, and the parallel version was developed with OpenMP tools. The second code was dominated by the solution of the linear systems, making a "quick and dirty" parallelization using a parallel numerical algebra library appealing. For parallelization with OpenMP KAP/Pro ToolSet from KAI has been used [3]

1.3.1 Code A

In this code the forces between two bodies, moving along a predefined path are computed. At each time-step the matrix of mutual influences must be computed. The routine where the matrix is computed amounts to $\simeq 95\%$ of the total elapsed time. This routine has been easily parallelized with OpenMP.
Resulting speedup ($S(n) \equiv t(1)/t(n)$, where $t(n)$ is the elapsed time using n processor) and efficiency ($E(n) \equiv t(1)/(n * t(n))$) are shown in table 2, together with the theoretical speedup ($S(n)^{th}$). The efficiency decrease with more than 4 processors: this depends on the increasing weight of the serial part of the code as processor number of processors goes up (i.e. Amdahl law). In fact the the serial part, that is essentially the solution of a linear system, becomes more important in a linear way with the number of processors used. Should we need more then $4-6$ processors, we'd have to parallelize also this part, negligible using less processors, spending more time on programming and optimizing.

1.3.2 Code B

In this code we compute separately Pitch, Heave and Surge movements of a hull in plain water in order to calculate the forces acting on it. Here the mutual influences matrix is computed only at the beginning of the simulation and between $85-95\%$ of the elapsed time is spent now on BLAS routines (essentially GEMV) solving a linear system. This routine can be parallelized using parallel BLAS or in a "hand-made" way using OpenMP. Using parallel BLAS 95% of elapsed time is spent in GEMV (both using DEC and SUN SMP machine), while with OpenMP we have used n SAXPY routines instead of one GEMV, dispatching them between the different processors; this section takes about 85% of the elapsed time. The results are shown in tab. 3. It is evident that the speedup tends to saturate for more then 4 processor and in this case vendor GEMV performs better than the our first attempt to a "hand-made" parallelization.
More effort, however, has to be spent in that direction. In fact, present parallel numerical libraries are incompatible with use of OpenMP directives, thus empairing parallelization of the remainder of the code, whose weight on the total elapsed time grows significantly when more processors are used.

n. of panel	time (s)	Ratio
256	32.66	-
1024	584.08	18.2
4096	10490.41	17.9

Table 1: Code A: time spent using different number of panels

n. of Processor	1	2	4	6	8
time	38' 57"	21' 05"	11' 19"	8' 06"	7' 02"
$S(n)$	-	1.85	3.4	4.8	5.5
$S(n)^{th}$	-	1.90	3.48	4.80	5.92
$E(n)$	-	0.92	0.86	0.80	0.69

Table 2: Code A: experimental speedup ($S(n)$), theoretical speedup ($S(n)^{th}$) and efficiency ($E(n)$) for a test case with 8192 panels. It was executed on SUN Enterprise 3500.

1.3.3 Code B: physical results

In order to show the gain of using parallel computing, the code B has been used to compute Pitch, Heave and Surge forces on a hull at three different resolution (690 + 713 panels, 690 + 2852 panels, 2668 + 2976 panels), at tree different Froude number (0.2–0.3–0.4) with fixed and moving hull. A simple snapshot of the results is shown in fig. 1.4. The simulation of the 54 combination of parameters, plus some tests for different dt in order to validate convergence, costs about 3000 hours on a cluster of 4 processor DEC-SMP machine in one month. The same computation on a single processor machine need more then 3 months of sustained computations, showing a very good turn-around time.

1.4 Conclusion

SMP parallelization presents good results on this kind of application. In the present application the need for parallel computing is to reduce elapsed and turn-around time between the simulations and thus can be obtained successfully also with a few processors.
OpenMP directives proved effective, as only 80 directives needed to be added to the original 2000 FORTRAN lines of code A. Moreover using OpenMP we are still able use the new parallel code to produce serial executables. The parallel library approach too demonstrated its effectiveness for codes dominated by numerical algebra operations, giving a parallel application at the cost of a linking phase.
Both approaches are fast and effective, freeing time from software development to concentrate on the physical problem. Unsatisfactory speedups are obtained for more than 4-6 CPUs, depending on the approach. This is due to the fact that some computational steps are intrinsically serial and parallel libraries aren't yet mature. But if we parallelize both kernels, we can reach a better speedup as shown in tab. 4. More work has to be profused on these issues, from programmers, library developers and standardization committees.

References

[1] Colagrossi, A. and Landrini, M. *Fully 3D time domain computations of seakeeping ship.* Proceedings of Second numerical towing tank symposium NuTTS 99, Roma, 1999

[2] http://www.openmp.org/

[3] http://www.kai.com/

n. of Processor	1	2	3	4
time	10' 02"	5' 40"	4' 15"	3' 25"
$S(n)$ (DXMLP)	-	1.77	2.67	2.94
$S(n)^{th}$ (DXMLP)	-	1.90	2.73	3.48
time	10' 42"	6' 54"	5' 19"	4' 46"
$S(n)$ (SP)	-	1.55	2.01	2.24
$S(n)^{th}$ (SP)	-	1.90	2.73	3.48
time	9' 09"	5' 26"	4' 25"	4' 06"
$S(n)$ (OMP)	-	1.68	2.07	2.23
$S(n)^{th}$ (OMP)	-	1.74	2.30	2.75

Table 3: Code B: experimental Speedup, theoretical Speedup and efficiency for a test case with a 1200×1200 matrix ($\simeq 150MB$) on a Compaq 4100 using DXMLP libraries (DXMLP), on a SUN Enterprise 3500 using Sunperf libreries (SP), and "Hand made" parallelization with OpenMP (OMP).

n. of Processor	1	2	4	6	8
time	38' 57"	20' 33"	10' 43"	7' 29"	6' 01"
$S(n)$	-	1.89	3.63	5.27	6.50
$E(n)$	-	0.95	0.91	0.88	0.81

Table 4: Code A: the same for table 2 using "hand made" parallelized BLAS.

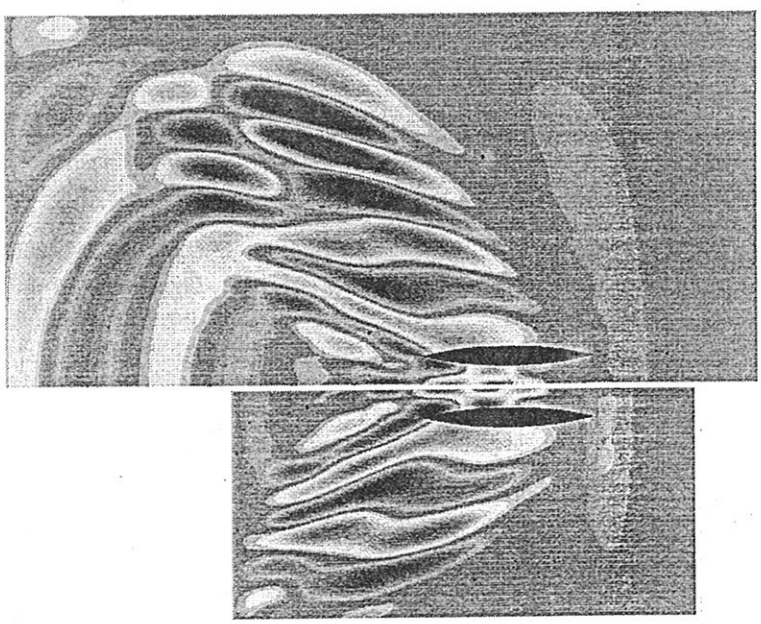

Figure 1: Wave pattern due to the interaction of a ship with an incident wave packet at $Fr = 0.2$ using two different grids.

PREDICTION OF FREE-SURFACE FLOWS WITH BREAKING WAVES

Volker Bertram[1], Samir Muzaferija[2], Milovan Perić[1]

[1] *TU Hamburg-Harburg, Lämmersieth 90, D-22305 Hamburg, Germany*

[2] *ICCM Institute of Computational Continuum Mechanics GmbH, Bramfelder Str. 164, D-22305 Hamburg, Germany*

INTRODUCTION

Free surface flows can be computed by a number of methods if no breaking waves occur; in those situations the methods based on potential flow theory are often quite satisfactory. However, there are many practical situations in which the free surface deforms so severely that classical methods for predicting free-surface flows fail. Examples are breaking bow waves in flows around ships and breaking waves above submerged hydrofoils.

In order to compute free-surface flows with breaking waves, one has to use one of the interface-capturing methods. Examples are: *(i)* the classical VOF-method [1], which computes the flow of water only but allows severe deformation of the free surface, *(ii)* level-set methods [2], which compute the flow of both liquid and gas and use a level-set function which describes the distance from the interface to track the motion of the interface, and *(iii)* methods which consider all fluids involved as one effective fluid with variable properties and solve additional equations for volume concentration of all but one constituent fluid in order to define the composition at any point in space [3,4,5]. The first two classes of methods have problems with situations of non-unique free-surface shape and enclosed pockets of one fluid within the other. The last named class of methods is the most general one as it represents a kind of multi-phase flow model; however, it requires a special care in discretizing and solving the conservation equations for species concentrations.

We describe below briefly the interface-capturing scheme and the underlying finite-volume method used in the present study, followed by examples of computations of flows with wave breaking.

MATHEMATICAL MODEL

The conservation equations for mass, volume concentrations and momentum describe the behavior of a multi-fluid system:

$$\frac{\mathrm{d}}{\mathrm{d}t}\int_V \rho \,\mathrm{d}V + \int_S \rho \mathbf{v}\cdot\mathbf{n}\,\mathrm{d}S = 0\,, \tag{1}$$

$$\frac{\mathrm{d}}{\mathrm{d}t}\int_V c_i \,\mathrm{d}V + \int_S c_i \mathbf{v}\cdot\mathbf{n}\,\mathrm{d}S = 0\,, \tag{2}$$

$$\frac{\mathrm{d}}{\mathrm{d}t}\int_V \rho\mathbf{v} \,\mathrm{d}V + \int_S \rho\mathbf{v}\mathbf{v}\cdot\mathbf{n}\,\mathrm{d}S = \int_S \boldsymbol{T}\cdot\mathbf{n}\,\mathrm{d}S + \int_V \mathbf{f}_\mathrm{b}\,\mathrm{d}V. \tag{3}$$

V is an arbitrary control volume bounded by a closed surface S, ρ is the density, $\mathbf{v}$ is the fluid velocity vector, $\mathbf{n}$ is the unit vector normal to the surface S and directed outwards, c_i is the volume concentration of the ith fluid component, $\boldsymbol{T}$ is the stress tensor, and $\mathbf{f}_\mathrm{b}$ is the resultant body force.

The mixture of fluids is treated as a single effective fluid, with physical properties expressed as a function of the volume concentrations and the physical properties of each fluid component:

$$\rho = \sum_i c_i \rho_i \; ; \quad \mu = \sum_i c_i \mu_i \; ; \quad \sum_i c_i = 1 \tag{4}$$

ρ_i and μ_i are the density and dynamic viscosity of the ith fluid component, respectively.

One should notice that the mathematical formulation of the problem is not limited to any specific number of fluids.

NUMERICAL METHOD

In order to solve the governing equations, the solution domain is first subdivided into an arbitrary number of contiguous control volumes (CVs) or cells. Control volumes can be of an arbitrary polyhedral shape allowing for local grid refinement, sliding grids, and grids with non-matching block interfaces. More details about this finite-volume FV discretization can be found in [6]. Here only the interface-capturing features of the method will be presented.

A successful scheme for interface capturing must exploit the interface sharpening nature of the downwind scheme, it must prevent over- and underflow of cells (it has to be bounded), and it should have a mechanism to avoid alignment of the interface with the numerical grid. The High Resolution Interface Capturing (HRIC) scheme [5] achieves this by a non-linear blend of the upwind (UD) and the downwind (DD) scheme. The UD scheme approximates the cell-face value by the value at the upstream cell center (Fig. 1). It is unconditionally stable and always produces a bounded solution. On the other hand, the DD scheme is an unconditionally unstable scheme that introduces negative numerical diffusion. It approximates the cell-face value by the value at the downstream cell center. The way of blending UD and DD can be analyzed in the Normalized Variable Diagram (NVD) [7]. The local normalized volume fraction $\tilde{c}$ in the vicinity of the cell center C is defined as follows:

$$\tilde{c}(\mathbf{r}) = \frac{c(\mathbf{r}, t) - c_{\mathrm{U}}}{c_{\mathrm{D}} - c_{\mathrm{U}}} \; , \tag{5}$$

where subscripts U and D denote the respective nodes upstream and downstream of the cell center C, and $\mathbf{r}$ is the position vector. The HRIC scheme computes the cell-face value of the normalized volume fraction according to the following expression (Fig. 2):

$$\tilde{c}_{\mathrm{j}} = \begin{cases} \tilde{c}_{\mathrm{C}} & \text{if} \quad \tilde{c}_{\mathrm{C}} < 0 \\ 2\tilde{c}_{\mathrm{C}} & \text{if} \quad 0 \leq \tilde{c}_{\mathrm{C}} < 0.5 \\ 1 & \text{if} \quad 0.5 \leq \tilde{c}_{\mathrm{C}} < 1 \\ \tilde{c}_{\mathrm{C}} & \text{if} \quad 1 \leq \tilde{c}_{\mathrm{C}} \end{cases} \tag{6}$$

In order to prevent an alignment of the interface with the numerical grid because of the use of the downwind discretization [5] , the HRIC scheme corrects the $\tilde{c}_{\mathrm{j}}$ value according to the following expression:

$$\tilde{c}_{\mathrm{j}}^{*} = \tilde{c}_{\mathrm{j}} \sqrt{\cos\theta} + \tilde{c}_{\mathrm{C}} (1 - \sqrt{\cos\theta}) \; . \tag{7}$$

where θ is the angle between the normal to the interface (defined by the gradient of the volume fraction ∇c) and the normal to the cell face (Fig. 1).

The blending of upwind and downwind schemes is dynamic and accounts for the local distribution of the volume fraction. However, if the local Courant number Co is too large, the dynamic nature of the scheme may cause convergence problems. In order to prevent

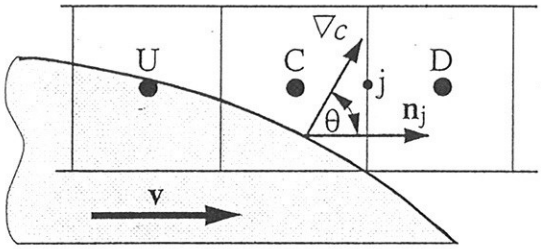

Figure 1: Notation and values used for NVD diagram and HRIC scheme.

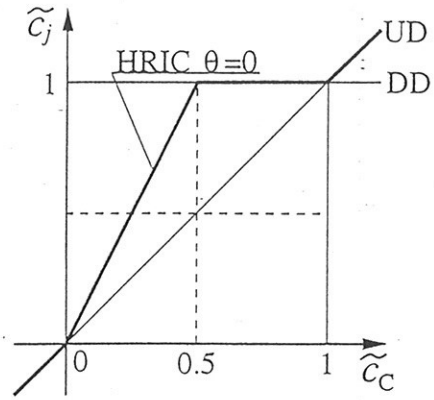

Figure 2: NVD diagram and the HRIC scheme.

this, the HRIC discretization also takes into account the value of Courant number, yielding the cell-face value of the volume fraction according to the following expression:

$$\tilde{c}_j^{**} = \begin{cases} \tilde{c}_j^* & \text{if} \quad \mathrm{Co} < 0.3 \\ \tilde{c}_C & \text{if} \quad 0.7 < \mathrm{Co} \\ \tilde{c}_C + (\tilde{c}_j^* - \tilde{c}_C)\frac{0.7-\mathrm{Co}}{0.7-0.3} & \text{otherwise} \end{cases} \tag{8}$$

Finally, the HRIC cell-face value of c is computed according to Eq.(5) as follows:

$$c_j^{\mathrm{HRIC}} = \gamma\, c_C + (1-\gamma) c_D\,, \qquad \gamma = \frac{(1-\tilde{c}_j^{**})(c_D - c_U)}{c_D - c_C}\,. \tag{9}$$

EXAMPLES

The first example is the flow around the Hamburg Test Case (HTC). The HTC is a container ship which has been selected by ITTC as a standard test case. The ship's geometry is typical for a modern ship hull, with bulbous bows and sterns, and a transom stern. Work is in progress and analyses are expected to be finished by early 2000. Figures 3 and 4 present some preliminary results. Figure 3 shows the distribution of water and air around the ship. Figure 4 shows the elevation of the free surface. Insufficient grid resolution especially in the rear part of the ship causes relatively fast dissipation of waves. At present, new grids with considerably higher resolution are in preparation.

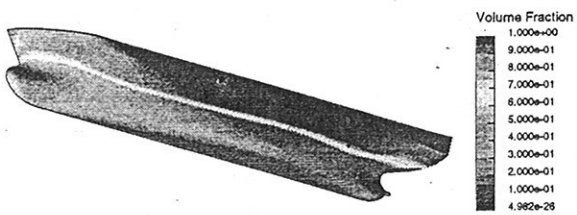

Figure 3: Distribution of air and water along the ship

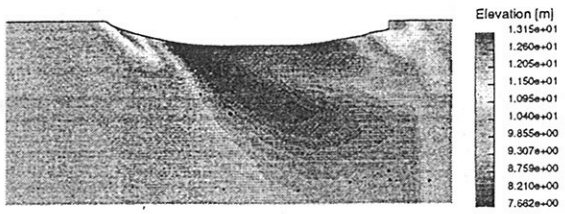

Figure 4: Free-surface elevation

The second test case is the flow around the NACA0012 hydrofoil with chord length 1 m and submergence depth of 0.14 m (measured from the mid-point on the profile nose). The hydrofoil moves at a constant velocity of 1.5 m/s. Figure 5 shows free-surface shapes and

velocity distribution at six time instants during the simulation. One can observe first the buildup of one steep wave (top-left figure). The splash caused by the overturning wave hitting the free surface is seen in the second-left figure. At later times, violent wave breaking with air entrainment takes place in a region extending from the trailing edge to about half chord length behind the foil. Also, the crest of the wave that forms above the leading edge starts breaking at the later stage of the simulation. This case is documented extensively by [8].

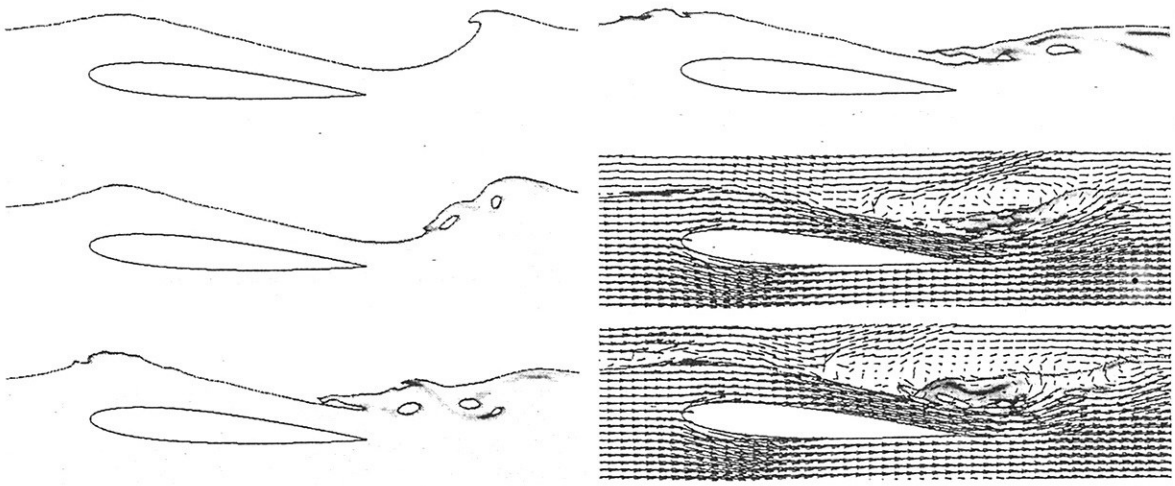

Figure 5: Computed velocity vectors and free-surface shapes at six time instants about one second apart

References

1. C.W. Hirt and B.D. Nichols, "Volume of fluid (VOF) method for the dynamics of free boundaries", *J. Comput. Phys.*, **39**, 201-225, (1981).

2. S. Osher and J.A. Sethian, "Fronts propagating with curvature-dependent speed: algorithms based on Hamilton-Jacobi formulations", *J. Compt. Phys.*, **79**, (1988).

3. B. Lafaurie, C. Nardone, R. Scardovelli, S. Zaleski, and G. Zanetti, "Modeling merging and fragmentation in multiphase flows with SURFER", *J. Comput. Phys.*, **113**, 134–147, (1994).

4. O. Ubbink, Numerical prediction of two fluid systems with sharp interfaces, PhD thesis, University of London, 1997.

5. S. Muzaferija, and M. Perić, "Computation of free surface flows using interface-tracking and interface-capturing methods", chap. 3 in O. Mahrenholtz and M. Markiewicz (eds.), *Nonlinear Water Wave Interaction*, Computational Mechanics Publications, Southampton, 1998.

6. I. Demirdžić, S. Muzaferija and M. Perić, "Advances in computation of heat transfer, fluid flow, and solid body deformation using finite volume approaches", in W.J. Minkowycz, E.M. Sparrow (Editors), *Advances in Numerical Heat Transfer*, chap. 2, Taylor and Francis, New York, 1996.

7. B.P Leonard, "Bounded higher-order upwind multidimensional finite-volume convection-diffusion algorithms", in W.J. Minkowycz, E.M. Sparrow (eds.), *Advances in Numerical Heat Transfer*, chap. 1, pp. 1–57, Taylor and Francis, New York, 1996.

8. R. Azcueta, S. Muzaferija, M. Perić and S.-D. Yoo, "Computation of flows around hydrofoils under the free surface", *Num. Ship Hydrodyn. Conf.*, Nantes, 1999.

Wave pressure computations for a VLCC in regular waves

Volker Bertram, INSEAN
Hironori Yasukawa, Mitsubishi Heavy Industries

Bertram (1998) described a fully three-dimensional ship seakeeping method that considers the steady flow contribution completely (within the framework of potential flow) and linearises the unsteady flow contribution with respect to wave height around the steady flow (including steady wave system, steady trim and sinkage of ship). The theory is also briefly described in Bertram and Yasukawa (1999).

The Rankine Singularity Method (RSM) employs special elements for the seakeeping computations. 'Jensen panels' are used on the hull which allow the evaluation of first-order panels using only point source evaluation. Desingularised point source clusters are used for the free surface. The radiation condition (waves propagate only downstream) is enforced using the shifting technique, Bertram (1990). This technique is simple to implement and free of numerical damping (shown for steady linear free-surface problems and plausibly assumed for quasi-steady seakeeping computations). However, theoretically for $\tau < 0.25$ it is not applicable, as then also significant waves may propagate upstream. Iwashita and Ito (1998) concluded that for seakeeping computations in the frequency domain a practical limit appears to be $\tau = 0.5$ as then results for added mass and damping began to disagree noticeably with experimental values in a benchmark test.

So far, applications of the present RSM were shown only for relatively high Froude numbers, which for most angles of encounters and wave lengths of interest result in sufficiently high τ values. For these cases, good agreement with experiments for motions was demonstrated, Bertram (1998). Numerical studies showed that the influence of the steady flow on the results for motions is significant, for moderate wave lengths, but negligible for short and long waves. This was explained by purely numerical investigations of local pressures. A research cooperation allowed now to investigate local pressures for a VLCC, Table I, at $F_n = 0.131$. The exact geometry of the test case is confidential. The pressures are the amplitudes of the pressure fluctuation, i.e. pressures without hydrostatic and steady hydrodynamic pressures.

The tanker was discretised using 495 elements. First the steady fully nonlinear wave resistance problem was solved. The grid on the free-surface was generated using the 'cut-out' technique. This technique generates a structured grid consisting of rectangular elements. Elements which are partially or totally inside the hull are then eliminated and then the shifting technique is applied. This technique is known to give better results for full hulls than streamlining a grid around the hull. The fully nonlinear method used 3 iterations which reduced the error at the free surface by 4 orders of magnitude.

The same grid for the hull was employed for the seakeeping computations (at the dynamic trim and sinkage). Pressure integrations considered only the area submerged in the steady case. The free surface in the seakeeping computations was discretised with typically 1400 elements. Again the 'cut-out' technique was employed and the steady results interpolated from the 'steady' grid to the 'unsteady' grid. Test computations for two wave lengths with free-surface grids involving approximately 4200 elements yielded results that were only 5% different. This may be interpreted as that the coarser discretisation is sufficient.

The computational results are compared to measurements of Tanizawa et al. (1993) and MHI strip method results. The strip method is a standard STF method with Lewis section representation. The results include motions and pressures on the hull at a location $x = -0.078 L_{pp}$ (23.95m behind amidships). The motions agree rather well for both head sea and oblique sea with $\mu = 150°$, Figs.1 and 2. However, strip method also predicts heave and pitch motions well. In fact, for long waves strip methods gives better results than the RSM. This is not surprising. Strip methods are known to predict heave and pitch motions well for usual ships and ship speeds. The present RSM

uses the shifting technique which deteriorates in performance for $\tau < 0.4...0.5$. Sway and yaw are also well predicted, the maximum of the roll motion is underpredicted. This may be due to the deterioration of the shifting technique, as for a fast containership with $F_n = 0.275$ Bertram (1998) obtained significant overprediction for roll resonance as expected for a method that does not include empirical corrections for nonlinear roll damping.

Figs.3 and 4 compare pressures. Starboard is the weather side. For head waves the computed pressures are of course symmetrical to the midship plane (90°). One point on the port side was then plotted on its corresponding position on the starboard side. Pressures computed by the RSM agree well with measured pressures for $\lambda/L < 1.25$ for $\mu = 180°$ and $\lambda/L < 1.0$ for $\mu = 150°$. These limits correspond for the investigated low Froude number to τ-values around 0.35...0.4. For short waves, the computations underpredict the pressures at the bottom of the ship compared to measurements. However, as the pressures should decay exponentially with depth like all wave effects, for short waves the near-zero values of the computation appear to be more plausible and we assume that they reflect in this case reality better than the measured values. For waves of moderate length $0.5 < \lambda/L < 0.75$, measured and computed pressures at the ship bottom agree well. The strip method results for pressures are significantly worse, especially for short waves $\lambda/L = 0.3$ where diffraction effects are stronger than radiation effects.

In summary, the RSM predicted pressures and motions well, the strip method predicted pressures badly, but motions well. The RSM is currently limited in practice to approximately $\tau > 0.4$. Unless techniques are developed to extend it to smaller τ-Values, the RSM will remain a research tool of limited functionality. We see hybrid methods matching an inner RSM solution to an outer Green function method or Fourier-Kochin solution as most promising approach to extend the method to low τ-values, but at present no such research is planned due to lack of funds.

Table I: Test case VLCC

L_{pp}	307.00	m	KG	15.17	m	k_y	19.193	m
B	54.00	m	x_g	10.045	m	k_y	73.987	m
T	19.50	m	z_g	4.333	m	k_z	76.750	m
C_B	0.813		k_x			k_{xz}	0	m

Acknowledgement

Special thanks to Shuji Mizokami and 'Cowboy' Tanaka in preparing the results.

References

BERTRAM, V. (1990), *Fulfilling open-boundary and radiation condition in free-surface problems using Rankine sources*, Ship Technology Research 37, pp.47-52

BERTRAM, V. (1998), *Numerical investigation of steady flow effects in 3-d seakeeping computations*, 22. Symp. Naval Hydrodyn., Washington

BERTRAM, V.; YASUKAWA, H. (1999), *Added resistance for a fully three-dimensional ship seakeeping method*, NuTTS'99, Rome

IWASHITA, H.; ITO, A. (1998), *Seakeeping computations of a blunt ship capturing the influence of the steady flow*, Ship Technology Research 45, pp.159-171

TANIZAWA, K.; TAGUCHI, H.; SARUTA, T.; WATANABE, I. (1993), *Experimental study of wave pressure on VLCC running in short waves*, J. Soc. Nav. Arch. Japan 174, pp.233-242

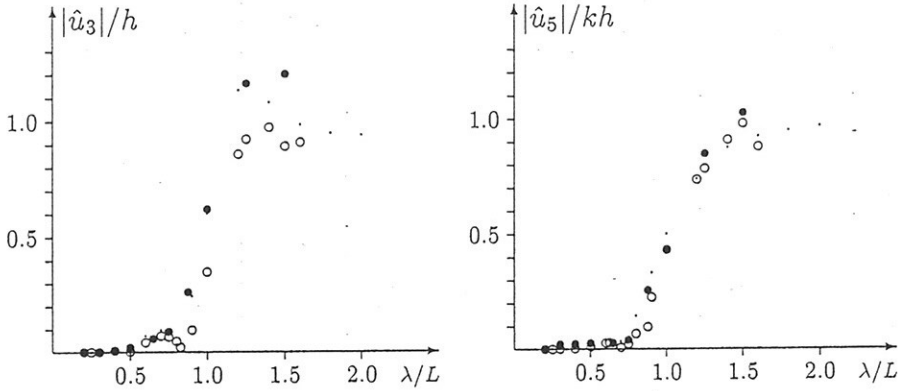

Fig.1: Motions for VLCC, $F_n = 0.131$, $\mu = 180°$; • experiment, ○ RSM, · strip method

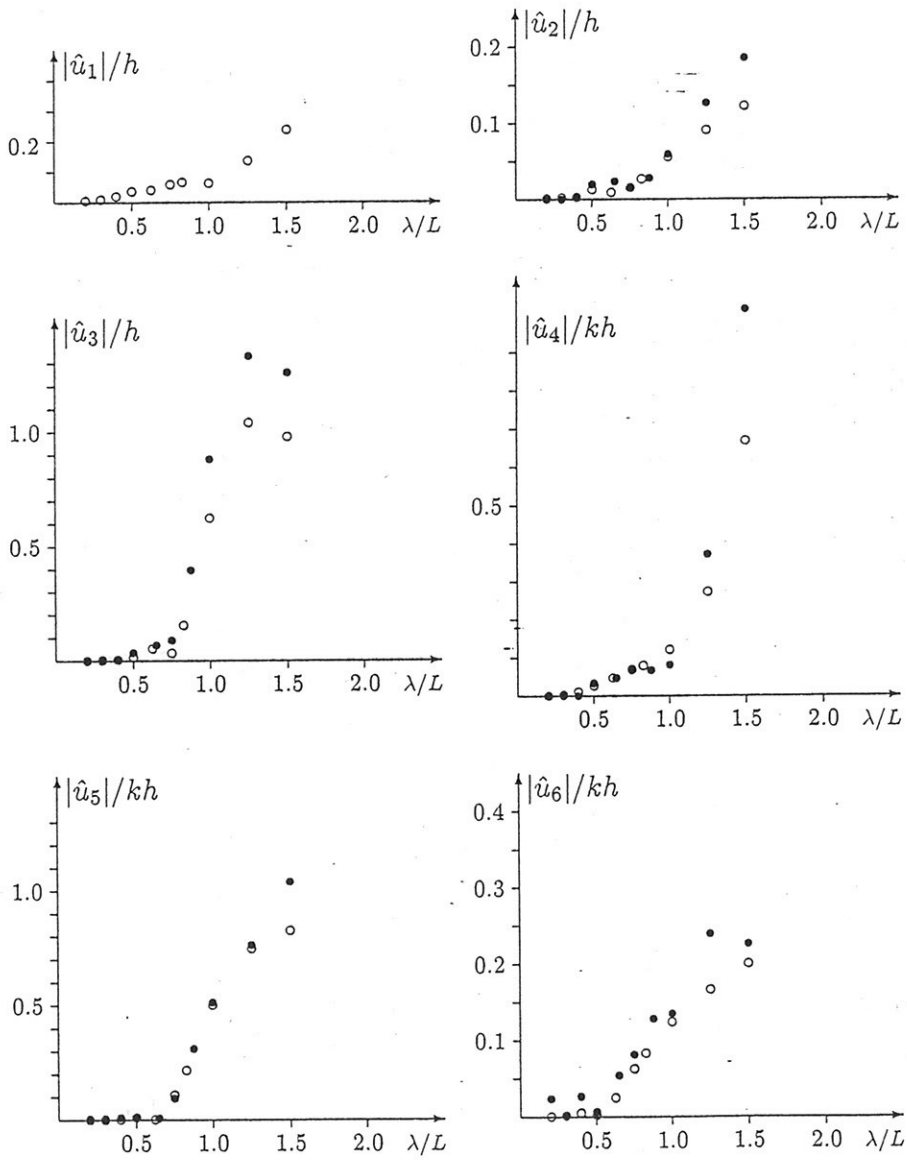

Fig.2: Like Fig.1, but for $\mu = 150°$

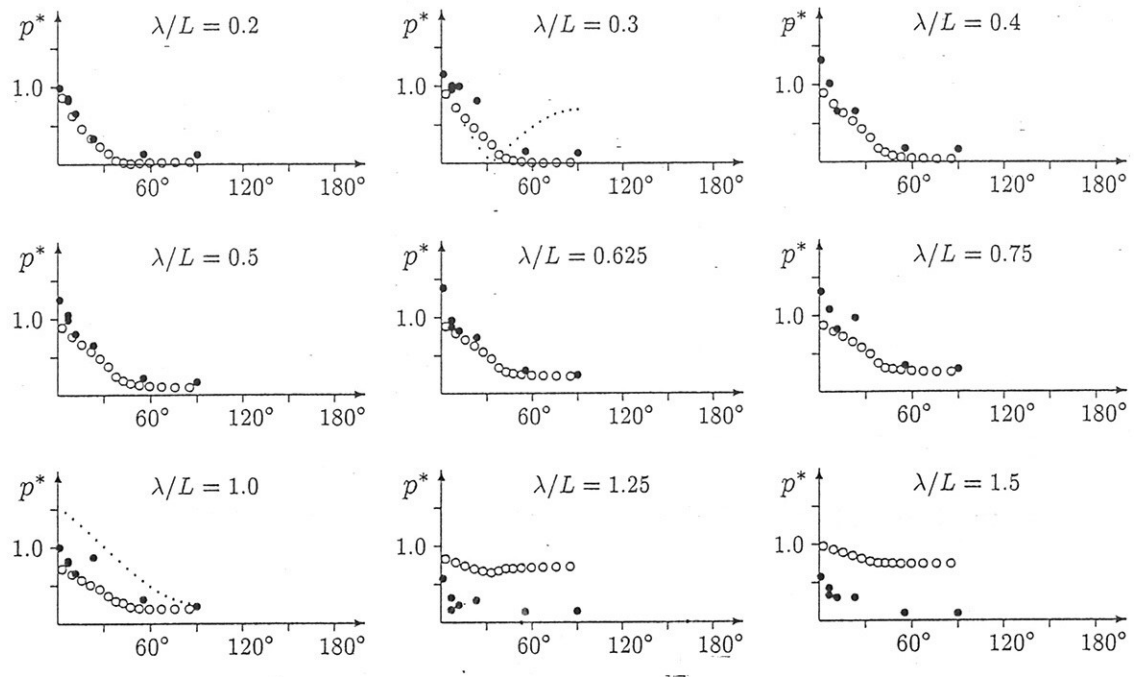

Fig.3: VLCC, $F_n = 0.131$, $\mu = 180°$; unsteady pressure $p^* = |\hat{p}^{(1)}|/(\rho g h)$ at $x = -0.078 L_{pp}$ plotted over circumference angle; 90° = bottom, 0° starboard CWL; • exp., ○ RSM, · strip method

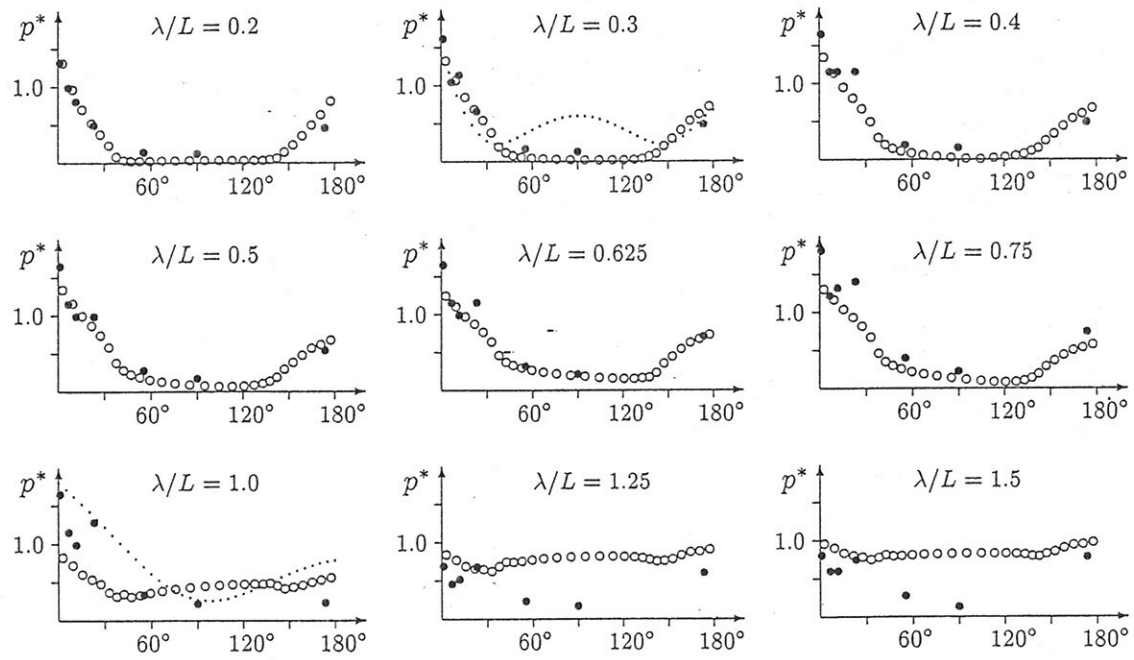

Fig.4: Like Fig.3, but for $\mu = 150°$

Added Resistance for a Fully Three-Dimensional Ship Seakeeping Method

Volker Bertram, INSEAN
Hironori Yasukawa, Mitsubishi Heavy Industries

Bertram (1998) described a fully three-dimensional ship seakeeping method that considers the steady flow contribution completely (within the framework of potential flow) and linearizes the unsteady flow contribution with respect to wave height around the steady flow (including steady wave system, steady trim and sinkage of ship). The formula for added resistance given in Bertram (1998a) contained an error in the contribution of the line integral term. This will be corrected here.

The theory for the determination of the linear RAOs for motions is only very briefly outlined here to the extent necessary for understanding the added resistance formula. Details are given in Bertram (1998a).

We consider a ship moving with mean speed U in a harmonic wave of small amplitude h with $\tau = U\omega_e/g > 0.25$. ω_e is the encounter frequency, $g = 9.81\mathrm{m/s}^2$. All coordinate systems here are right-handed Cartesian systems. The inertial $Oxyz$ system moves uniformly with velocity U. x points in the direction of the body's mean velocity U, z points vertically downward. The $\underline{Oxyz}$ system is fixed at the body and follows its motions. u_i $(i = 1...6)$ denotes the body motions. $\alpha_i = u_{i+3}$ $(i = 1...3)$ denotes just the rotational motions.

A perturbation formulation for the potential is used: $\phi^{total} = \phi^{(0)} + \phi^{(1)} + h.o.t.$
$\phi^{(0)}$ is the part of the potential which is independent of the wave amplitude h (Solution of the steady wave-resistance problem determined in fully nonlinear wave-resistance code.) $\phi^{(1)}$ is proportional to h. Terms proportional to higher powers of h are neglected. The potential and the free-surface elevation ζ are then:

$$\phi^{total}(x,y,z;t) = \phi^{(0)}(x,y,z) + \phi^{(1)}(x,y,z;t) = \phi^{(0)}(x,y,z) + Re(\hat{\phi}^{(1)}(x,y,z)e^{i\omega_e t}) \quad (1)$$

$$\zeta^{total}(x,y;t) = \zeta^{(0)}(x,y) + \zeta^{(1)}(x,y;t) = \zeta^{(0)}(x,y) + Re(\hat{\zeta}^{(1)}(x,y)e^{i\omega_e t}) \quad (2)$$

Correspondingly the symbol $\hat{}$ is used for the complex amplitudes of all other first-order quantities, such as motions, forces, pressures, etc. $\omega_e = |\omega - kU\cos\mu|$ the frequency of encounter. k is the wave number. $\omega = \sqrt{gk}$ is the frequency of the incident wave. The superposition principle can be used within a linearized theory. Therefore the radiation problems for all 6 degrees of freedom of the rigid-body motions and the diffraction problem are solved separately. The total solution is a linear combination of the solutions for each independent problem. The harmonic potential $\phi^{(1)}$ is divided into the potential of the incident wave ϕ^w, the diffraction potential ϕ^d, and 6 radiation potentials. It is convenient to divide ϕ^w and ϕ^d into symmetrical and antisymmetrical parts ($\phi^{w,s}$, $\phi^{w,a}$ for ϕ^w; $\phi^7 + \phi^8$ for ϕ^d) to take advantage of geometrical symmetry:

$$\phi^{(1)} = \phi^{w,s} + \phi^{w,a} + \sum_{i=1}^{6} \phi^i u_i + \phi^7 + \phi^8 \quad (3)$$

The linearized potential of the incident wave is:

$$\phi^w = Re(-\frac{igh}{\omega} e^{-ik(x\cos\mu - y\sin\mu) - kz} e^{i\omega_e t}) = Re(\hat{\phi}^w e^{i\omega_e t}) \quad (4)$$

The following abbreviations are useful: $\vec{a}^{(0)} = (\nabla\phi^{(0)}\nabla)\nabla\phi^{(0)}$, $\vec{a}^g = \vec{a}^{(0)} - \{0,0,g\}^T$, $B = -\frac{1}{a_3^g}\frac{\partial}{\partial z}(\nabla\phi^{(0)}\vec{a}^g)$. The linearized free-surface condition at $z = \zeta^{(0)}$ is:

$$(-\omega_e^2 + Bi\omega_e)\hat{\phi}^{(1)} + ((2i\omega_e + B)\nabla\phi^{(0)} + \vec{a}^{(0)} + \vec{a}^g)\nabla\hat{\phi}^{(1)} + \nabla\phi^{(0)}(\nabla\phi^{(0)}\nabla)\nabla\hat{\phi}^{(1)} = 0 \quad (5)$$

The linearized time-harmonic free-surface elevation is:

$$\zeta^{(1)} = -\frac{\phi_t^{(1)} + \nabla\phi^{(0)}\nabla\phi^{(1)}}{a_3^g} \quad (6)$$

The hull boundary condition at average steady hull position $\underline{S}(\vec{\underline{x}}) = 0$ is:

$$\underline{\vec{n}}\nabla\hat{\phi}^{(1)} + \hat{\vec{u}}(\vec{m} - i\omega_e\underline{\vec{n}}) + \hat{\vec{\alpha}}(\underline{\vec{x}} \times (\vec{m} - i\omega_e\underline{\vec{n}}) + \underline{\vec{n}} \times \nabla\bar{\phi}^{(0)}) = 0 \tag{7}$$

$\underline{\vec{n}}$ is the inward unit normal vector. The m-terms are $\vec{m} = (\underline{\vec{n}}\nabla)\nabla\phi^{(0)}$.

Diffraction and radiation problems for unit amplitude motions are solved independently in a collocation scheme using first-order panels and the same hull grid as for the solution of the fully nonlinear wave-resistance problem. All relevant quantities on the free-surface are interpolated from the 'steady' grid to the 'time-harmonic' grid. After the potential $\hat{\phi}^i$ $(i = 1...8)$ have been determined, only the motions u_i remain as unknowns. These are determined in principle from the 'ansatz' $F = m \cdot a$ (as vector equations in 6 degrees of freedom). This yields a system of equations in $\hat{u}_i$ which is quickly solved using Gauss elimination.

Following a similar approach as for the first-order forces, a formula for the added resistance can be derived that uses only quantities computed so far. The added resistance is the negative time-averaged value of the x-component of the second-order force. If t_1 and t_2 are time-harmonic quantities, the time-average of $t_1 t_2$ is $\frac{1}{2}Re(\hat{t}_1\hat{t}_2^*)$, where $\hat{t}_2^*$ is the conjugate complex of $\hat{t}_2$.

One contribution to this force is the pressure integral over the average wetted surface where only second-order terms of the integrand are retained:

$$T_1 = \overline{\int_{\underline{S}^{(0)}} \left[p^{(1)} + \nabla p^{(0)}(\vec{\alpha} \times \vec{\underline{x}} + \vec{u})\right](\vec{\alpha} \times \underline{\vec{n}})_1 + \left[p^{(2)} + \nabla p^{(1)}(\vec{\alpha} \times \vec{\underline{x}} + \vec{u})\right] \underline{n}_1 \, d\underline{S}} \tag{8}$$

$p^{(0)} = -\rho\left(\frac{1}{2}(\nabla\phi^{(0)}(\vec{x}))^2 - \frac{1}{2}U^2 - gz\right)$, $\nabla p^{(0)} = -\rho\vec{a}^g$, $p^{(1)} = -\rho\left(\nabla\phi^{(0)}\nabla\phi^{(1)} + \phi_t^{(1)}\right)$,
$p^{(2)} = -\rho\frac{1}{2}(\nabla\phi^{(1)})^2$
(A term containing the time-derivative of the second-order potential vanishes in the time-average.)

The first part of the integral yields:

$$\overline{\int_{\underline{S}^{(0)}} \left[p^{(1)} + \nabla p^{(0)}(\vec{\alpha} \times \vec{\underline{x}} + \vec{u})\right](\vec{\alpha} \times \underline{\vec{n}})_1 \, d\underline{S}} = \tag{9}$$

$$\frac{1}{2}Re\{mg\hat{\alpha}_1\hat{\alpha}_3^* - m\omega_e^2(\hat{\alpha}_2^*(\hat{u}_3 - \hat{\alpha}_2\underline{x}_g) - \hat{\alpha}_3^*(\hat{u}_2 + \hat{\alpha}_3\underline{x}_g - \hat{\alpha}_1\underline{z}_g))\}$$

$$\nabla p^{(1)} = -\rho(\nabla\phi_t^{(1)} + \nabla(\nabla\phi^{(0)}\nabla\phi^{(1)})) \tag{10}$$

The second derivatives of the potential on the hull are neglected (due to 'desperation' rather than physical insight.)

Another contribution to the longitudinal time-averaged pressure force stems from the difference between average and instantaneous wetted surface $\triangle S$:

$$T_2 = \overline{\int_C \int_0^Z \left[p^{(0)} + p^{(1)} + \nabla p^{(0)}(\vec{\alpha} \times \vec{\underline{x}} + \vec{u})\right] \underline{n}_1 \, dz' \, dc} \tag{11}$$

C is the vertical projection of the steady wave profile. This modified waterline contour accounts also for steady trim and sinkage and differs usually somewhat from the still waterline contour. z' is a vertical coordinate with origin at the height of the steady surface. Z is the first-order difference between average (steady) and instantaneous wave profile on the hull:

$$Z = \zeta^{(1)} - (u_3 - u_5\underline{x} + u_4\underline{y}) = \tag{12}$$

with $\zeta^{(1)} = p^{(1)}/(\rho a_3^g)$. Developing the pressure about the steady (mean) position, using that the pressure is zero at the free surface, and retaining only second-order terms yields:

$$T_2 = \overline{\int_C \left(\frac{1}{2} p_z^{(0)} Z^2 + [p^{(1)} + \nabla p^{(0)} (\vec{\alpha} \times \vec{\underline{x}} + \vec{u})] Z \right) \underline{n}_1 \, dc} \tag{13}$$

The added resistance is accordingly found with (8) and (13) as $R_{aw} = -(T_1 + T_2)$:

$$\begin{aligned} R_{aw} \;=\; & -\tfrac{1}{2} Re\{ \int_C \left(\tfrac{1}{2} p_z^{(0)} \hat{Z} + \hat{p}^{(1)} + \nabla p^{(0)} (\hat{\vec{\alpha}} \times \vec{\underline{x}} + \hat{\vec{u}}) \right) \hat{Z}^* \underline{n}_1 \, dc \\ & + \int_{\underline{S}^{(0)}} \left[-\tfrac{\varrho}{2} \nabla \hat{\phi}^{(1)} \nabla \hat{\phi}^{(1)*} + \nabla \hat{p}^{(1)*} (\hat{\vec{\alpha}} \times \vec{\underline{x}} + \hat{\vec{u}}) \right] \underline{n}_1 \, d\underline{S} \\ & + mg \hat{\alpha}_1 \hat{\alpha}_3^* - m\omega_e^2 (\hat{\alpha}_2^* (\hat{u}_3 - \hat{\alpha}_2 \underline{x}_g) - \hat{\alpha}_3^* (\hat{u}_2 + \hat{\alpha}_3 \underline{x}_g - \hat{\alpha}_1 \underline{z}_g)) \} \end{aligned} \tag{14}$$

All pressure integral are evaluated numerically over the starboard half only and multiplied by 2 for symmetrical/symmetrical and antisymmetrical/antisymmetrical pressure-normal combinations only. (Antisymmetrical/symmetrical combinations yield zero contributions.)

We show here applications to the ITTC standard test case S-175 containership in head seas. Computations are compared to experiments of Mitsubishi Heavy Industries. Fig.1 shows results for $F_n = 0.25$ and Fig.2 for $F_n = 0.3$. For all three motions the agreement is very good. In fact, the computational results for heave for long waves appear to be more plausible, as they tend as expected monotonously to 1. The slight overshoot in the maximum of heave motion could be due to nonlinear damping effects in the experiments. For $F_n = 0.275$, Bertram (1998) showed that the phase information is also correctly captured, at least for wave lengths where the RAOs are not approximately zero. The added resistance, however, is computed completely wrong for the high Froude number. For $F_n = 0.25$, the agreement appear better, but the added resistance for longer waves is several orders of magnitude larger than measured. There are various possible explanations:

1. The mathematical formulation may be wrong. We detected one error in the formulation given in Bertram (1998). Perhaps there are other errors?

2. The coding of the mathematical formula may be wrong (programming mistake).

3. The pressure integration may react very sensitively to errors in the input data. We found e.g. that setting the second derivatives of the potential in the surface integral to zero produces changes in the results of up to 200%! We know from wave resistance computations that the pressure integrals frequently produce errors of up to 100%.

It will take more collective research to determine the true problem. It is our hope that despite the disappointing results, the formula may prove to be valuable as more research groups follow similar approaches and may then eventually also try to compute the added resistance of ships.

Acknowledgment

We are grateful for the support of our younger colleagues Shuji Mizokami and 'Cowboy' Tanaka in preparation of the results.

References

BERTRAM, V. (1998), *Numerical investigation of steady flow effects in 3-d seakeeping computations*, 22. Symp. Naval Hydrodyn., Washington

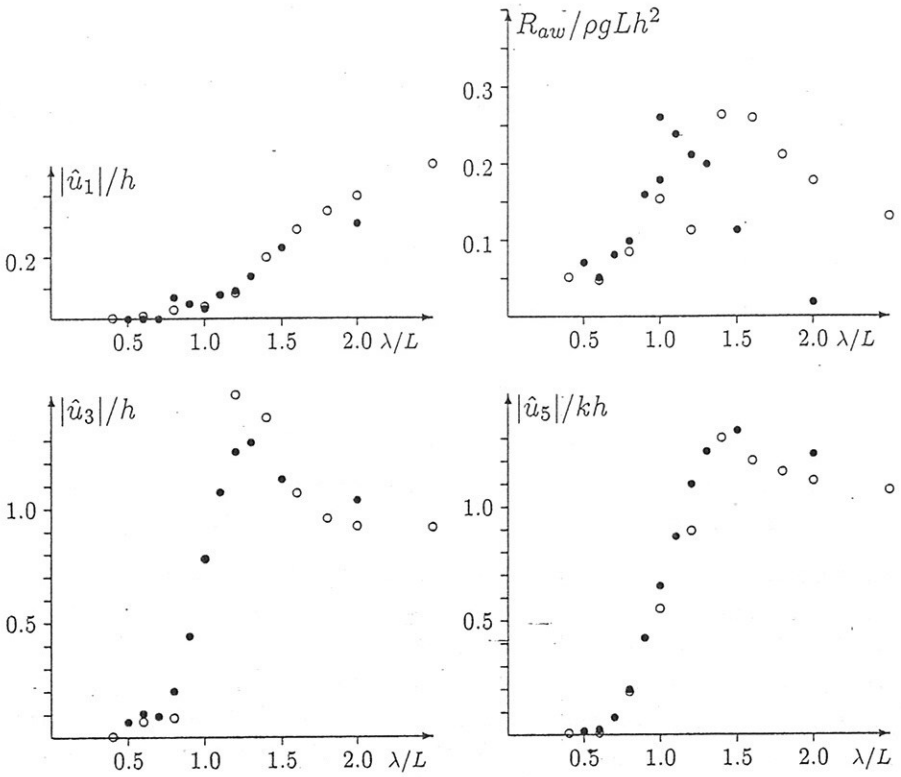

Fig.1: RAOs for S175, $F_n = 0.25$, $\mu = 180°$, • experiment, ○ RSM

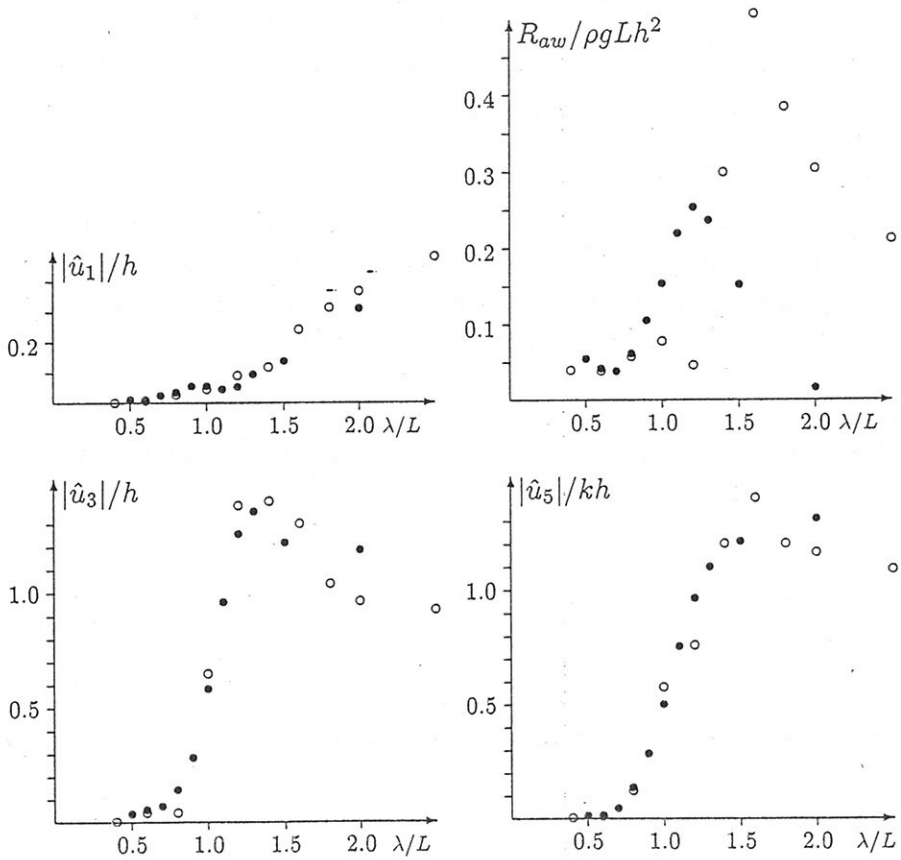

Fig.2: RAOs for S175, $F_n = 0.3$, $\mu = 180°$, • experiment, ○ RSM

NUMERICAL PREDICTION OF WAKE IMPROVEMENT BY VORTEX GENERATOR NEAR STERN USING OVERLAPPING GRID TECHNIQUE

Shiu-Wu CHAU
United Ship Design and Development Center
Keelung, TAIWAN, R.O.C.

ABSTRACT

In order to deal with complex geometry, an overlapping grid technique is developed and incorporated with the USDDC RANS solver. In the overlapping grid technique, the numerical grids of different zones can overlap with each other in the computational domain. More flexibility and ease in generating numerical grids can be obtained. Grid skewness can be better improved, and therefore the numerical diffusion can be also reduced. The demonstrated case shows the numerical prediction of wake improvement of a container ship by installing a pair of vortex generator on ship hull near stern. The numerical results agree well with wind tunnel measurements. The overlapping grid technique is proven to be an effective means to compute flow for complex geometry with required engineering accuracy.

KEYWORDS: Overlapping grid, RANS computation, ship flow calculation

INTRODUCTION

In engineering applications few problems can be modeled only with one-block structured grid for complex geometry. Different kinds of grid techniques have been developed to handle complex geometry [1],[2],[3]. Unstructured grid approach [3] seems to offer good flexibility to deal with such problems. Unstructured domain decomposition [2] is an alternative way to reduce the effort for managing the inter-zone connectivity and, still to maintain the advantage of effective grid distribution. Two groups of grids can be further divided according to the topological relationship of zonal boundaries. In the first group, zonal boundaries are shared and, hence coincided between different zones [1]. Conservation between zonal interface is clearly defined, and can be easily achieved. Overlapping grid [4], which allows grid overlapping between different zones, belongs to the second group. Unlike the grids in the first group, the consistence of flux calculation for overlapping grids at zonal boundary is not implicitly insured. However, different zones can be more economically, easily and flexibly arranged in the computational domain. This will help to improve the skewness problem of numerical grids. In the past years a Reynolds Averaged Navier-Stokes solver [5][6] has been developed using domain decomposition method in United Ship Design and Development Center. In order to meet the increasing need in analyzing flow around ship with complex geometry, the available RANS solver should be upgraded to be able to deal with those challenging geometries. Two most important requirements for engineering applications are the ease of creating an adequate grid within reasonable time and the sufficient accuracy of flow solution. Furthermore, grid skewness should be reduced to avoid causing excessive numerical diffusion. After surveying present numerical methods and the structure of our RANS solver, overlapping grid approach seemed to be the best candidate.

OVERLAPPING GRID APPROACH

Here the overlapping grid approach, mainly following the method proposed in [7], is briefly discussed. Two types of grids are employed in the overlapping grid system: foreground and background grid. Both grids are structured grids. The background grids are applied to cover the whole computational domain without considering local geometry. The foreground grids are designed to take care of the local regions, where complex geometry or high gradient of physical variable exists. Hence, the grid quality and density are more easily controlled. After the foreground and background grids are created in the computational domain, the second step is to remove the some cells of background grid, which reside inside foreground grids, from solution process. The removed cells in background grids are known as hole regions. However, in order to have enough coupling between two overlapping grids, sufficient overlapping region must be given. Besides, the cells of background grids can fall inside the body, which is not physically necessary, and should be also excluded from the numerical calculation. The hole regions define new inner boundaries (hole boundaries) of background grids. The value of field variables on hole boundaries is interpolated from the neighboring cells in foreground grids. The value of field variables on outer boundaries of foreground grids is, in the same way, interpolated from the neighboring cells in background grids. Hence the flow solution is obtained by alternatively solving background and foreground grids.

HOLE GENERATION

A typical overlapping relation between foreground and background grid is shown in Fig.1, where FG denotes foreground ground grid, BG background grid, OR overlapping region, HB hole boundary, HR hole region, and HCB hole creation boundary. The hole region in background grid is defined by the hole creation boundary. The hole creation boundary is often chosen as inner grid surface of foreground grid for simplicity, but there is no other limitation in choosing this boundary, when sufficient overlapping region is insured. A simple two-stage procedure is used to decide the relationship between a given point and a given boundary, Fig.2. The first step is to collect all grid points P_B defining the hole creation boundary and to calculate their outer normal vectors. The second step is to compute P_0 by averaging all P_B. If the position vector R_P between the given point P and P_0 is larger than R_{max}, which denotes the maximum distance between P_B and P_0, P is clearly outside the boundary. If R_P smaller than R_{max}, further test is required. The third step is to find the point P_B, which is closest to P, and the corresponding position vector r_P (using P_B as the base point) between them. The last step is to compute the dot product $r_P \cdot N$. If $r_P \cdot N<0$, the point P is located inside the boundary. Otherwise, it will be outside the boundary. This scheme is quite efficient, but the boundary shape should be always convex to insure the correct hole detection. When boundary is partially concave, it should be divided into several convex boundaries. All points are successively checked through all these sub-boundaries. The cell outside hole region means that its cell center must be outside all these boundaries. Following the above procedure, cells inside the given hole creation boundary can be found. Because the USDDC RANS solver is based on a finite volume formulation, the cell centers, instead of grid vertices, are used to decide whether a cell is inside the hole creation boundary or not.. The hole boundary is then defined as the grid lines shared by cells inside and outside the hole creation boundary.

INTERPOLATION STENCIL

For background grids the boundary conditions for the outer boundary are already specified by the user. The boundary conditions for inner boundary, which are defined by the hole boundary, should be interpolated from the foreground grids.

For foreground grids the outer boundary, in most cases, lies inside the background grids. Numerical interpolation is also required to determine the value of field variables on the outer boundary. The numerical interpolation consists of three basic steps. The first step is to search the interpolation stencils P_i for boundary cell centers stated above. The interpolated point, say point P, should be typically surrounded by eight interpolation stencils P_i, Fig.3. The search of interpolation stencils of P starts from finding its nearest cell center point P_C in the interpolating grid. Then the hexahedrons using P_C as one edge vertex are sequentially checked to identify the hexahedron, which the interpolated point P lies inside. The eight edge vertices of this hexahedron are the interpolation stencils P_i for point P. The second step is to compute the corresponding interpolation coefficient a_i, which is a function of the offset (ξ,η,ζ) in the parametric space. The parametric offset (ξ,η,ζ) is calculated using an iterative procedure based on an isoparametric mapping [7]. At last, the trilinear interpolation is applied to calculate the interpolated value V, where V_i denotes the corresponding field variable of point P_i. The interpolation of boundary values actually builds an indirect coupling between overlapping grids. The degree of coupling depends on the size and location of overlapping, the grid size in overlapping region, and the interpolation scheme etc. According our experiences, some guidance should be followed in order to get good numerical predictions.

RANS SOLVER

The USDDC RANS solver is based on a finite volume discretization. Artificial compressibility model [8] is applied to calculate the steady state solution. Thin-layer approximation [6] is used to simplify the governing equations. A body-fitted coordinate system with matching interface and multi-block structure is employed to model complex ship form. All grid points must be aligned at block interface. The turbulence model proposed by Boldwin-Lomax[9] is incorporated to calculate Reynolds stress tensor. Besides, some modifications for this zero equation model are also implemented. More details of this RANS solver are discussed in [6].

MULTI-BLOCK VERSUS OVERLAPPING GRID

Multi-block grid is widely used to decompose computation domain for complex geometry, Fig.4. For the sake of simplicity, it is always applied together with block-structured topology and grid alignment at block interface. For flow solver only few efforts and simple numerical schemes are required to make the numerical algorithm for one-block capable of dealing with block-structured grids. It seems to be easiest way to create numerical grids for complex geometry. However, the increasing number of blocks often make the grid generation no more straight forward, and the connectivity between different blocks is sometimes very confused. Some grid points are not efficiently distributed in the computation domain due to the matching block interface. Fig.5 give a typical example of overlapping grid system. Less time for creating numerical grids with better grid quality are obtained in practical cases. More accuracy of flow solution could be, hence, obtained due to the more reasonable grid distribution and less skewed grid.

VORTEX GENERATOR

For ships with unfavorable wake distribution at propeller plane, some problems like noise, vibration may occur. If the ship is still in design stage, local modification of stern shape will help to solve this kind of problems. For existing built ships suffering from such problems, an external device is often installed to change stern flow pattern and, hence to get a better wake distribution. Vortex generator is one of the possible devices, and it can can produce a wide range of substantial change in flow field. Here, a 145 m container ship is computed in bare hull condition and with the installation of a pair of vortex generators near stern to investigate the improvement of propeller wake at design speed. Due to the symmetry, only half ship is calculated. Double model is used as the boundary condition for design waterline. Fig.6 is the wake comparison between the measured [10] and the calculated results in bare hull condition. Good agreement is easily observed. However, this ship suffers from a non-uniform wake distribution due to a deep low-speed region near 180°. Fig.7 shows the velocity vectors near hull surface near stern. The red region near ship bottom is the bilge vortex owning flow with high velocity. The green region in the middle is caused by the local hull curvature, and explains why a deep region near 180° with low-speed axial component appears. After the vortex generator is installed, some part of the bilge vortex is redirected to the middle region, Fig.8. A strong vortex with high velocity is then generated This introduces high velocity flow into the propeller plane and improves wake distribution. Fig.9 shows the streamline tracing result from the wind tunnel experiment. The form, location and orientation of vortex generator used in wind tunnel experiment are slightly different from the one used in the numerical computation. Numerical calculation in Fig.10 shows good location agreements of reattachment lines and separation lines. Fig.11 is the wake comparison for vortex generation arrangement. The wake prediction is not qualitatively satisfactory, but quantitatively correct. The prediction has a low-speed region under the hub, which is physically incorrect. But the high velocity components penetrate into the region above hub, where low-speed components early exist, is well reproduced.

CONCLUSION

An overlapping grid method is developed and incorporated with a RANS solver. In the studied case, the prediction of the wake improvement at propeller plane by vortex generator is in good agreement with the measurement. The overlapping grid method is proven to be an effective means to compute flow for complex geometry, e.g. flow around ship with appendage, with required engineering accuracy.

REFERENCES

[1] Chau, S.W., *Numerical Investigation of Free-Stream Rudder Characteristics Using a Multi-Block Finite Volume Method*, Bericht Nr.580, IfS der Uni. Hamburg, 1997.

[2] Lilek, Z., Muzaferija, S., Peric, M., Seidl, V., "An implicit finite-volume method using non-matching blocks of structured grid", *Numerical Heat Transfer*, Part B, Vol.32, pp.385-401, 1997.

[3] Demirdzic, I., Muzaferija S., "Numerical method for coupled fluid flow, heat transfer and stress analysis using unstructured moving meshes with cells of arbitrary topology", *Computational Methods in Applied Mechanical Engineering*, Vol.125, pp.235-255, 1995.

[4] Chau, S.W., Chou, S.K., Chen, C.T., "Composite grid approach for solving N-S equations: Part 1", *Proceeding of 11th Conference On Naval Architecture and Marine Engineering*, pp.373-382, 1998.

[5] Jaw, S.Y., Chou, S.K., "Prediction of an uniform flow past HSVA tanker with two-layer $k\varepsilon$ turbulence model", *Proceeding of CFD Workshop TOKYO 1994*, 1994.

[6] Chou, S.K., Chen, C.T., "Computation of three-dimensional flow around ship hull", *Proceeding of 8th Conference On Naval Architecture and Marine Engineering*, pp.180-184, 1995.

[7] Benek, J.A., Steger J.L, Dougherty, F.C., Buning P.G, *Chimera: A Grid-Embedding Technique*, AEDC Report, AEDC-TR-85-64, 1986.

[8] Chorin, A.J., "A numerical method for solving incompressible viscous flow", *Journal of Computational Physics*, Vol.2, pp.12-26, 1967.

[9] Baldwin, B.S., Lomax, H., "Thin-layer approximation and algebraic model for separated turbulent flows", *AIAA Paper*, No. 78-257, 1978.

[10] *Model Tests for The Project of a 145m Container Feeder*, HSVA Report, N75-96, 1996.

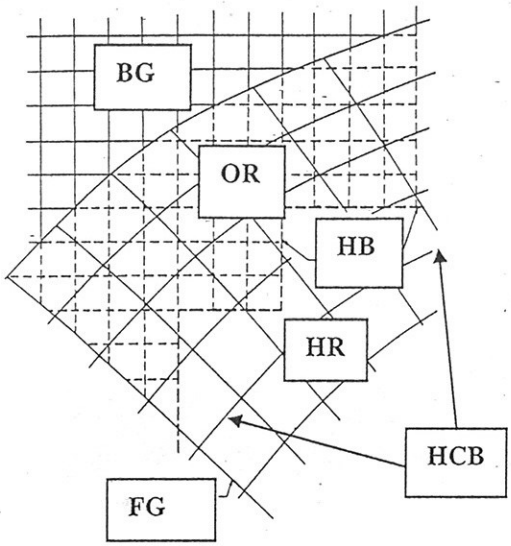

Fig.1: Typical overlapping relationship between foreground and background grid

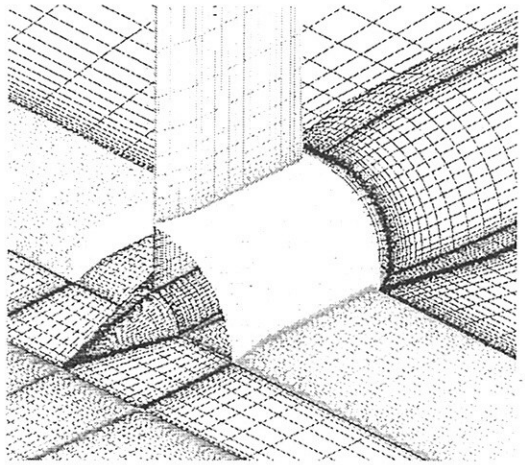

Fig.4: Block-structured grid with matching grid points at block interface

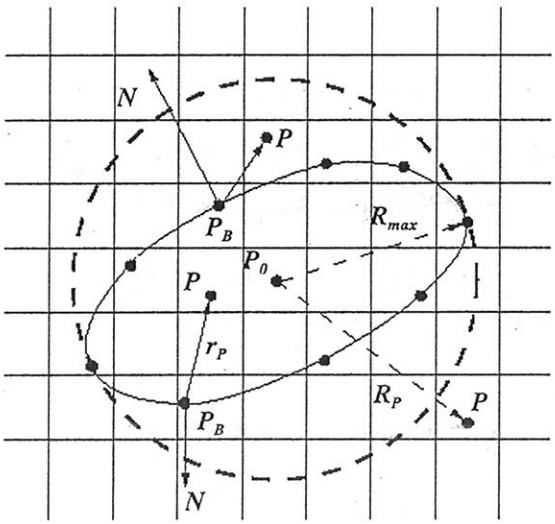

Fig.2: Procedure to decide the relationship between a given point and a given boundary

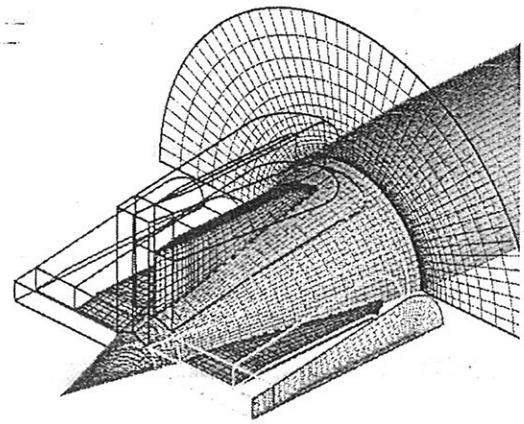

Fig.5: Overlapping grid arrangement for body of revolution with appendage

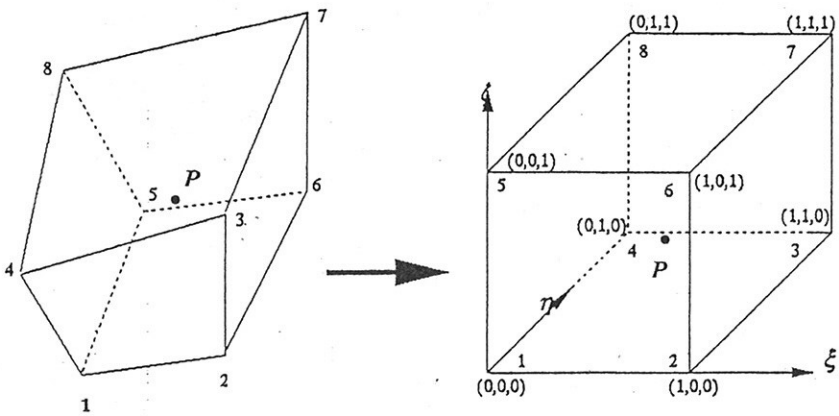

Computational domain

Parametric domain

Fig.3: Isoparametric mapping of interpolation stencils used for trilinear interpolation

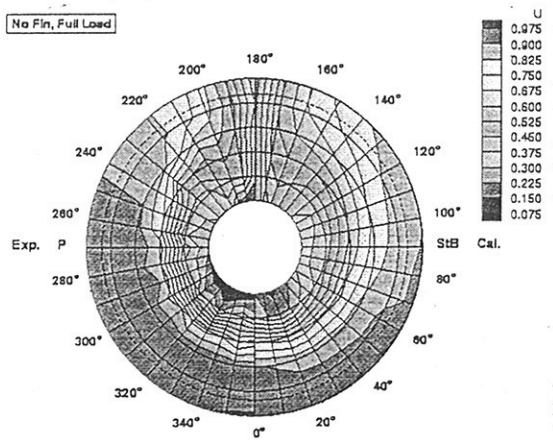

Fig.6: Wake comparison between measured and calculated results at propeller plane in bare hull condition [10]

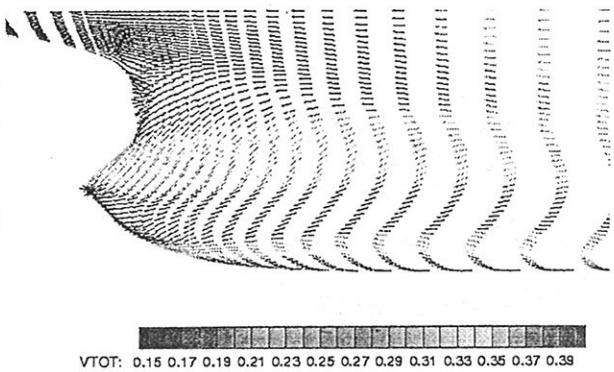

Fig.7: Velocity vector near ship hull in bare hull condition of a 145 m container ship

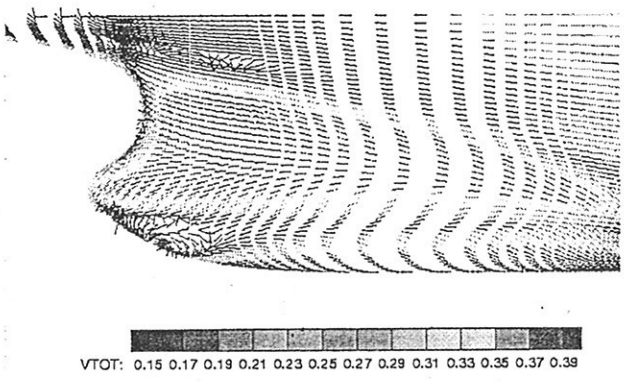

Fig.8: Velocity vector near ship hull with vortex generator of a 145 m container ship

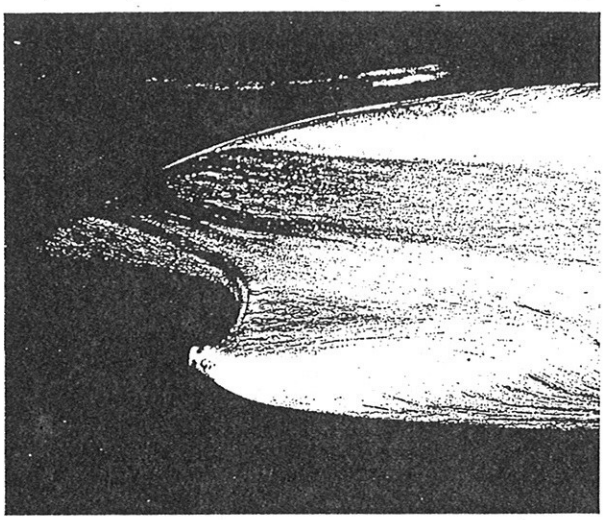

Fig.9: Wind tunnel result of streamline tracing for model with vortex generator arrangement

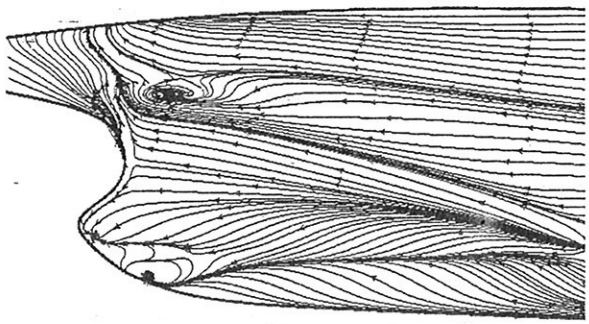

Fig.10: Calculated streamline of a 145 m container ship with vortex generator

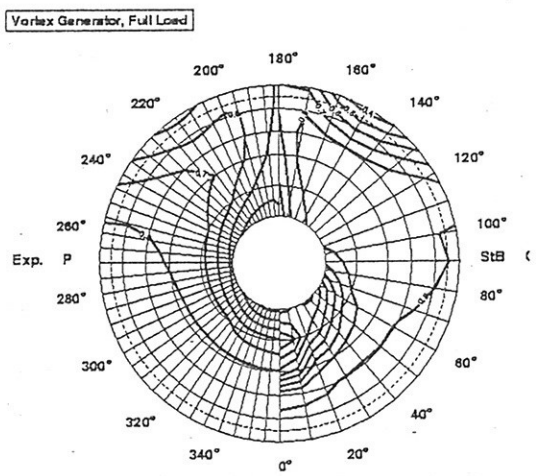

Fig.11: Wake comparison between measured and calculated results at propeller plane with vortex generator arrangement

Validation of Panel Methods for Propeller Flow Analysis

Mario Caponnetto, Rolla SP Propellers, Switzerland

Panel methods are considered a mature tool for propeller analysis and design. This is relatively true if comparing with other fields of marine application of panel methods, such as for predicting wave resistance or sea keeping. One physical reason is the relative smoothness of the flow that is achieved on marine propeller, compared with the complicated flow on the rest of the hull. From the numerical point of view, force computation using pressure integration is less sensitive of errors on the propeller than on the hull. But this accuracy is obtained mainly in open water conditions and around the design point. Results are in general less satisfactory when computing propellers at off design point, and even more unpredictable when including the effect of cavitation. In the present work a systematic comparison between open water measurements and computations is presented at first. The possibility to predict sheet cavitation is then discussed.

Open water computation

The capabilities of numerical tools in predicting propeller performances are very attractive for propeller manufacturers when the kind of application doesn't allow the validation of the design with experimental methods, such as the towing tank or the cavitation tunnels. This is particularly true for small and medium size propellers, due to the obvious time and money constrains. Lifting line and lifting surface methods have been successfully used for a long time. Panel methods should represent an improvement with respect to lifting surface, due to the possibility to properly model the effect of blade thickness, as well as the presence of other thick bodies (hub, duct, and portion of the hull). While the computation of the global forces (and moments) should have an accuracy comparable with lifting surface, panel methods should allow a better determination of the pressure distribution, especially at the leading edge, and this is a valuable improvement for predicting cavitation inception. In its classical Morino formulation [1], panel methods are relatively easy to implement numerically, are fast and stable. The program developed in house at Rolla SP Propeller is a low order panel method, that uses a constant distribution of sources and doublets distributed over non-planar panels (PANAIR); a pressure Kutta condition is enforced at the geometrical trailing edge of the blade; the trailing wake is iteratively aligned to the local flow; viscous drag and viscous pitch reduction are implemented using empirical formula. The method has been extended from the original steady and non-cavitating original version to deal with the unsteady and cavitating cases. Moreover it is used as kernel of the design program currently used at Rolla SP Propellers for submerged propellers design [2].

It has been claimed that panel methods for propeller analysis are mature tools, namely can be applied for practical applications with accuracy comparable with experimental methods. It is true that, for a number of lucky coincidences, the accuracy for propeller analysis is much higher that for other marine applications, such has wave resistance and seakeeping computation. When facing the real life one have to be aware about this statement. A first attempt to validate systematically panel method for open water has been presented by the author in [2]. A total number of 36 B-series propellers, with different blade number (Z=4, 5, 6, 7), expanded area ratios (Ae/Ao=0.6, 0.8, 1.0) and pitch ratio (P/D=0.6, 1.0, 1.4) have been computed with the panel code in the whole range of advance ratios (J), for a total of 324 runs. The computed results have been compared with the experimental data and are presented in figures 1 and 2. While the scattering of the results is quite high, the most obvious trend is that the thrust is in general better predicted then the torque and particularly the torque is highly under-predicted at high loads (low J).

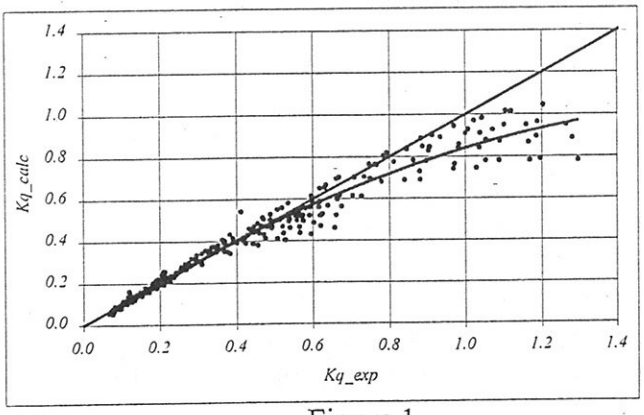

Figure 1

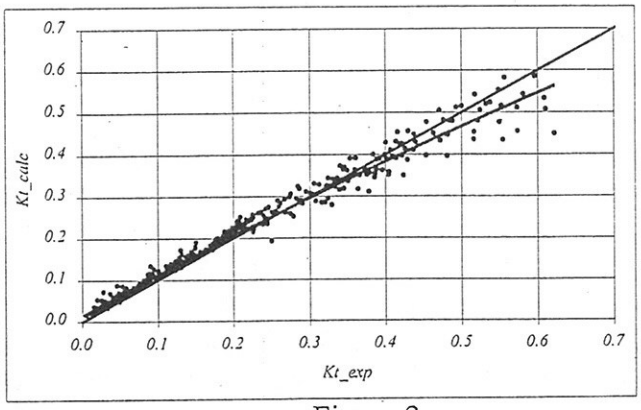

Figure 2

The B-series propellers have been used for this analysis since they represent the most complete and systematic series for propellers. As known, they have very simple blade geometry, with a constant pitch distribution, standard blade outline and skew, and "old-fashion" sections. In particular the profiles are quite different from those normally used nowadays to face cavitation problems, such as the NACA profiles, or even better those customised using for example the Eppler code [3]. It could be expected that for more complex geometries, typical of recent and sophisticated propellers, results should be worst then for the simple B-series; but may be that *simple* geometry doesn't mean necessarily *simple flow*. Indeed several propellers with more complex geometries have been analysed with the panel method, obtaining excellent comparisons with the experiments. As an example, this comparison is presented for propeller AO-177, designed for the US Navy. This 5 bladed propeller has 40 deg of skew, NACA profiles and a variable pitch and camber distribution designed to reduce the circulation near the tip and the hub. In figure 3 open water results for the Kt and Kq are compared with computations obtained with 3 different meshes.

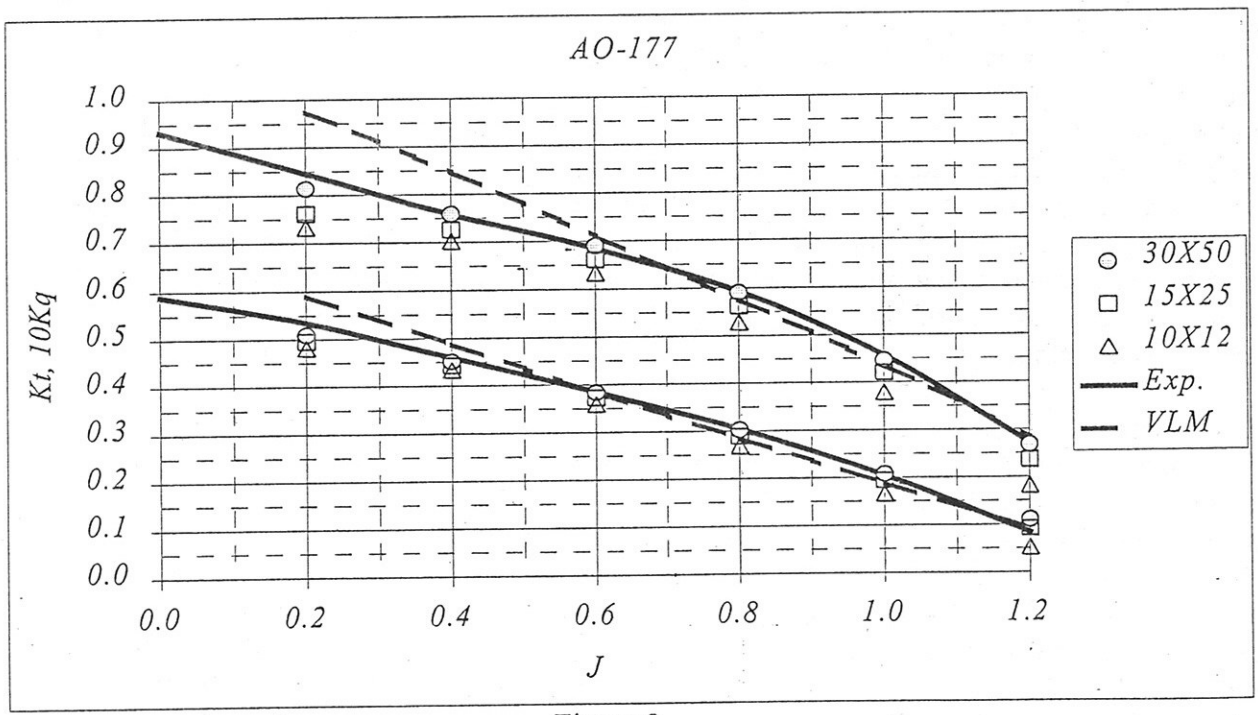

Figure 3

The finest mesh (30X50) consists of 30 spanwise equally spaced panels and 50 chordwise cosinusoidally spaced panels on both sides, for a total of 3000 panels per blade. The agreement with the experiments improves rapidly with the number of panels. The results obtained using a state of the art lifting surface program (VLM) is also shown in the figure. The results obtained with the

panel method are extremely good in the range of advance ratios J=0.4/1.0; thrust and torque is slightly under-predicted only at J=0.2.

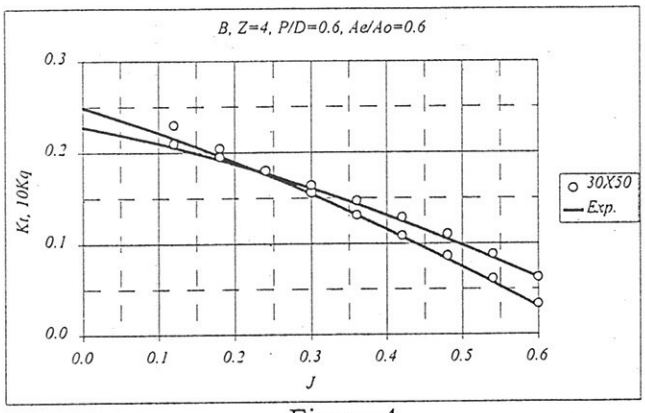

Figure 4

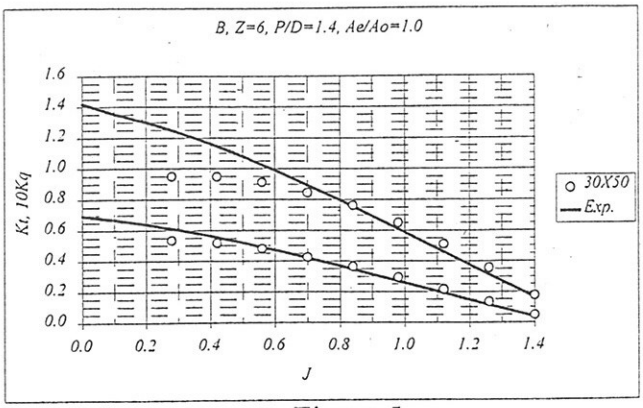

Figure 5

Another good result is presented in figure 4. The propeller is again a B-series, 4 bladed, with Ae/Ao=0.6 and P/D=0.6. At the opposite the propeller of the same family but 6 bladed, with Ae/Ao=1.0 and P/D=1.4 shows disappointing results for the torque below approximately J=0.7. In this case at J=0.28 the torque is under-predicted of about 24% and the thrust of 10%.

One of the possible explanations about the different accuracy of the panel method for different propellers could be explained with the effect of leading edge vortex separation. In the panel method the trailing vortex detachment is imposed at the geometrical cusped trailing edge of the blades. This hypothesis is reasonably satisfied as long as the angle of attack of the flow remains confined in a range of angle of attack above the ideal one. For swept leading edges, above a given angle of attack the flow may separate from the leading edge forming a free shear layer. This shear layer rolls up in a concentrated vortex (leading edge vortex) that flows over the suction side of the blade. The low pressure in the core of the vortex generates an extra lift that cause an increase of the propeller thrust and an even higher increase of torque. In principle, when operating at low J, a propeller with a reduced pitch at the tip, such as the AO-177 or the B-4-60 with P/D=0.6, should experience a lower angle of attack at the tip and consequently less leading edge separation with respect to the propeller with an high pitch (B-6-100 with P/D=1.4). In theory, knowing the position of leading edge separation, the effect of the leading edge vortex could be implemented in the frame of a potential flow method. A tentative approach has been proposed in [4] for a vortex lattice method. While this approach could be explored, it must be pointed out that, from a practical point of view, when the propeller is operating at J lower then the design point cavitation is quite always experienced, further complicating the local flow pattern.

Cavitating propellers

Marine propellers in almost any kind of applications experiences cavitation. For large ship it is important to predict the cavitation pattern and volume variation, in order to predict noise and vibrations. For fast vessels it is mandatory to predict the variation of performances (thrust and torque), experienced by the propeller mainly due the inclination of the shaft. Panel methods can deal with stationary and non-stationary sheet cavitation; an outline of the method can be found in [5] and [6]. While the mathematical formulation of the problem is not particularly difficult, it has been pointed out that the computation of the cavitation pattern is very sensitive of the location of cavity detachment point, not easy to predict. In order to have an idea of the capability of the method for fast propellers, a comparison between computations and experiments performed in the cavitation tunnel is presented. In figure 6 the computed and observed cavity pattern is shown for the propeller operating at a fixed J and varying the cavitation number. The agreement is generally good. In figure

7 and 8 the computed and measured forces can be compared for two different J. The cavitation number of thrust breakdown is quite well predicted in both cases, but below this point a quite large discrepancy of the value of the forces can be observed.

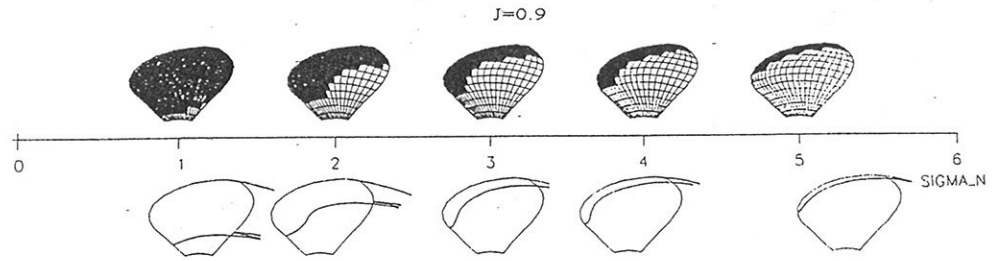

FIGURE 8

Figure 6

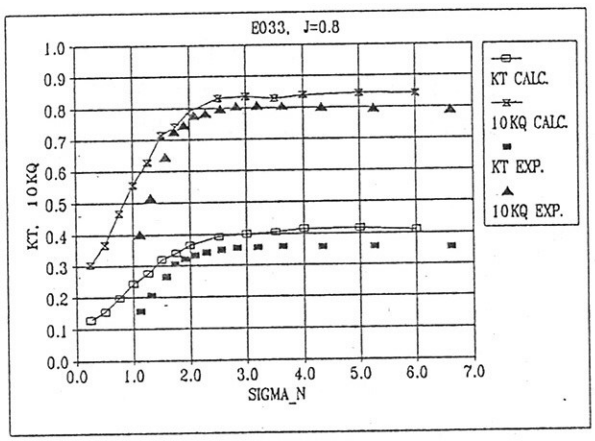

Figure 7

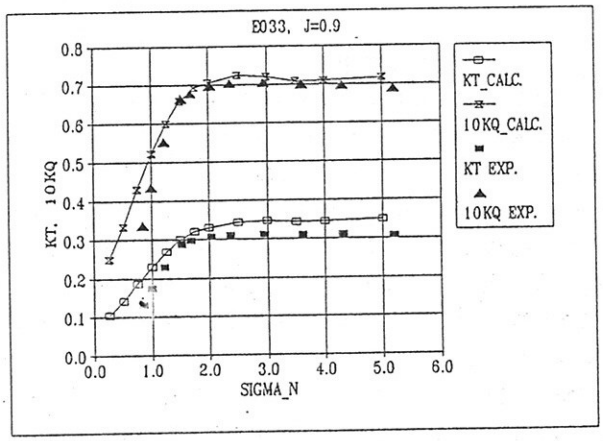

Figure 8

Another major problem experienced by-fast propellers is cavitation and erosion at the junction between the blade and the hub when operating with a large inclination of the shaft. This phenomenon is difficult or impossible to model with a potential flow code, since the local flow is strongly influenced by the viscous flow coming from the brackets and the shaft. Moreover subtle changes in the geometry, such as leading edge or fillet radius, can have a large influence in this phenomenon. A few literature exists on this subject [7]; for this reason the author is trying to increase the knowledge using a Navier-Stokes solver and full-scale observation of the phenomenon.

Conclusion

In this work a validation of panel codes for open water propellers has been attempted. A large number of propellers have been computed and compared with the available experimental data. It can be summarized that the results are in general satisfactory, for engineering purpose, for propellers working close to the design point, while noticeable discrepancies may exists at off design point. Most of this discrepancies could be probably ascribed to the difficulty of predict leading edge separation at large angles of attack. For what concerns cavitating propellers, the panel method used is generally capable to predict the condition of thrust breakdown, very useful for fast propeller design. The author suggests more research in the field of root cavitation for fast propellers.

References

1. Morino, L & Kuo, C.C., "Subsonic Potential Aerodynamics for Complex Configurations: a General Theory", AIAA Journal, vol.12 (no. 2), pp. 191-197, February 1974.

2. Caponnetto, M. & Rolla, P., "Theoretical and Practical Experience in Developing and Tuning Codes for the design and Analysis of Propellers", CFD 99, 5-7 June 1999, Ulsteinvik, Norway.

3. Avellan, F. & Dupont, P., "Analysis of the Cavitation Behavior of Different Propeller Sections", CTI N. 31016.1 Project, EPFL-IMHEF, Study done for Rolla SP Propellers SA.

4. Greeley, D.S. & Kerwin, J.E., "Numerical Methods for Propeller Design and Analysis in Steady Flow", SNAME Transactions, Vol. 90, 1982, pp. 415-453.

5. Fine, N.E. & Kinnas, S., "The Nonlinear Prediction of Unsteady Sheet Cavitation for Propellers of Extreme Geometry", VI Conference on Numerical Ship Hydrodynamics, Iowa City, 1993.

6. Caponnetto, M. & Brizzolara, S., "Theory and Experimental Validation of a Panel Method for the Analysis of Cavitating Propellers in Steady Flow", Propcav 95, Newcastle upon Tyne, 1995.

7. Maioli, G. "Cavitazione delle Eliche nella Zona del Raccordo", Annale N. 5, 1966, Ministero della Difesa, (in italian).

RANS simulations for manoeuvring

G. Delussu, M. Mulas and E. Pillosu

Area of Fluid Dynamics and Combustion, CRS4

CP 94, Uta (Ca), 09010-I

Abstract

In the this work, numerical simulations of flow past a Series 60 hull are presented. Two situations have been analysed: the steady drift flow with 10° angle of attack, and the steady turning. The calculations have been carried out with a novel numerical formulation for numerical towing tank simulations: the fully compressible Euler and Navier-Stokes equations are marched in time with a Jameson-like method, namely an outer multi-grid acceleration algorithm, and an inner multi-stage Runge-Kutta explicit scheme. Beside a preconditioning matrix, to allow for incompressible flow simulations, the present method makes use of an arbitrary equation of state and high order TVD schemes based on Roe's approximate Riemann solver. The arbitrary equation of state used in this work is given in terms of water compressibility coefficients β and χ (respectively at constant pressure and at constant temperature). Despite the use of inviscid approximation on a rather coarse mesh, the preliminary calculations presented show a good convergence capability of the method as well as a good evaluation of sideforces and moments.

The numerical problem

The code **Karalis** solves the fully compressible Euler and Navier-Stokes equations where all couplings between dynamics and thermodynamics are allowed. This is the most general mathematical model for all fluid flows. The code solves the coupled system of continuity, momentum and full energy equation for the velocity components, pressure and temperature. Once u, v, w, p and T are updated, arbitrary thermodynamics is supplied and the iterative numerical procedure can continue. The second order Roe's upwind TVD scheme is used to compute convective fluxes through the Finite-Volume cell interfaces. A V-cycle Coarse Grid Correction Multi-Grid algorithm is used, together with a 5-stage Runge-Kutta explicit time-marching method, to accelerate convergence to a steady state. This formulation, typical of aerodynamic flows, shows an eccellent efficiency even for incompressible flows, once equipped with a preconditioner.

It is in fact well known that, in order to efficiently use a time-marching method to drive incompressible flow solutions to steady state, the acoustic wave speeds need to be considerably reduced, and made comparable to the entropy and shear wave speeds, by means of a suitable preconditioner of the Navier-Stokes system of equations. Merkle's preconditioner [1] has been chosen because it can be easily formulated for arbitrary equations of state given as:

$$\rho, h, \frac{\partial \rho}{\partial p}, \frac{\partial \rho}{\partial T}, \frac{\partial h}{\partial p}, \frac{\partial h}{\partial T} = f(p, T)$$

where p and T represent pressure and temperature. Density ρ and static enthalpy h, as well as their derivatives with respect to both p and T are given by arbitrary functional relations, or even in tabular form.

Inviscid calculations have been carried out for both the steady drift and for the steady turning on a rather coarse and rude O-H type mesh with 113 nodes on the

hull in the streamwise direction, and 41 nodes in the crosswise direction, with some 150,000 nodes total in 5 blocks. The mesh does not resolve the boundary layer, and only inviscid calculations have been performed at this stage of the work.

Results

The table below shows the available references for the S60 steady-drift ($\beta = 10°$) and steady turning cases, with the measured and computed nondimansional sideforces and moments:

reference	[2]	[2]	[3]	[4]	[5]	[6]
Re number	n.s.	n.s.	1.5×10^7	2.67×10^6	2.0×10^6	5.3×10^6
Fr number	0.32	0.10	0.32	0.16	0.0	0.32
motion	SD	SD	SD	SD	SD	ST
mesh	none	none	1,180,000	480,000	400,000	430,000
Sideforce	0.027	0.021	0.026	0.018	0.0184	≈ 0.0
Moment	-0.00184	-0.00103	-0.00187	-0.00100	-0.00119	-0.00030

All of the numerical works (references [3] to [6]) made use of highly stretched grids on the solid walls and turbulence models (RANS simulations). The Reynolds number is not specified in the experimental work [2], and some uncertainty still remains on which the "correct" Reynolds number is. Experiments also show that below $Fr = 0.15$ effects of free surface become negligible. Ref.[3], with $Re = 1.5 \times 10^7$ gives the best agreement of computed sideforce and moment, however using the finest mesh. Ref.[5] is the only computational work at $Fr = 0.0$ and no free surface. Finally, ref.[6] is the only computational work available with the steady-turning case for which there is no experimental evidence. It remains unclear whether the better agreement of ref.[3] is due to a finer mesh, to more accurate numerical methods, or to the higher Reynolds number employed.

The following table summarises the present results (with no free surface $Fr = 0.0$):

fluid	air	air	water	air	water
motion	SD	SD	SD	ST	ST
V_∞	26.2	2.6	1.5	26.2	1.5
Re number	∞	∞	∞	∞	∞
β	9.5	9.5	10.0	0.0	0.0
Sideforce	0.0196	0.0196	0.0203	≈ 0.0	≈ 0.0
Moment	-0.00090	-0.00090	-0.00096	-0.00024	-0.00024

Three cases have been run for the Steady-Drift motion, employing water at $V_\infty = 1.5\ m/s$, and air at $V_\infty = 26.2$ and $V_\infty = 2.6\ m/s$. All 3 cases have the same exact convergence history showing that the preconditioner is doing his job correctly. The computed sideforces and moments are about 10% lower than the experimental results at $Fr = 0.10$. Small differences between air and water can be due to the slightly different angle of attack employed. The Steady Turning case shows identical results for water and air, with a calculated z-moment about 20% lower than that of ref.[6].

In principle, an inviscid external flow simulation represents the limit $Re = \infty$ of a fully turbulent flow simulation, provided that the boundary layer remains attached throughout. If this is the case, the presence of an attached thin boundary layer does not change the overall pressure field, which both the sideforce and the z-moment depend

upon. From ref.[2] there is no evidence of streamwise boundary layer separation. There is however boundary layer separation on crosswise sections. This separation generates x-vorticity and x-moment, but apparently does not affect too much the z-vorticity and the z-moment.

Fig. 1 shows the vertical velocity component w isolines in an horizontal plane below the ship ($z = -0.08$). In the steady-drift case there is a downward fluid motion starting at the front-pressure side of the ship (negative w on the left of the picture), which becomes upward at the rear-suction side. It is a large vortex motion generating x- and y-component of vorticity. Details of the small separations in crosswise sections ($y - z$ planes) are obviously missed by the coarse mesh and by the inviscid (slip) wall boundary conditions. The same plot for the steady-turning case indicates that the main vortex motion has essentially a y-component only of vorticity due to the fact that there is no angle of attack.

Fig.2 shows the pressure isolines at the free surface ($z = 0.0$) together with a few streamlines. The two pictures make sense and wouldn't probably differ too much from those obtained with a fully turbulent simulations with no-slip wall conditions.

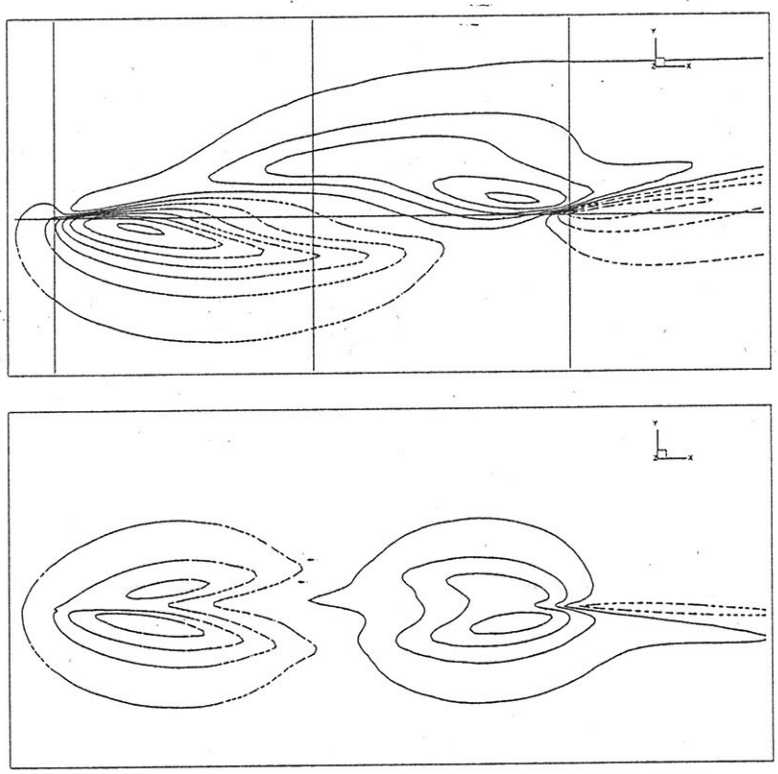

Figure 1: Fig.1: vertical velocity isolines at z=-0.08: steady drift (above), steady turning (below). Dashed isolines for negative values.

Conclusions

An efficient, aerodynamic-like, numerical model has been set up and tested for a typical towing tank simulation. Preliminary results for a S60 ship in both steady drift and steady turning motion have been obtained. Despite the use of a very coarse mesh and the inviscid approximation, calculated sideforces and z-moments are close to those evaluated experimentally and by other numerical simulations. More inviscid and fully

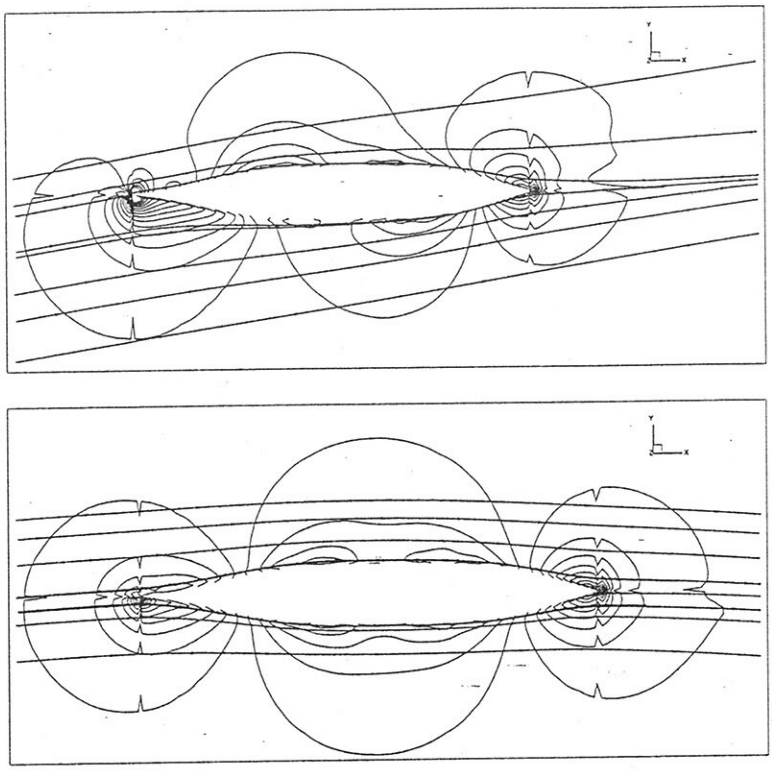

Figure 2: pressure isolines: steady drift (above), steady turning (below)

turbulent simulations on finer and better meshes (a O-O type mesh will be created) will be carried out in the near future in order to understand whether the main forces and moments of interest as well as the vorticity field do need fully turbulent approximation to be correctly resolved.

References

[1] C.L.Merkle *et al.*: *Computation of Flows with Arbitrary Equation od State*, AIAA J. Vol.36 No.4, 1998.

[2] J.F.Longo: *Effects of Yaw on Model-Scale Ship Flows*, Ph.D. Thesis, University of Iowa, 1996.

[3] E.F.Campana, A. Di Mascio and R.Penna: *CFD Analysis of the Flow Past a Ship in Steady Drift Motion*, INSEAN Report.

[4] A.C.Hochbaum: *Computation of the Turbulent Flow Around a Ship Model in Steady Turn and Steady Oblique Motion*, Hamburg Ship Model Basin.

[5] Y.Tahara, J.Longo, F.Stern and Y.Himeno: *Comparison of CFD and EFD for the Series 60 $C_B = 0.6$ in Steady Yaw Motion*, Osaka Prefecture University and University of Iowa.

[6] B.Alessandrini and G.Delhommeau: *Viscous Free Surface Flow Past a Ship in Drift and in Rotating Motion*, Ecole Centrale de Nantes.

TURBULENCE MODELS BENCHMARKED FOR STEADY SHIP YAW FLOW

A. Di Mascio and E.F. Campana
I.N.S.E.A.N., Istituto Nazionale per Studi ed Esperienze di Architettura Navale
Via di Vallerano 139, 00128–Roma, Italia
Fax: +39-06-5070619; E-Mail: a.dimascio@insean.it

INTRODUCTION

Numerical solution for the steady flow past a ship in straight course with a yaw angle have been obtained with a finite volume RANSE solver. Two different turbulent models, namely the Baldwin - Lomax and the Spalart - Allmaras models, have been applied and the results have been validated against experimental measurements, collected by Longo [1] for boundary layer, wake and wave fields of a Series 60 hull in yaw motion.

The new one-equation model by Spalart and Allmaras [2] is encountering an increasing popularity in the aeronautical community, whereas there is little experience on the use of this model in the naval hydrodynamic context. As a results of this benchmark, solutions obtained with the Balwin-Lomax model agree well for global coefficients and wave profiles, but the contours of the axial velocity in some cross-planes reveal that most details of the measured data are not caught. Results for the axial velocity contours with the Spalart-Allmaras model are in better agreement with experimental data.

DESCRIPTION OF THE NUMERICAL AND TURBULENCE MODELS

The solution of the free-surface viscous steady flow past a ship hull has been obtained as the asymptotic solution of the unsteady pseudo-compressible Navier-Stokes equations, [3]. A general description of the numerical code used to run the turbulent model as well as the boundary conditions can be found in [4].

The mathematical equations are approximated by a discrete finite volume model. The fluid domain D is divided into structured blocks, each with $N_i \cdot N_j \cdot N_k$ disjoint hexahedrons D_{ijk}. Velocity and pressure at the interface, needed for the computation of the Eulerian fluxes, are evaluated by a second-order E.N.O.-type scheme [5] while a Runge-Kutta type scheme updates the numerical solution from step n to step $n+1$.

A special multigrid algorythm for ENO schemes [6] was used to enhance the convergence rate.

In the simulations two different turbulent models have been employed: the Baldwin-Lomax algebraic turbulent model [7] and the Spalart-Allmaras one equation model [2]. Both these models are based on the eddy viscosity concept, i.e. on the assumption that the Reynolds stress tensor $(-\overline{\rho u_i' u_j'})$ is related to the mean strain rate through the eddy viscosity ν_T

$$-\overline{u_i' u_j'} = \nu_T \left(\frac{\partial \bar{u}_i}{\partial x_j} + \frac{\partial \bar{u}_j}{\partial x_i} \right) - \frac{2}{3}\delta_{ij} k \qquad (1)$$

where k is the turbulent kinetic energy.

A brief description of the Spalart and Allmaras model. is given in the following. For the Baldwin and Lomax models the reader is referred to [7].

In what follows, it can be noted that the Spalart-Allmaras model is strictly "local", in the sense that the coefficients in the equations depends only on quantities that can be computed from the velocity field and its first order tensor in each point, and from the distance from the nearest wall. This property renders this model very attractive when dealing with complex geometries and therefore with multiblock meshes or unstructured grids. On the contrary, the Baldwin-Lomax model requires the evaluation of the wall shear stress at the intersection of the "normal" to the wall; consequently, ambiguities often arises when simulating the flow past boundaries like, for instance, hull with appendages.

In the Spalart and Allmaras model, the eddy viscosity ν_T is computed by means of an intermediate variable $\tilde{\nu}$

$$\nu_T = \tilde{\nu} f_{v1}(\chi), \qquad \chi = \frac{\tilde{\nu}}{\nu}, \qquad f_{v1}(\chi) = \frac{\chi^3}{\chi^3 + C_{v1}^3} \qquad (2)$$

$\tilde{\nu}$ is computed from the solution of a partial differential equation

$$\begin{aligned} \frac{D\tilde{\nu}}{Dt} &= c_{b1}\left[1 - f_{t2}\right]\tilde{S}\tilde{\nu} \\ &- \left[c_{w1} f_w - \frac{c_{b1}}{k^2} f_{t2}\right]\left[\frac{\tilde{\nu}}{d}\right]^2 \\ &+ f_{t1}\Delta U \\ &+ \frac{1}{\sigma}\left[\nabla\cdot((\nu+\tilde{\nu})\nabla\tilde{\nu}) + c_{b2}(\nabla\tilde{\nu})^2\right], \end{aligned} \qquad (3)$$

where $\tilde{S} = S + [\tilde{\nu}/(k^2 d^2)] f_{v2}$, S is the magnitude of the vorticity vector, d the distance from the wall, $f_{t1}, f_{t2}, f_w, f_{v2}$ are functions that depends only on χ and the distance from the wall; finally, the c-s and k are constants. The first two terms in the right hand side represent production and destruction of $\tilde{\nu}$,respectively; the third one is the so-called "trip" term, that allows to specify the laminar-turbulent transition point (in the results shown in the next section,

this term was always turned off); the last part is a dissipation term, that contains also a non conservative portion $c_{b2}(\nabla\tilde{\nu})^2$ which is responsible, together with the non-linear part of the diffusion term $\nabla\cdot(\tilde{\nu}\nabla\tilde{\nu})$, for the advection of a turbulent front into non-turbulent regions.

RESULTS

As a benchmark test for the comparison between the two turbulence models, the flow past a Series 60 hull with $C_b = 0.6$, moving in steady motion, was computed for yaw angles $\alpha = 0°, 2.5°, 5°, 10°$ at $Fr = 0.316$, $Re = 5.3 \cdot 10^6$. Detailed experimental data were collected by Longo *et al.* in [1] for the same configuration. In both the simulation and the experiments, 'port' is the pressure side, 'starboard' the suction side.

The two turbulence models have been tested by implementing the models on the same numerical code.

The fluid domain was divided into port and starboard blocks with O-O topology, each block with $96 \times 96 \times 64$ cells in stream-wise, normal, and girthwise direction, respectively. Five coarser were generated by halving the number of cells in each direction in the previous finer grid. Although the coarsest grid is only $6 \times 6 \times 4$. and this mesh is too poor to get an accurate numerical solution, it is convenient to have such a coarse grid to speed up convergence with the full multigrid approach.

As expected, the use of different turbulent models has no appreciable influence on the wave pattern and on the wave profile. Hence, the comparison between the two turbulence models is carried out by comparing the local velocity fields in four transversal sections. The analysis has been focused on the starboard region, where viscous and wave effects are stronger.

In figs. (1), (2), the results obtained with the Baldwin-Lomax model have been compared with the experimental data, while in figs. (3), (4) results computed by using the Spalart-Allmaras model are shown. Contours of the axial velocity u are shown at $x = 0.9,\ 1.0$ for $Fr = 0.316$, $Re = 5.3 \cdot 10^6$, and $\alpha = 10°$.

With the Baldwin-Lomax model, although the global trends are predicted, the strong bilge vortex in the suction side in the numerical simulation is much weaker than in the experiment. The Reynolds stresses in the simulation seem to be too strong with respect to the actual situation, and therefore the shed vorticity too weak. This is illustrated in fig. (5),fig. (7), by comparing numerical and experimental streamlines for $x = 1.0$. In the experiments the vortex is approximatively located at $y = 0.02, z = -0.03$. The simulation predicts a less intense vortex, located at the same depth, but at $y = 0.01$. With the Spalart-Allmaras model, global trends are much better predicted. In all the computed transversal sections the agreement between numerical and experimental data is better than that obtained with the Baldwin-Lomax model. Furthermore, the strong bilge vortex in the suction side is much more like the one visualized in the experiment. This is illustrated in fig. (6),fig. (7), by comparing numerical and experimental streamlines for $x = 1.0$. The Spalart-Allmaras model predicts an intense vortex, located at a depth of $y = 0.015, z = -0.2$, close to the location of the measured vortex.

As a general comment, the departure of the numerical prediction obtained with the Baldwin-Lomax model from the experimental observation should be attributed to its simplified nature, which does not take into account any diffusion or convection effects of the turbulent viscosity. In fact, the Baldwin-Lomax model is purely algebraic, and therefore connected only to the local properties of the flow.

CONCLUSIONS

Two different turbulent models, namely the Baldwin-Lomax and the Spalart-Allmaras models, have been used and the results have been validated against experimental measurements for boundary layer, wake and wave fields of a Series 60 hull in yaw motion.

Numerical results compare favourably with experimental data with regards to the hydrodynamic coefficients. The main features of the flow phenomena are reproduced by the simulation and the behavior of the two turbulence models is pointed out in the analysis of the axial velocity contours and the transversal streamlines in the the propeller region.

The Spalart-Allmaras turbulent model appears to be a promising trade-off between CPU cost and reliability of the results. Results obtained with the Balwin-Lomax model agree well for global coefficients and wave profiles, but the contours of the axial velocity in some cross-planes reveal that most details of the measured data are not caught. Results for the axial velocity contours with the Spalart-Allmaras model are in better agreement with experimental data.

ACKNOWLEDGEMENTS

This work was supported by the Italian Ministry of Transportation in the frame of INSEAN research plan 1997–99.

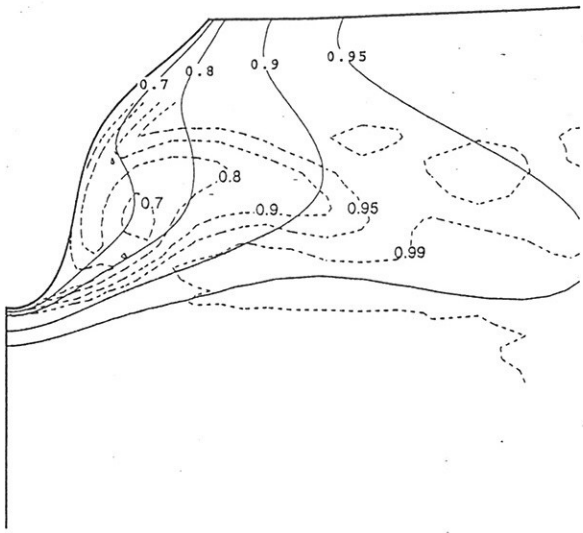

Figure 1: Numerical (Baldwin-Lomax, solid) and experimental (dashed) contours of the axial velocity u. Left $x = 0.9$, right $x = 0.9$. $Fr = 0.316$, $Re = 5.3 \cdot 10^6$, $\alpha = 10°$

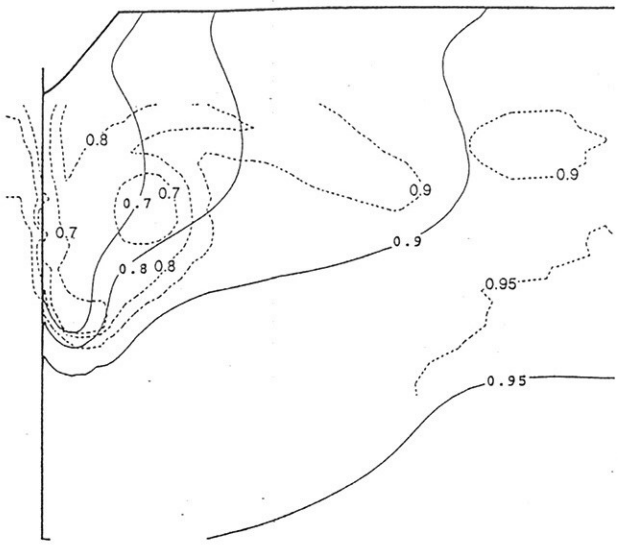

Figure 2: Numerical (Baldwin-Lomax, solid) and experimental (dashed) contours of the axial velocity u. Left $x = 1.0$, right $x = 1.0$. $Fr = 0.316$, $Re = 5.3 \cdot 10^6$, $\alpha = 10°$

REFERENCES

1. Longo, J.F., Effects of Yaw on model-scale Ship Flows, Iowa Institute Hydraulic Research, Iowa City, 1996.

2. Spalart, P.R. and Almaras, S.R., "A one-equation turbulence model for aerodynamic flows," La Recherche-Aérospatiale, No. 1, 1994, pp. 5–21.

3. Chorin, A.J., "On the convergence of discrete approximations to the navier–stokes equations," Math. Comput., No. 23, 1969, pp. 341–353.

4. Di Mascio, A. and E.F.Campana, "Yaw flow simulation for the series 60," Ship Technology Research, to be published.

5. A. Harten, B. Engquist, S. Osher and Chakravarthy, S.R., "Uniformly high order accurate essentially non–oscillatory schemes," J. Comp. Phys., Vol. 71, No. 231, 1987.

6. B. Favini, R. Broglia and Di Mascio, A., "Multigrid acceleration of second order eno schemes from low subsonic to high supersonic flows," Int. J. Num. Meth. Fluids, No. 23, 1996.

7. Baldwin, B.S and Lomax, H., "Thin layer approximation and algebraic model for separated turbulent flows," AIAA Paper, Vol. 78, No. 257, 1978.

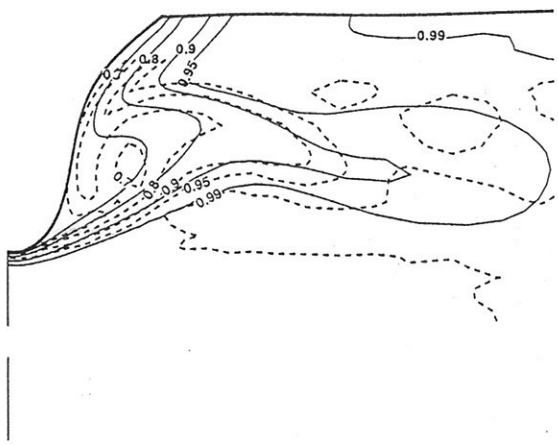

Figure 3: Numerical (Spalart-Allmaras, solid) and experimental (dashed) contours of the axial velocity u. Left $x = 0.9$, right $x = 0.9$. $Fr = 0.316$, $Re = 5.3 \cdot 10^6$, $\alpha = 10°$

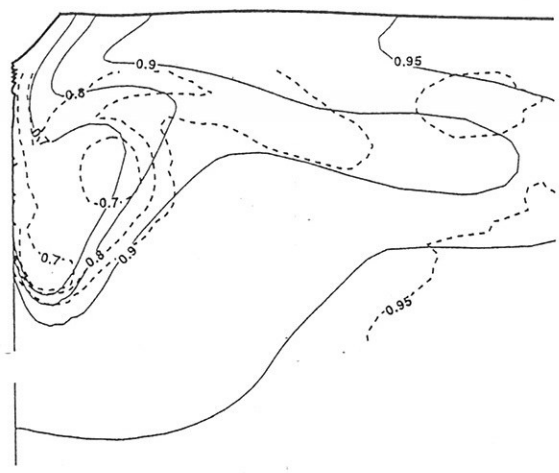

Figure 4: Numerical (Spalart-Allmaras, solid) and experimental (dashed) contours of the axial velocity u. Left $x = 1.0$, right $x = 1.0$. $Fr = 0.316$, $Re = 5.3 \cdot 10^6$, $\alpha = 10°$

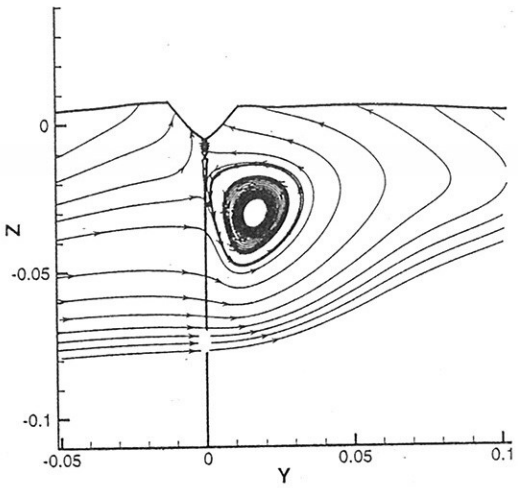

Figure 6: Cross-flow streamlines of the flow onto the (y, z) plane at $x = 1.0$. Numerical (Spalart-Allmaras) solution.

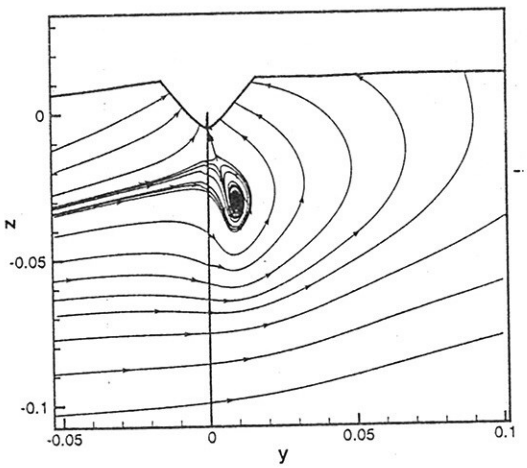

Figure 5: Cross-flow streamlines of the flow onto the (y, z) plane at $x = 1.0$. Numerical (Baldwin-Lomax) solution.

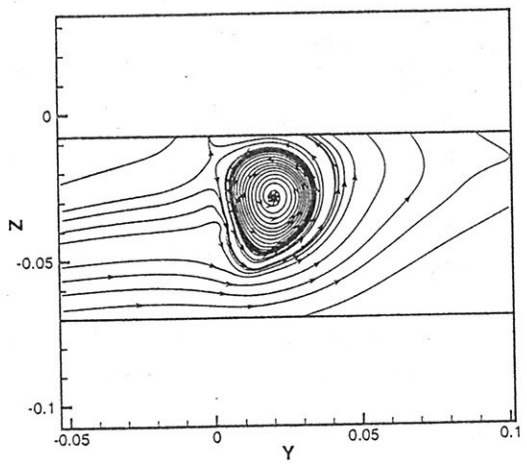

Figure 7: Cross-flow streamlines of the flow onto the (y, z) plane at $x = 1.0$. Experimental data.

Numerical investigation of propeller-rudder interaction

Ould El Moctar, Technical University Hamburg-Harburg[1]

Rudder forces and moments should be determined including the interaction with ship hull and propeller, especially if the rudder is located just behind a propeller. My previous research activities were limited to rudders in uniform flow [4]. Here I shall present Rans calculations for three kinds of flows: Modern controllable-pitch propellers in uniform flow; Rudders in uniform flow; and Rudders behind a propeller.

1 Propeller in uniform flow

The turbulent flow around free-running propellers was computed using a commercial Ranse code [6] using the finite-volume method and the k-ϵ turbulence model with wall functions. Grids were produced using the commercial code ICEM-HEXA. The grid on and around the propeller blade is of O type (Fig 2), whereas in flow direction it is of H type. The reference system rotated with the propeller to obtain a stationary flow. Two block-structured grids of 450,000 and 650,000 cells were used. A modern controllable-pitch propeller of the Potsdam towing tank SVA (Fig 1) was chosen because experimental results were available for it. For the fine grid differences between the experimental and computed thrust were $< 3\%$ (Fig. 3); also the computed and experimental thrust coincided very well for most of the range of advance ratios. For large advance ratios leading to small K_Q values outside of the design range differences up to 7% were found. Reasons for the larger differences may be the substantially oblique inflow direction and the small torque to which the percentage errors refer.

2 Effects of a fixed fin on rudder force and influence of gap width

In my earlier works [4] the effects of profile shape, profile thickness and aspect ratio of spade rudders were investigated. Here a single-blade rudder in free flow is compared with a system consisting of a fixed fin and a rudder beneath. Such arrangements are used to reduce the shaft bending moment in spade rudders. The total area and shape of the fin + rudder system was the same as that of the single-blade rudder. It was found that the fin + rudder system produces hardly less lift than the single-blade rudder, because also the fixed fin generates lift due to the oblique flow generated by the rudder. For smaller rudder angles, the resistance of the rudder plus fin is up to 20% less than that of the single-blade rudder, because the fin generates nearly alone frictional resistance and no induced resistance (Fig 4). However, for larger rudder angles a pronounced tip vortex occurs between fin and rudder, increasing the induced resistance.

The gap width between rudder and fin was varied between 0 and 10cm. Below 7cm gap width the effects were $< 3\%$, but for larger gap width the effects increased considerably (Fig 5).

3 Rudder behind propeller

3 methods were applied to investigate the influence of the propeller on rudder forces:

1. The instationary viscous flow around a system consisting of the above-mentioned propeller and the rudder was computed using a grid of 750,000 cells surrounding both bodies. R_n was $32 \cdot 10^6$.
2. For the same physical arrangement, the propeller was modelled by external forces only. The grid had 300,000 cells. The Computation has been steadly performed.
3. The stationary potential flow around a rudder-propeller configuration was computed using a panel method [7] . The influence of the propeller slipstream was modelled by seting velocities at the inlet according to the guideline giving in [7].

[1]Lämmersieth 90, D 22305 Hamburg, Germany

Fig.6 shows that the deviations between the results of all 3 methods are small. Results of method 1 show also that the distance between rudder and propeller has minor effects only.

4 Summary

The computed results for force and moment agree well with measurments and, thus appear accurate enough for various practical applications.
The future research will concentrate on including the ship hull.

5 References

[1] Abdel-Maksoud, M., Menter F.R.,Wuttke, H.: Viscous Flow Simulations for Conventional and High Skew marine Propellers, Ship Technology Research, Vol. 45, No. 2, 1998
[2] Brix, J. (1993), Manoeuvring Technical Manual, Seehafen Verlag
[3] Chen, B. (1993), Computational Fluid Dynamics for Four-Quadrant Marine Propeller, Proceeding of FED'98, FED SM 98-4872, ASME 1998
[4] El Moctar, O. (1997), Numerical determination of rudder forces, Euromech 374, 1998
[5] Ferziger, J.H., Perić, M. (1996), Computational Methods for Fluid Dynamics, Berlin: Springer- Verlag
[6] ICCM Institute of Computational Continuum Mechanics GmbH, User Manual, Comet Version 1.040, Hamburg 1999.
[7] Söding, H. (1998), Limits of potential Theory in Rudder Flow Predictions, Ship Techn. Res. 45

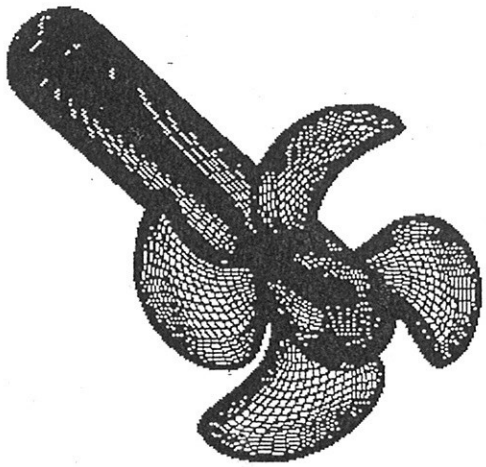

Figure 1: SVA-Propeller

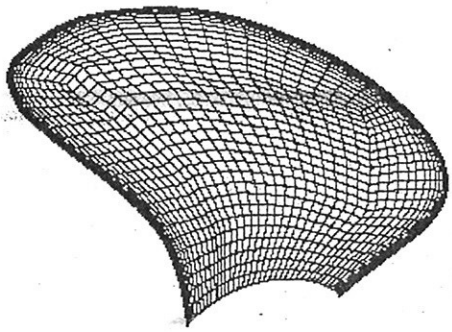

Figure 2: O Grid Philosophy

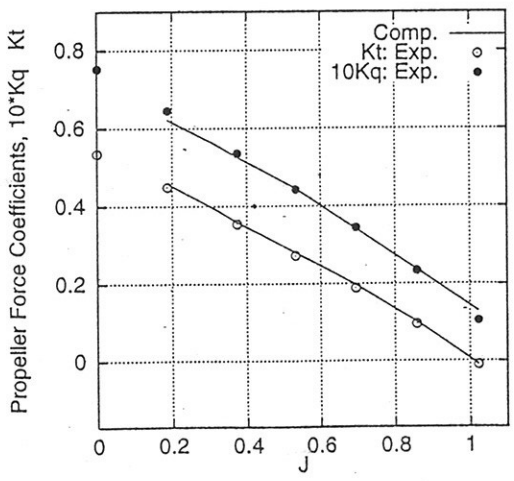

Figure 3: Measured and Predicted K_T and K_Q for the SVA-Propeller

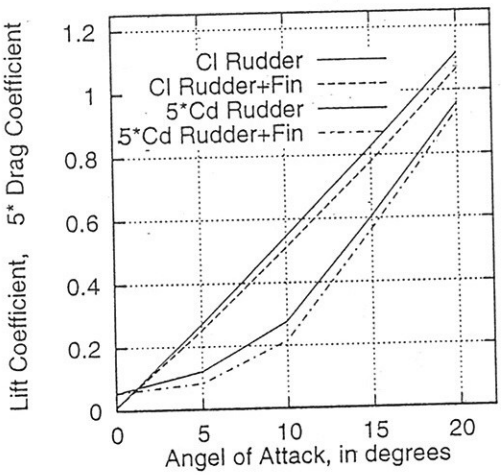

Figure 5: Effects of a Fixed Fin

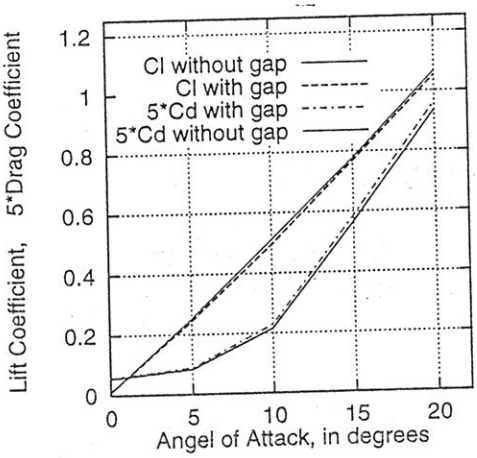

Figure 4: Gap Effects

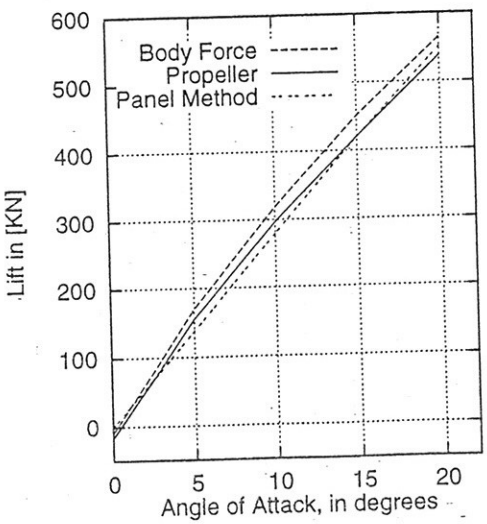

Figure 6: Ruder Forces in a Propeller Slipstream

Simulation of Free Surface Ship Flows with a VOF-Euler Code

Dieke Hafermann
Hamburg Ship Model Basin (HSVA)
Bramfelder Str.164, D 22305 Hamburg
hafermann@hsva.de

1 Introduction

Free surface flows play an important role in the design of a ship. Today potential theory methods are widely used to analyse such flows. A drawback of the potential theory is the inaccurately predicted drag. During the past years, methods for solving the Navier-Stokes-Equations have been developed which describe the free surface by adapting the mesh boundaries. These methods, however, do only apply to smooth free surfaces. Here the development and application of a Finite-Volume-Code using the Volume of Fluid (VOF) method for the simulation of inviscid unsteady free surface flows will be described. With this method, the position of the free surface is described by the void fraction in the computational domain.

Several applications will be shown. First results show an significant improvement in the resolution of the wave field compared to potential theory results.

2 Mathematical Model

The transient flow of an inviscid and incompressible fluid is considered. It is described by the conservation equations for mass and momentum, formulated in an inert Cartesian coordinate system, the momentum equations are written as

$$\underbrace{\frac{\partial}{\partial t}\int_{\Omega}\rho\vec{v}d\Omega}_{\text{non stationary term}} + \underbrace{\int_{S}\rho\vec{v}((\vec{v}-\vec{v_b})\vec{n})dS}_{\text{convective term}} = -\underbrace{\int_{S}\hat{p}\vec{n}dS}_{\text{pressure force}} + \underbrace{\int_{\Omega}\rho\vec{g}d\Omega}_{\text{gravity force}} \tag{1}$$

where, $\vec{v} = (u, v, w)^T$ denotes the velocity vector with its components in x, y and z direction, $\hat{p}$ the pressure, ρ the density and $\vec{g}$ the gravity vector. Further variables are the control volume Ω ,the velocity of the control volume $\vec{v_b} = (u_b, v_b, w_b)^T$, the control volume Ω , the surface area S and the normal vector of the control volume surface $\vec{n}$. The pressure $\hat{p}$ is the sum of the dynamic and the hydrostatic pressure

$$\hat{p} = p + i\rho\vec{g}\vec{r}. \tag{2}$$

The vector $\vec{r}$ denotes the position of the free surface, the gravity vector $\vec{g}$ is normal to the undisturbed free surface. For a completely filled control volume the conservation equation for mass is

$$\frac{\partial}{\partial t}\int_{\Omega}\rho d\Omega + \int_{S}\rho(\vec{v}-\vec{v_b})\vec{n}dS = 0\,. \tag{3}$$

To describe the free surface, a function $\hat{f}$ is introduced with a value of either 1 denoting liquid or a value of 0 denoting gas. The function $\hat{f}$ is a non steady function. The free surface is the boundary line where $\hat{f}$ changes from 0 to 1. Fluid particles above the free surface will always have a value $\hat{f}$ of 0 and particles below a value of 1. This yields a conservation equation for $\hat{f}$ which is independent of the position of the control volume

$$\frac{\partial}{\partial t}\int_{\Omega}\rho\hat{f}d\Omega + \int_{S}\rho\hat{f}(\vec{v}-\vec{v_b})\vec{n}\,dS = 0\,. \tag{4}$$

Below the free surface this leads to a mass conservation equation (3). The cell fill ratio F is the ratio of the cell volume filled by the liquid to the total cell volume

$$F = \frac{\int_{\Omega} \hat{f} d\Omega}{\int_{\Omega} d\Omega} . \tag{5}$$

By definition this ratio has values between 0 (empty) and 1 (full). At the free surface ambient pressure is assumed: $\hat{p} = \hat{p}_a = \text{const}$ (dynamic boundary condition). This leads to

$$p = \hat{p}_a - \rho \, \vec{g} \, \vec{r} \qquad \text{at the free surface .} \tag{6}$$

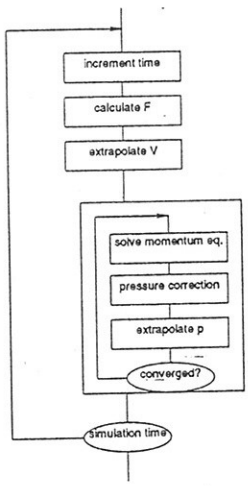

Figure 1: The flowchart of the algorithm

Figure 1 shows the algorithmic scheme. At the beginning of every physical timestep, the VOF-function F is calculated. The surface integral needed for the FV formulation is approximated using the product of the flux and the open cell surface ratio. The open cell surface o is defined as follows

$$\int_S \hat{f}(\vec{v} - \vec{v_b})\vec{n} \, dS \approx f \frac{\int_{Se} \hat{f} dS}{\int_{Se} dS} = feoe . \tag{7}$$

Since the cell fill ratio F is an unsteady function, the cell surface ratio cannot be obtained by interpolation but has to be calculated iteratively. This leads to a description of the free surface. The velocities close to the free surface are extrapolated using the neighbouring values.

Afterwards the SIMPLE Algorithm is applied to solve for the velocities and the pressure. Starting with an approximated solution for the pressure, the linearised momentum equations are solved. To satisfy the continuity equation the pressure and the velocities are corrected by applying the so-called pressure correction. The two steps are repeated until the required accuracy is reached.

In addition to the dynamic boundary condition at the free surface, several other boundary conditions must be applied:

- At the inlet, the velocity is fixed and the pressure is extrapolated,
- at the outlet, the pressure is fixed and the velocity is extrapolated,
- at the symmetry planes, fluxes are set to zero and the pressure is mirrored,
- at the wall, the fluxes are set to zero and the pressure is extrapolated.

The waves are damped in z-direction by applying an artificial force, which depends on the velocity component w and the distance from the ship.

3 Discussion

Figure 2 shows a part of the coarsened grid for the 'Hamburg Test Case', a container ship with a Froude number of 0.238. At the beginning and the end of the ship as well as close to the free surface the resolution is refined. The computational results are shown in figure 3. Compared are the results for the wave distribution obtained by potential theory (bottom) and a VOF-Euler calculation (above). The Euler calculation used about 330000 cells. It can be seen that the VOF-method yields a more detailed description of the free surface, in particular at the stern. The results are in good agreement with measurements.

In figure 4 the details at the stern of a fast mono hull are shown. The separation at the lower edge and the development of the waves at the sides can be seen.

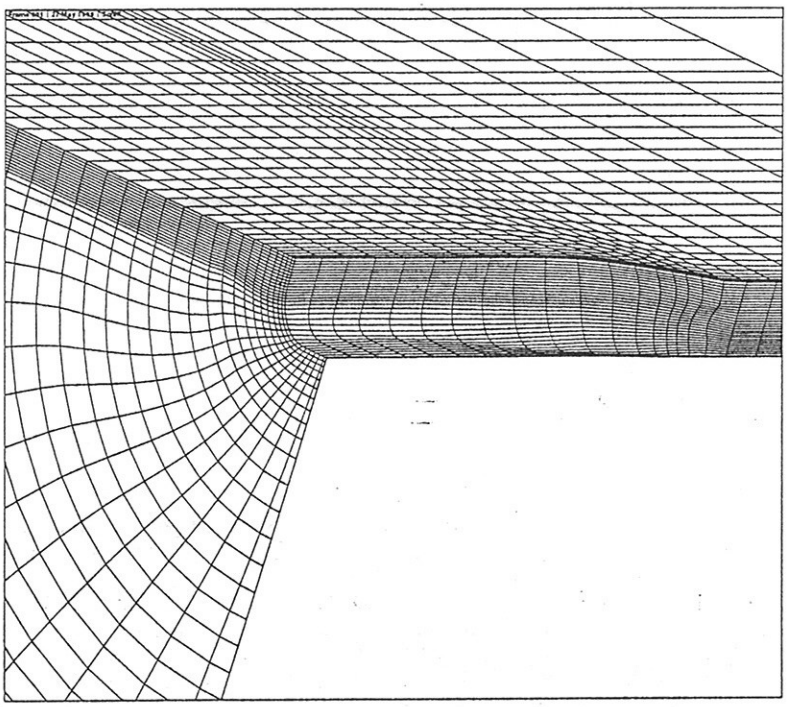

Figure 2: Example of a mesh for the Hamburg Test case

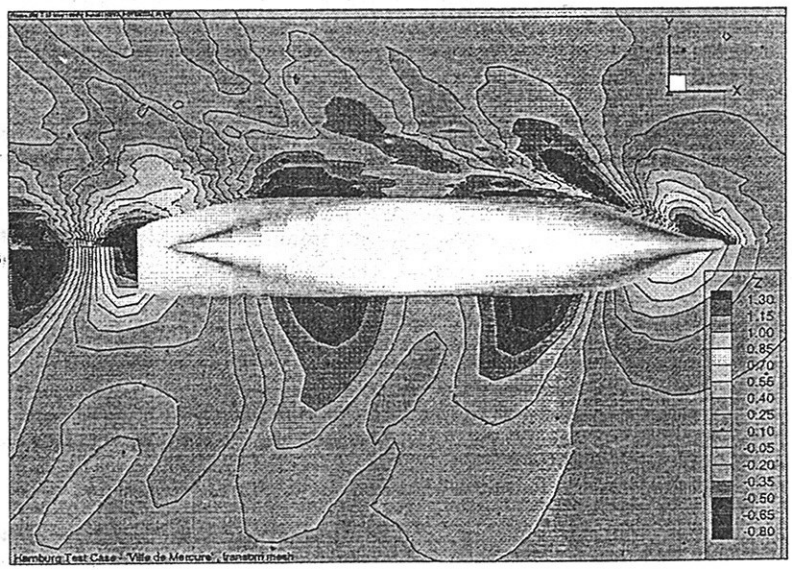

Figure 3: Wave contour for the Hamburg Test case

Figure 5 shows experimental data together with the results of a numerical simulation for a series 60 ship. The Froude

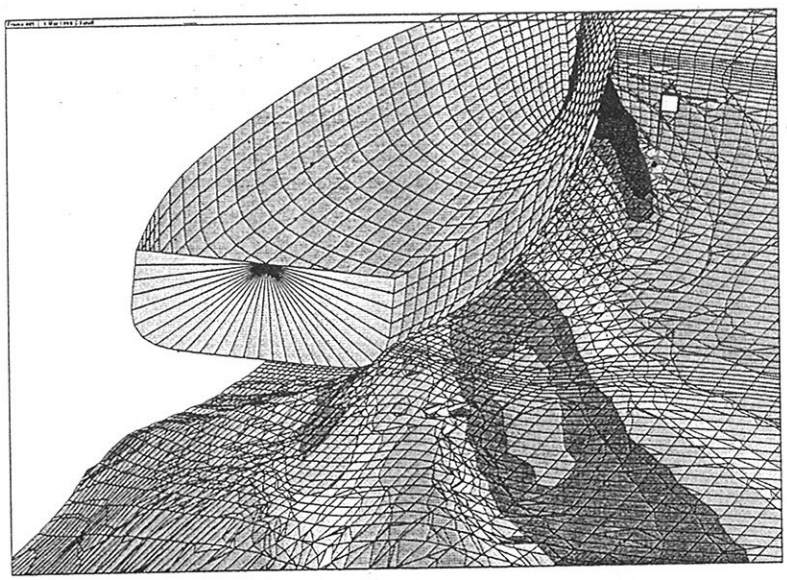

Figure 4: Flow past fast mono hull

number is 0.316. Up to 2/3 L_{PP} the numerical results compare well with the experimental data. Further downstream the numerical error and viscous effects result in an less accurate description of the wave distribution.

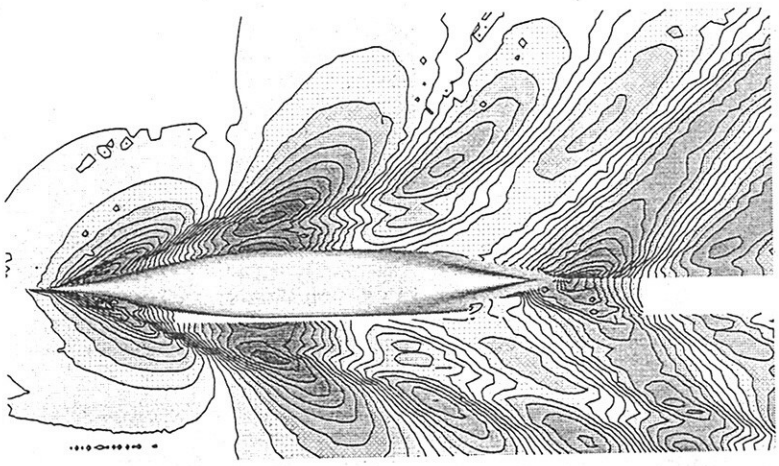

Figure 5: Comparison of measurement (bottom) and calculation (top) for the Series 60 Ship

The development of the code focuses on the introduction of a multi block technique grid in order to ease the grid generation process. This involves the identification of inter-block communication. On the base of the multi block approach the code will be parallelised in order to reduce the run time. This will allow to compute more complex configurations in the near future.

4 Literature

1. Schumann, C.: Berechnung von reibungsfreien Schiffsumströmungen unter Verwendung einer "Volume of Fluid"-Methode zur Beschreibung der freien Wasseroberfläche, "Ph. D. Thesis, Hamburg 1999

2. Schumann, C.: "Berechnung von Schiffsumströmungen mit brechenden Wellen, HSVA Report 1624

Free surface flows

Håvard Holm* and Bjørnar Pettersen†
Department of Marine Hydrodynamics
Norwegian University of Science and Technology (NTNU), N-7491 Trondheim, Norway

Abstract Governing equations describing flows are discretized by a finite volume method and the method of artificial compressibility is used to step time. The resulting equations are solved using an approximate Newton relaxation approach. A method for stepping the free surface in time in a Navier-Stokes solver has been developed. Conservation of the volume of fluid is directly linked to the residual of the mass conservation equation. Development of the free surface is ensured by a moving grid. The algorithm is tested out for a light sloshing problem. The ability of the method to handle the contact problem is studied. The code is validated against analytical results.

1 Introduction

In recent years, CFD has become a useful design tool in several marine application areas. The increase in computer capacity has made it possible to model more complex physical problems, i.e. the nonlinear free surface elevation around a moving ship. The goal of this work is to study the influence of the free surface on flows where viscous effects may be important.

The free surface is normally predicted by surface tracking methods or surface capturing methods. Surface capturing methods can handle complex surface configurations, like breaking waves. This is important when studying the bow-wave of a ship. It is generally hard to implement correct boundary conditions for surface capturing methods.

Free surface tracking methods uses a mesh that is fitted to the free surface as it develops. A time dependent mesh must therefore be incorporated. The method can not handle highly deformed free surfaces because of highly stretched elements or even grid folding. It is however possible to implement free surface boundary conditions accurate. This method is chosen in the present study because details of flow very close to the free surface are of interest.

This is part of a larger effort started at NTNU, where we during a 6 year Strategic University Program will focus on modeling and simulation of viscous flow. Special emphasis will be given to marine engineering and free surface flow problems (http://www.math.ntnu.no/cse/).

*haavard.holm@marin.ntnu.no
†bjornar.pettersen@marin.ntnu.no

2 Navier-Stokes solver

2.1 Governing equations

The governing equations are the two-dimensional time dependent incompressible Navier-Stokes equations. Laminar flow and constant viscosity are assumed. p, u and v denotes the pressure and Cartesian velocity components respectively and $\dot{r}$ represents the velocity of the boundary.

In integral form the Navier-Stokes equations can be expressed as :

$$\frac{d}{dt}\int_{\Omega} U' dV + \int_{\partial\Omega} (F - U'\dot{r})\,\vec{n} ds = 0 \qquad (1)$$

where F is the flux vector, and we define

$$U = \begin{bmatrix} p \\ u \\ v \end{bmatrix}, U' = \begin{bmatrix} 1 \\ u \\ v \end{bmatrix} \qquad (2)$$

F can be split into two parts :

$$F = F_{inv} + F_{vis} \qquad (3)$$

The component of F_{inv} along $\vec{n}$ is

$$F_{n,inv} = \begin{bmatrix} \beta v_n \\ uu_n + pn_x \\ vu_n + pn_y \end{bmatrix} \qquad (4)$$

β is a positive constant of artificial compressibility, typical value is 1. p is the modified pressure, defined by

$$p = p^* + \frac{y}{F_r^2} \qquad (5)$$

where p^* is the original pressure and F_r is the Froude number $\frac{\bar{U}}{\sqrt{g\bar{L}}}$. $\bar{U}$ and $\bar{L}$ is characteristic velocity and length respectively.

$$F_{n,vis} = A_{n,x}\frac{\partial U}{\partial x} + A_{n,y}\frac{\partial U}{\partial y} \tag{6}$$

$$A_{n,x} = \begin{pmatrix} 0 & 0 & 0 \\ 0 & 2\mu & \mu \\ 0 & 0 & \mu \end{pmatrix} A_{n,y} = \begin{pmatrix} 0 & 0 & 0 \\ 0 & \mu & 0 \\ 0 & \mu & 2\mu \end{pmatrix} \tag{7}$$

where μ is the kinematic viscosity.

2.2 Boundary conditions

Light sloshing (no breaking waves) in a rectangular tank is calculated. Boundary condition on the vertical and horizontal walls are imposed as no slip condition unless otherwise stated in the text. At the free surface we have two boundary conditions: the kinematic and the dynamic condition. The kinematic condition states that a particle on the free surface will remain on the free surface. This can be mathematically formulated as :

$$(\mathbf{V} - \mathbf{V_{fs}})\,\mathbf{n} = 0 \tag{8}$$

where $\mathbf{V_{fs}}$ is the velocity vector of the free surface interface, $\vec{\mathbf{n}}$ is the normal vector of the free surface. This boundary condition is used to step the free surface in time. The dynamic boundary condition states that the stress tensor should be continuous over the free surface. Surface tension and viscous effects at the free surface are neglected, which results in zero stress tensor. Due to the zero tangential stress condition, the velocity boundary condition is zero gradient extrapolation. The zero normal stress condition lead to the Dirichlet condition for pressure on the free surface : $p = p_a + h/F_r^2$, where p_a is the atmospheric pressure and h is the wave height.

2.3 Spatial disctretization

A finite volume method is used to discretize the domain. The spatial disctretization is divided into a viscous part and an inviscous part. F_{vis} is calculated using a central differencing scheme and F_{inv} is calculated using Roe's upwind scheme with second-order differencing. This scheme is briefly reviewed here. The extension to two or three dimensions is straight forward by applying the one-dimensional scheme independently in each coordinate direction.

Roe showed the following :

$$F(U^+_{i+\frac{1}{2}}) - F(U^-_{i+\frac{1}{2}}) = A(U_{i+\frac{1}{2}})(U^+_{i+\frac{1}{2}} - U^-_{i+\frac{1}{2}}) \tag{9}$$

$U_{i+\frac{1}{2}}$ should be evaluated as the Roe average. Pan and Chakravarthy [1] have shown that for incompressible flow, this average turns out to be a simple arithmetic average :

$$U_{i+\frac{1}{2}} = \frac{1}{2}\left(U^+_{i+\frac{1}{2}} + U^-_{i+\frac{1}{2}}\right) \tag{10}$$

By Roe's scheme, the numerical flux is then given by

$$\begin{aligned} F_{i+\frac{1}{2}} &= \frac{1}{2}(F(U^-_{i+\frac{1}{2}}) + F(U^+_{i+\frac{1}{2}})) \\ &- \frac{1}{2}(A^+_{i+\frac{1}{2}} + A^-_{i+\frac{1}{2}})(U^+_{i+\frac{1}{2}} - U^-_{i+\frac{1}{2}}) \end{aligned}$$

Here $U^-_{i+\frac{1}{2}}$ and $U^+_{i+\frac{1}{2}}$ are extrapolated values of the conserved variable at the left and right side of the cell surface. $A^\pm_{i+\frac{1}{2}}$ are given by

$$A^\pm_{i+\frac{1}{2}} = R_{i+\frac{1}{2}}\Lambda^\pm_{i+\frac{1}{2}}R^-_{i+\frac{1}{2}} \tag{11}$$

here $R_{i+\frac{1}{2}}$ is the right eigenvector of $A_{i+\frac{1}{2}}$, which is the Jacobian of $F(U_{i+1})$. The diagonal matrices $\Lambda^\pm_{i+\frac{1}{2}}$ are the split eigenvalue matrices corresponding to $R_{i+\frac{1}{2}}$.

A first order scheme is obtained by simply setting $U^-_{i+\frac{1}{2}} = U_i$ and $U^+_{i+\frac{1}{2}} = U_{i+1}$ Schemes of higher order are obtained by defining $U^-_{i+\frac{1}{2}}$ and $U^+_{i+\frac{1}{2}}$ by higher order extrapolations. The scheme is then called a MUSCL (Monotonic Upstream Schemes for Conservation Laws) scheme.

2.4 Implicit time integration

After spatial integration, we are left with :

$$\frac{d}{dt}(DU') = R(U) \tag{12}$$

where D is the volume of the cell. The most general two-step scheme of Equation 12 is implemented:

$$\begin{aligned} &(1+\xi)\frac{D_i^{n+1}}{\Delta t}U'^{n+1}_i \\ -\ &(1+2\xi)\frac{D_i^n}{\Delta t}U'^n_i + \xi\frac{D_i^{n-1}}{\Delta t}U'^{n-1}_i \\ =\ &\Theta R_i^{n+1} + (1-\Theta+\phi)R_i^n - \phi R_i^{n-1} \end{aligned} \tag{13}$$

Following the same algorithm as Belov et al. [2]

$$\begin{aligned} R^*(U^{n+1}) &= \Theta R_i^{n+1} + (1-\Theta+\phi)R_i^n - \phi R_i^{n-1} \\ &- (1+\xi)\frac{D_i^{n+1}}{\Delta t}U'^{n+1}_i \\ &+ (1+2\xi)\frac{D_i^n}{\Delta t}U'^n_i - \xi\frac{D_i^{n-1}}{\Delta t}U'^{n-1}_i \\ &= 0 \end{aligned} \tag{14}$$

According to Newtons method, a correction can be found :

$$\Rightarrow \left(\Theta\frac{\partial R}{\partial U} - (1+\xi)\frac{D_i}{\Delta t}\right)\Delta U + R^*(U^l) = 0 \tag{15}$$

An important consequence is that before we find the new velocities, we must have updated values of the fluxes, grid location and grid velocities.

3 Evolution of the free surface

To step the free surface in time, the kinematic boundary condition, equation 8, on the free surface is used. Traditionally the boundary condition is rewritten to :

$$\frac{\partial h}{\partial t} = v - u\frac{\partial h}{\partial x} \tag{16}$$

For a cell centered discretisation v and u are usually taken as the average of the cells on the left and right hand side closest to the free surface. $\frac{\partial h}{\partial x}$ is usually calculated using a higher order upwind scheme.

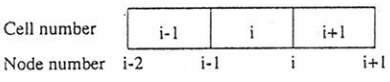

Figure 1: Numbering of nodes and cells

The method has been used with success for a wide range of applications. For some applications it is very important to preserve the mass. The sloshing problem is one example. If the mass increase or decrease, the eigenfrequency will change accordingly and the response will be different. It is therefore important to have a method where the conservation of mass is automatically preserved. The kinematic condition at free surface states that the free surface should be moved so that the mass flux through the uppermost cell face is zero. The mass flux is calculated as :

$$\dot{m} = \mathbf{V}\cdot\mathbf{s} - \mathbf{V_{fs}}\cdot\mathbf{s} \tag{17}$$

$\mathbf{V}$ and $\mathbf{V_{fs}}$ is the velocity vector of the fluid and the free surface respectively. $\mathbf{s}$ is the surface vector. The kinematic condition states that $\mathbf{V_{fs}}$ should be adjusted (through motion of the nodes on the free surface) so that the mass flux is zero. In this work the wave height is restricted to be single valued. We can therefore restrict the nodes to move vertically.

$$\begin{aligned} \Delta v_{fs} &= -\dot{m}^l/s_x \\ h_c^{l+1} &= h_c^l - \alpha\,\dot{m}/s_x * dt \end{aligned} \tag{18}$$

where α is an underrelaxing factor and h_c^l is the position of the center of the uppermost cell face at Newton iteration l. At the time when we are to move the nodes, $\dot{m}^l$ are not calculated yet (dependent on h_c^l). Therefore we replace $\dot{m}^l$ with :

$$\dot{m}^l \approx \dot{m}^{l-1} + \Delta(V\cdot s) \tag{19}$$

Where $\Delta(V\cdot s) = V^l\cdot s^l - V^{l-1}\cdot s^{l-1}$. When the Newton iterations converge, $\Delta(V\cdot s)\to 0$ and we are left with $\dot{m}^l = \dot{m}^{l-1}$.

This gives us N equations, where N is the number of cells at the free surface. The number of nodes to move is N+1. We experience that a lot of care should be put into algorithms that moves the nodes. For equally spaced grids, one could try to move the nodes according to :

$$\begin{aligned} h_n^i &= .5*(h_c^i + h_c^{i+1}) \\ h_n^N &= h_c^N \\ h_n^0 &= h_c^1 \end{aligned} \tag{20}$$

Doing this iteratively will reduce the mass flux through the uppermost cell face until a certain limit. This procedure will after some iterations end up in an oscillating mass flux, see figure below.

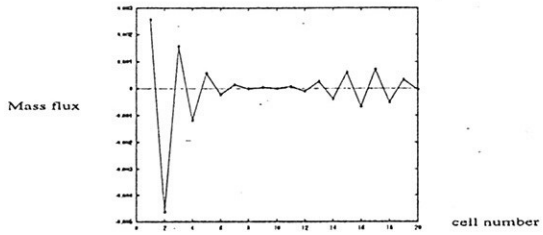

Figure 2: Mass flux $\dot{m}$, as function of

The magnitude of these oscillations is not nessecarily big, but their presence is hard to remove ($h_c^i + h_c^{i+1} \approx 0$). To get rid of the oscillations the following method will work:

1. Divide the free surface into a small number of superblocks.

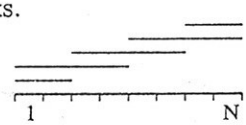

2. The mass-flux over each superblock is calculated.

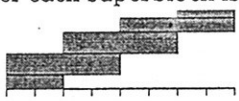

3. Distribute the mass-flux smoothly according to the indicated scheme in the figure below.

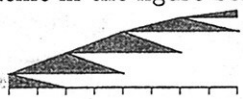

4. goto step 1, but use smaller superblocks.

For the last iteration, we have the same scheme as for Equation 20. To ensure a stable solution the last term in Equation 19 is rewritten to :

$$\Delta(V\cdot s) = \left(v - u\frac{\partial h}{\partial x}\right)s_x \tag{21}$$

$\frac{\partial h}{\partial x}$ is calculated using an upwind scheme. Using this algorithm , a smooth surface will evolve and global conservation of mass will be preserved. No sort of filtering is nessesary. The key point here, is to use the same numerical mass flux that are used when calculating the residuals. The question of conservation of mass is then linked to the residual of the mass flux.

4 Application: Light Sloshing

The sloshing problem is used as an example because of it's well defined boundary conditions. The conservation of mass is also very controllable and important.

The initial mesh is given by 20 horizontal amd 20 vertical points uniformly distributed. Start condition is given in figure 2.

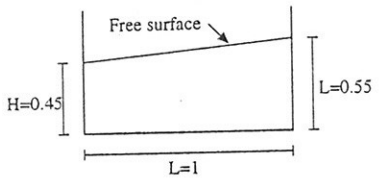

Figure 3: Initial geometry

To check out the mass conservation, the fluid volume is plotted as functions of Newton iterations in figure 3. We observe that the change in volume decreases rapidly as function of Newton iterations.

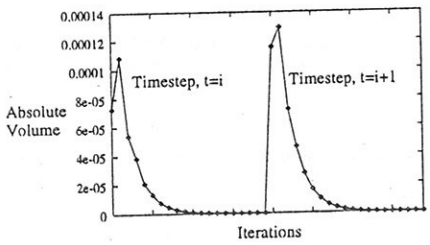

Figure 4: Volume as functions of Newton iterations at two typical timesteps

A special problem for viscous free surface flow is the contact problem. The fluid will adhere to the wall, due to the noslip condition. A viscous calculation is

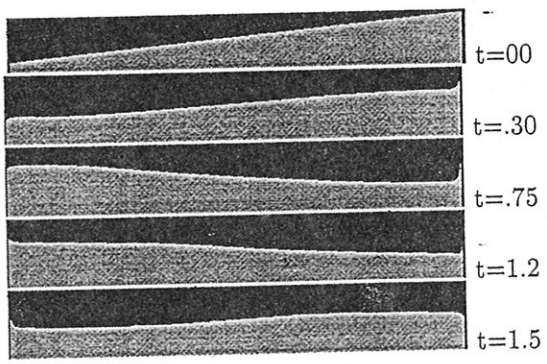

Figure 5: Free surface at different timesteps $R_e = 1000$

performed, $R_e = 1000$, $F_n = .5$, initial geometry is shown in figure 2, but now we use 80 grid points in the horizontal direction. Smallest elementsize (closest to the wall) is 0.00113, which is sufficient to resolve the boundary layer. Results are shown in figure 4 and 5.

In another example, the initial surface elevation is set to $0.01 * sin()$. Both the depth and the height are set

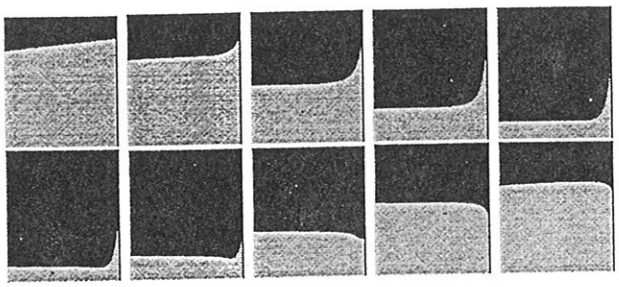

Figure 6: Close look at right corner, t=0, .2, .4, .6, .8, 1., 1.2, 1.4, 1.6, 1.8

to 1. Linear theory can now be applied. Viscosity are neglected and $F_r = 1$. For standing waves linear theory gives the period $T = 2\pi/\sqrt{\pi \tanh(\pi)} = 3.5515$. Calculated free surface elevation at the wall are given in figure 6. The calculated period is 3.555, which agrees

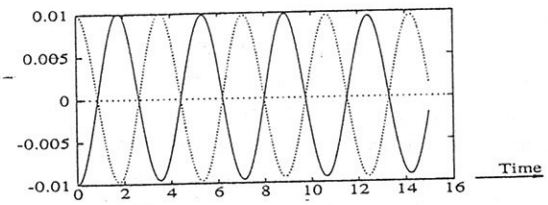

Figure 7: Free surface elevation at left and right wall.

very well with linear theory. The damping that can be seen in figure 5 (decrease in amplitude) is assumed to be due to numerical damping, and should decrease with finer mesh.

The goal of this work is to study the influence of the free surface on flows where viscous effects may be important. The sway problem is one such example. Figure 6 shows the velocity contours and the free surface elevation around a ship section at a given time.

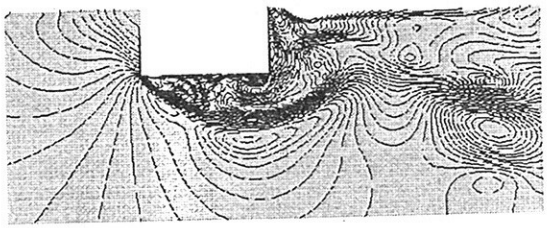

Figure 8: Velocity contours and free surface elevation for 2D flow around a rectangular ship cross section

References

[1] D. Pan et al, *Uniform formulation for Incompressible Flows*, AIAA-89-0122, Jan. (1989).

[2] Andrey Belov et al. *A new implicit algorithm with multigrid for unsteady incompressible flow calculations*, AIAA, Aerospace Sciences Meeting, 33rd, Reno, NV, Jan. 9-12, 1995.

A level-set approach for unsteady free surface flows

A. Iafrati, E.F. Campana,
INSEAN - Via di Vallerano, 139 - 00128 - Roma (ITALY)

1 Abstract

In this paper an unsteady Navier-Stokes solver is coupled with a level-set approach to describe the free surface motion. As a first step the method is validated by comparisons with other numerical techniques. The numerical procedure is then applied to simulate the free surface motion induced by the sudden start of an high bump.

The analysis cover the successive stages of the breaking phenomenon: the steep wave evolution, the jet formation, the splash-up and the entrainment of the air. As a results of the adopted numerical approach, the velocity field in both air and water domains is computed.

On the base of experimental observation, available in literature, the qualitative behavior during and after the overturning phase is correctly reproduced.

2 The Navier-Stokes solver

To simulate free surface flows the level-set technique [1, 2] has been coupled with a finite difference Navier-Stokes solver in generalized coordinates. This latter is essentially similar to that described by Zang *et al.* [3], even though some changes have been made to account for density and viscosity variations.

In generalized coordinates the Navier-Stokes equation for an incompressible fluid are:

$$\frac{\partial U_m}{\partial \xi_m} = 0 \tag{1}$$

$$\frac{\partial}{\partial t}(J^{-1}u_i) + \frac{\partial}{\partial \xi_m}(U_m u_i) = -\frac{1}{\varrho}\frac{\partial}{\partial \xi_m}\left(J^{-1}\frac{\partial \xi_m}{\partial x_i}p\right) + J^{-1}q_i + \frac{1}{\varrho}\frac{\partial}{\partial \xi_m}\left(\mu G^{mn}\frac{\partial u_i}{\partial \xi_n}\right) \ , \tag{2}$$

where x_i and u_i are the $i-$th cartesian coordinate and velocity component, respectively, p is the pressure, μ and ϱ are the local values of the dynamic viscosity and fluid density. The body force for unit mass is denoted by q_i, J^{-1} is the inverse of the Jacobian, and

$$U_m = J^{-1}\frac{\partial \xi_m}{\partial x_j}u_j \quad G^{mn} = J^{-1}\frac{\partial \xi_m}{\partial x_j}\frac{\partial \xi_n}{\partial x_j} \ ,$$

are the volume flux normal to the ξ_m iso-surface and the *mesh skewness tensor*, respectively.

Cartesian velocity components and pressure are defined at the cell center while volume fluxes, defined at the mid points of the cell faces, are computed by a quadratic upwind interpolation of the cartesian velocities.

A semi-implicit scheme is adopted for the time integration of equation (2). Convective terms are accounted for explicitly by the Adam-Bashfort scheme, while, to avoid the viscous stability limit, a Crank-Nicolson discretization has been employed for the diagonal part of the diffusive operator. A variable time step integration is carried out according to the CFL constraint.

The discrete form of equation (2) is solved through a fractional step approach. Namely, an auxiliary velocity field is introduced and it is computed by neglecting the pressure term in the momentum equation. The velocity field at the new time-step is then corrected by adding the gradient of a scalar function to the auxiliary velocity field. The pressure corrector is computed by solving the Poisson equation that arises by enforcing the continuity equation (1).

Turbulence modeling and surface tension effects are not yet included in the numerical procedure.

3 Dynamics of the air-water interface

In the level-set approach a signed normal distance d from the air-water interface is defined at $t = 0$, being $d > 0$ in water, $d < 0$ in air and $d = 0$ on the interface. During the motion the distance function moves with the fluid and it is updated by the transport equation:

$$\frac{\partial d}{\partial t} = -\boldsymbol{u} \cdot \nabla d \ . \tag{3}$$

Fluid properties, such as density and viscosity, vary with the distance d. To avoid instabilities in the evaluation of the derivatives, due to large variations of fluid properties, the jump is spread over a small region close to the interface. As a consequence, for the property f it is assumed $f(d) = f_w$ if $d > \alpha$, $f(d) = f_a$ if $d < -\alpha$ and

$$f(d) = (f_w + f_a)/2 + (f_w - f_a)/2 \ \sin(\pi d/(2\alpha)) \ ,$$

otherwise. Usually the thickness α is chosen so that the jump cover three or four cells. The influence of α on the free surface dynamics will be discussed in the following.

Due to the transport operated by equation (3), the function d will no more represent a distance later. In order to keep constant the width of the jump region in time, the iso-surface at $d = 0$ is reconstructed and the normal distance from the interface is reinitialized at each time step.

4 Results

The numerical method has been firstly applied to the sloshing in a tank and comparisons have been established with results obtained for an inviscid fluid by Lilek [4]. This test problem is useful to evaluate how the numerical procedure is able to conserve the mass and to check the grid sensitivity.

The initial free surface height has a sinusoidal variation $y(x) = 1 - 0.01 \sin(x\pi)$ for $x \in (-.5, .5)$ so that the height is $h_l = 1.01$ on the left wall of the tank and $h_r = 0.99$ on the right one. The gravity acceleration is $g = 1$ and the

following values are employed for densities and dynamic viscosities: $\varrho_w = 1000, \varrho_a = 1.25, \mu_w = 10^{-3}, \mu_a = 18\ 10^{-6}$. For the numerical simulation with the level set technique, the computational domain extends from $y = 0$ to $y = 1.4$ in the vertical direction.

A first computation has been performed on a grid having 20 cells equally spaced in the horizontal direction and 140 cells in the vertical direction, suitably clustered close to the free surface region. In particular in the region $y \in (.985, 1.015)$ a uniform vertical spacing $\Delta y = 0.0005$ has been employed. To evaluate the grid sensitivity the coarse mesh is refined twice by halving the cell size in both directions. The width of the jump region is chosen to be $\alpha = 0.001$ for the coarse and medium grid, while it is $\alpha = 0.0005$ for the finer grid.

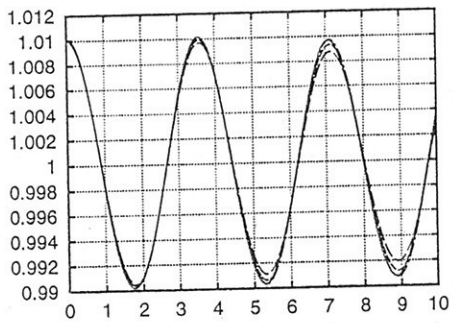

Fig.1: *Time history of the free surface elevation on the left wall of the tank.* (——) *Lilek,* (– – –) 20 × 140, (- - - -) 40 × 280, (– – –) 80 × 560.

Finally, to evaluate the effect of the width of the jump region, the computation on the 40 × 280 grid has been also performed with $\alpha = 0.0005$.

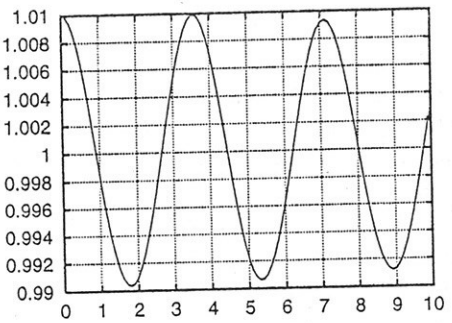

Fig.2: *Effect of the width of the jump on the free surface dynamics.* (——) *jump spread on 8 cells,* (– – –) *jump spread on 4 cells.* (grid 40 × 280)

Comparisons with inviscid Lilek's results, plotted in Fig.1, have been established in terms of the free surface height on the left wall of the tank. As was to be expected, a fine resolution is needed to avoid an excessive damping while the use of different width of the jump region does not affect the free surface dynamics (Fig.2).

In Fig.3 the time history of the total mass is shown for several grids. Due to errors occurring in the reconstruction of the interface, a fine resolution is required to achieve a good mass conservation. Jumps in the time history of the mass occurs when the free surface elevation takes its maximum and minimum values. Actually, in these phases velocities are very low and the time step grows according to a CFL constant time integration.

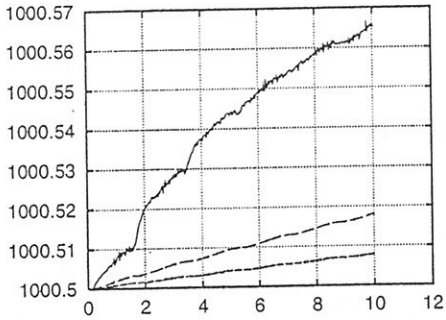

Fig.3: *Time histories of the total mass for several grid resolutions:* (——) 20 × 140, (– – –) 40 × 280, (- - - -) 80 × 560. (Initial value 1000.5)

As a further verification, the flow over a bump has been simulated and results are compared with those obtained by a standard panel method in order to assess the capability of the numerical procedure to model the wave dynamics.

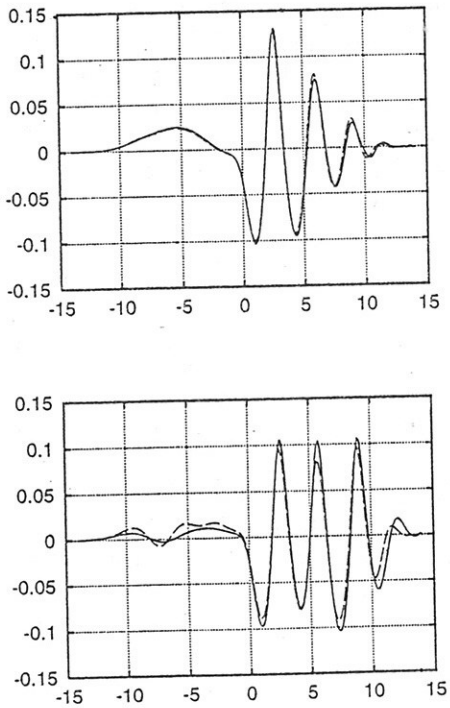

Fig.4: *Comparisons between level-set* (——) *and panel method* (– –) *at two times:* $t = 20$ (up) *and* $t = 150$ (down). *The iso-line at* $\varrho = (\varrho_a + \varrho_w)/2$ *is represented for the level-set.*

The bump is placed on the bottom of the channel and has a geometric profile $y(x) = \delta(1 - 2x^2/a^2 + x^4/a^4)$ for $x \in (-a, a)$, δ being the maximum height of the bump. The still water level is $h = 1$. At $t = 0$ the bump is suddenly started at $U = 1$.

As a first application, the resulting wavy flow over a bump having a maximum height $\delta = 0.1$ and extending

from $x = -0.5$ to $x = 0.5$, has been analyzed. The flow is simulated in a frame of reference moving with the bump. A value $g = 2$ has been assumed for the acceleration of gravity. Both in the level-set approach and in the panel method, numerical beach models [5, 2] have been employed at the two ends of the computational domain $x \in (-14, 14)$. A free slip boundary condition is applied on the bottom of the channel. The comparison, depicted in Fig.4, shows an excellent agreement between the two approaches at least before the wave disturbances reach the damping regions. Successively, the different model employed to damp out wave disturbances leads to different wave reflections on the domain and then the agreement becomes slightly worst.

In the above applications the numerical procedure here presented worked very well, but, however, it is not the most efficient method. Actually, the level-set technique is mainly important when complicated free surface configurations occur. For this reason the flow over a bump extending from $x = -1$ up to $x = 1$ with a maximum height $\delta = 0.4$ has been analyzed. Dynamic viscosities are $\mu_w = 10^{-1}, \mu_a = 18\ 10^{-4}$, in water and air, respectively. In this conditions the application of panel method predicts the occurrence of a breaking wave at $t \simeq 3.6$ and the simulation through the level-set technique is again in good agreement with the panel method before the wave breaks (Fig.5).

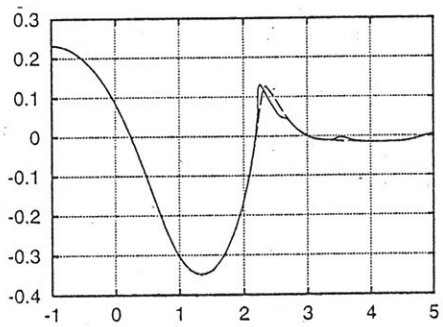

Fig.5: *Comparisons between level-set (——) and panel method (– –) for a bump with maximum height $\delta = 0.4$ at $t = 3.6$.*

Through the level-set technique the numerical simulation has been performed for large times and successive configurations are reported in Fig.6. The formation of several plunging waves and the consequent splash-up is reproduced. Even though a quantitative comparison has not been made, a qualitative agreement with experimental observation is achieved [6].

In Fig.7 the stream traces in the region where the falling jet hits the free surface are shown both in the air and water domains. The thick stripe represents the variable density region. While a quite regular behavior occurs in water, recirculation regions in air are induced by the falling jet and by the separation behind the wave profile.

In Fig.8 the corresponding velocity field is shown: to emphasize the local behavior the uniform value of velocity $U = 1$ has been subtracted to the horizontal component. A strong velocity characterizes the jet falling on to the water surface and, by consequence, an intense velocity field is induced by the escaping air leading to the formation of the two recirculation regions shown in Fig.7.

Acknowledgment

This work was supported by the *Ministero dei Trasporti e della Navigazione* in the frame of INSEAN research plan 1997-99.

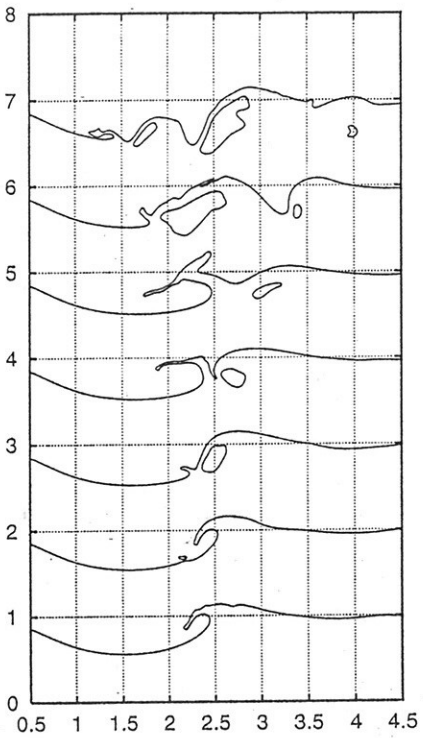

Fig.6: *Free surface configurations at several times: $t = 5.5, 6, 6.5, 7, 7.5, 8, 8.5$.*

References

[1] Sussman M., Smereka P. and Osher S., (1994) *A level-set approach for computing solutions to incompressible two-phase flow*, J. Computational Physics, vol. **114**.

[2] Vogt M., Larsson L. (1998) *The level-set technique applied to 2-d wave problems*, First NuTTS' Conference, Hamburg.

[3] Zang Y., Street R.L., and Koseff J.R., (1994) *A non staggered grid, fractional step method for time-dependent incompressible Navier-Stokes equations in curvilinear coordinates*, J. Computational Physics, vol. **114**.

[4] Ferziger J.H., Peric M., (1996) Computational method for fluid dynamics, Springer-Verlag, Berlin.

[5] Baker G.R., Meiron D.I. and Orszag S.A., (1989) *Generalized vortex methods for free surface flow problems. II: Radiating waves*, J. Sci. Comput., vol. **4**.

[6] Bonmarin P., (1989) *Geometric properties of deep-water breaking waves*, J. Fluid Mechanics, vol. **209**.

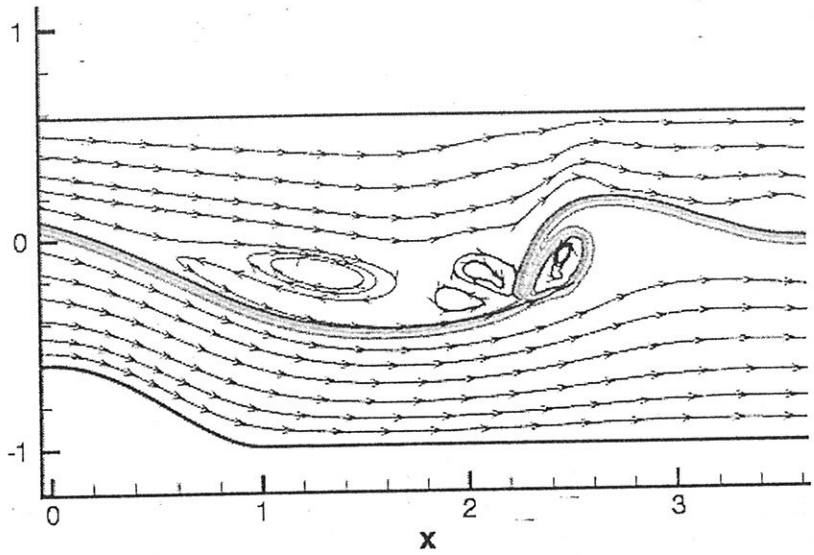

Fig.7: *Stream traces in the region where the jet hits the free surface.*

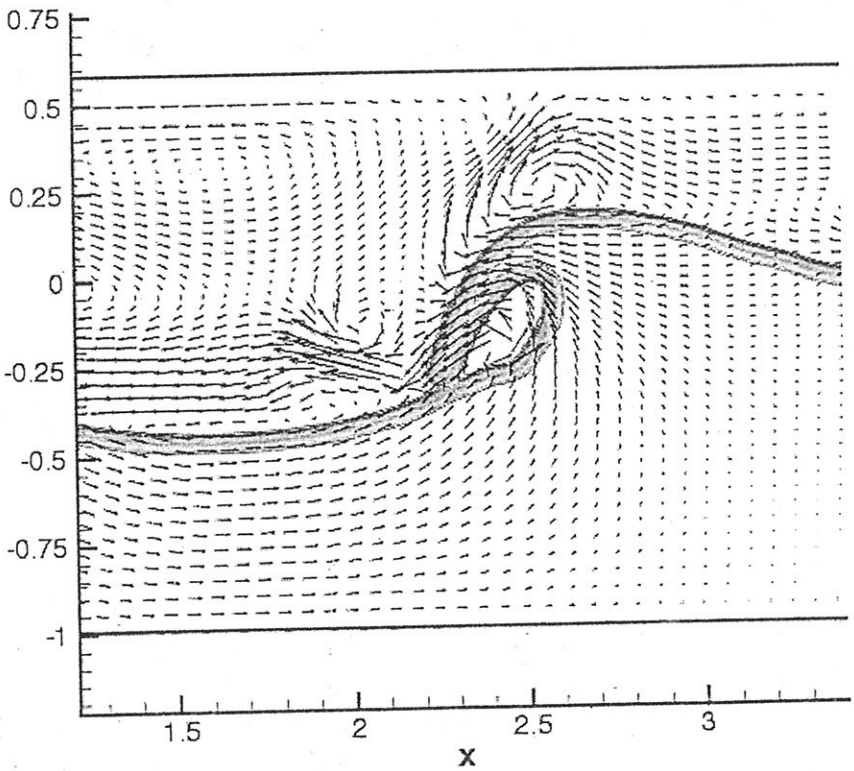

Fig.8: *Velocity field.*

Computation of Ship Wave and Resistance using a RANS solver

S. ISHIKAWA and H. YASUKAWA, Nagasaki Experimental Tank, MHI

Introduction

RANS solver has been used as a design tool for the hull form improvement. We applied the RANS solver including free-surface to actual hull form design. Waves and resistance for 2 vessels with different bow shape were computed. The usefulness of RANS solver is shown through comparison with the model experiments.

RANS solver

Our RANS solver is based on the code developed by *Hino(1994)*. The outline is as follows:

- N-S equation with artificial compressibility
- Finite-volume approach for spatial discretization
- Cell-centered layout for flow variables (u,v,w,p)
- Convective flux: upwind scheme based on the flux difference splitting
- Viscous flux: 2nd-order central differential
- Turbulence model: Baldwin-Lomax Model
- Free-surface: Moving grid system & Multigrid technique

Computation of Wave Pattern and Resistance

Fig.1 shows the comparison of wave patterns between the computation and experiment for Fn=0.296 & 0.391. Then, Reynolds number is almost 10^7. Wave height distribution near ship hull is well predicted for both cases. However, the remarkable damping is observed in the far field and Kelvin wave pattern is not captured. That is due to coarse grid on the free-surface in far field. Further, we confirmed that the wave profile and longitudinal cut of the waves in near field by computation agree well with those by experiment.

Next, the resistance acting on the ships was computed. As a result of the computation, we found that residual resistance is well predicted although the total resistance is underestimated. And the resistance difference between 2 ships is well predicted in quantity.

The detailed comparison will be presented in the symposium.

References

Hino, T. (1994): *A Study of Grid Dependence in Navier-Stokes Solutions for Free Surface Flows around a Ship Hull*, J. of the Society of Naval Architects of Japan, Vol.176.

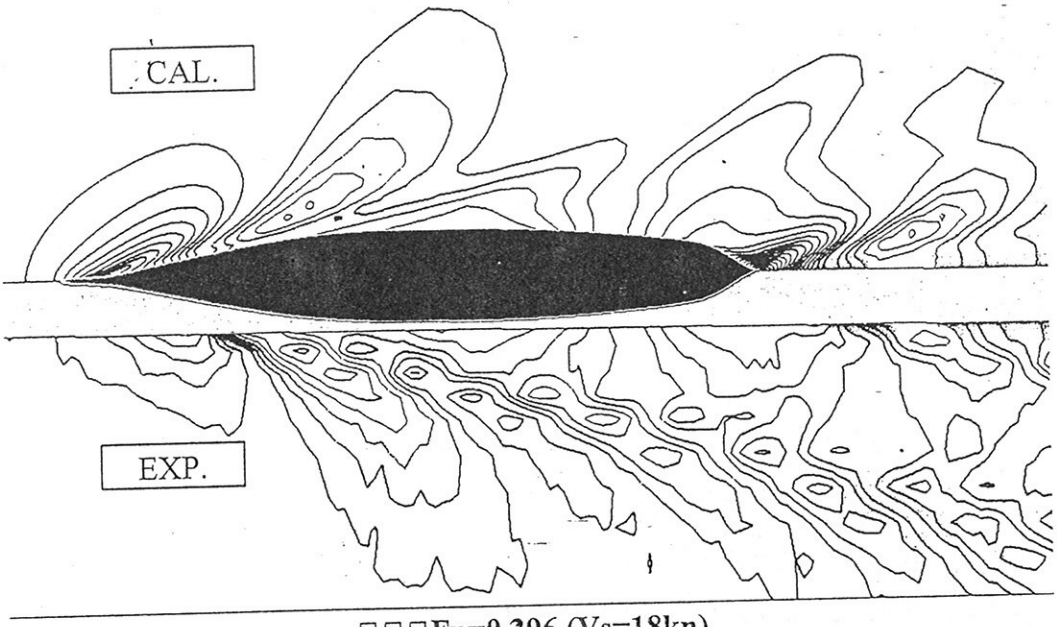

□□□Fn=0.296 (Vs=18kn)

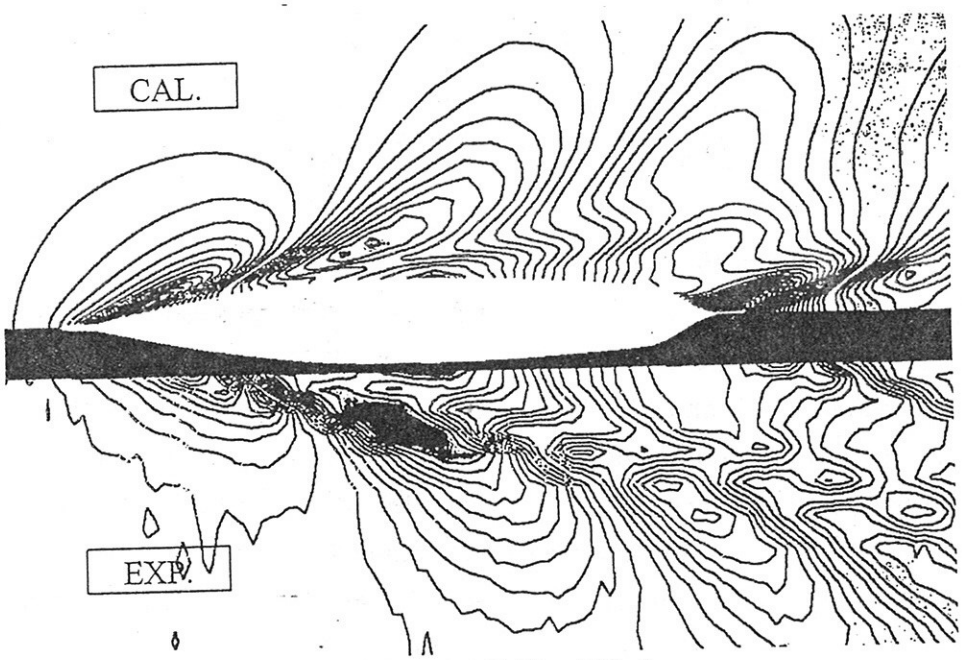

(2)Fn=0.361(Vs=22kn)

Fig.1 Comparison of wave patterns

(Abstract for the Numerical Towing Tank Symposium '99, August 1999)

Prediction of Diffraction Waves of a Blunt Ship with Forward Speed Taking account of the Steady Nonlinear Wave Field

Hidetsugu IWASHITA
Engineering Systems, Hiroshima University
1-4-1 Kagamiyama, Higashi-Hiroshima 739-8527, JAPAN

1 Introduction

When the ship advances in a seaway, the wave system generated by the ship consists of the time-independent steady wave field and the time-dependent unsteady wave field, as well known. Both wave fields are then not independent. The analysis based on the potential theory derives some influence of the steady wave field on the unsteady wave field through the free surface and the body surface boundary conditions. This influence can be considered to become negligible as the disturbance of the steady wave field becomes more remarkable due to a blunt ship hull form and/or higher forward speed.

Iwashita et al.(1993,1994) systematically investigated the influence of the steady wave field on the wave pressure, hyrdodynamic forces and ship motions of a blunt VLCC advancing in oblique short waves. The 3-D Green function method (GFM) was mainly used for the analysis taking account of the influence of the steady flow in the body boundary condition through m_j-term, and it was confirmed that its influence was significant especially in the low frequency range and its consideration was not yet sufficient to predict physical quantities described above in good accuracy. Consecutively the influence of the steady flow in seakeeping computations through the free surface boundary condition were studied by *Iwashita & Bertram (1997)* and *Iwashita et al.(1998A,B)* applying the Rankine panel method (RPM). It has been made clear up to now that the estimation accuracy of the wave pressure is improved in some quantity by taking into account the influence of the steady non-uniform flow in both the free surface and body surface conditions, but its improvement is not yet sufficient against our expectation. More accurate estimation may be expected only by fully taking into account the steady wave field beyound the framework of the linear theory.

In this paper we apply a desingularized Rankine panel method (RPM) presented by *Jensen et al.(1986)* and *Bertram (1990)* in order to enable to fully capture the influence of the steady wave field. The steady problem is solved so that the fully nonlinear free-surface condition is satisfied, and the influence terms of the steady wave field on the unsteady wave field are evaluated by using the solutions obtained here. The unsteady boundary value problem is linearized assuming the small amplitude of the incident wave and the ship motions and is formulated so that the boundary conditions are satisfied on the exact steady free surface and wetted surface on the body. The method is applied to a simple Wigley model for the validation and a Series-60 model for predicting diffraction wave. Numerical results are compared with experiments and another practical computation methods, and the influence of the steady wave field on the unsteady wave field is discussed.

2 Formulation

We consider a ship advancing at constant forward speed U in oblique regular waves encountered at angle χ, Fig.1. The ship motions $\Re[\xi_j e^{i\omega_e t}](j = 1 \sim 6)$ and the wave amplitude A of the incident wave are assumed to be small. ω_0 is the circular frequency and K the wave number of the incident wave. The encounter circular frequency is $\omega_e(= \omega_0 - KU\cos\chi)$. The linear theory is employed for this problem assuming ideal potential flow.

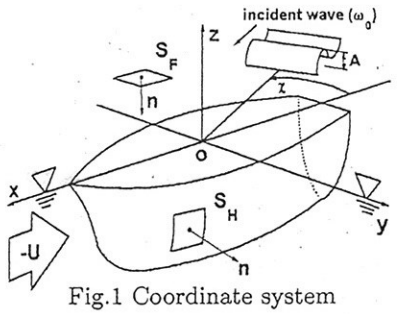

Fig.1 Coordinate system

The total velocity potential Ψ of the fluid governed by Laplace's equation can be expressed as

$$\begin{aligned}\Psi(x,y,z;t) &= U\Phi(x,y,z) + \Phi_t(x,y,z;t) \\ &= U\Phi(x,y,z) + \Re[\phi(x,y,z)e^{i\omega_e t}] \end{aligned} \quad (1)$$

where

$$\left.\begin{aligned}\phi &= \frac{gA}{\omega_0}(\phi_0 + \phi_7) + i\omega_e \sum_{j=1}^{6} \xi_j \phi_j \\ \phi_0 &= ie^{Kz - iK(x\cos\chi + y\sin\chi)}\end{aligned}\right\} \quad (2)$$

Φ means the steady wave field and ϕ the unsteady wave field which consists of the incident wave ϕ_0, the diffraction wave ϕ_7 and the radiation wave $\phi_j(j = 1 \sim 6)$. The kinematic and dynamic boundary conditions to be satisfied on the exact free surface $z = \zeta(x,y;t)$ yields

$$\Psi_{tt} + \nabla\Psi\cdot\nabla\Psi_t + \overline{\nabla}\Psi\cdot\overline{\nabla}\Psi_t + \frac{1}{2}\overline{\nabla}\Psi\cdot\overline{\nabla}(\nabla\Psi)^2 + g\Psi_z = 0 \quad \text{on } z = \zeta \quad (3)$$

where $\overline{\nabla}$ denotes the two-dimensional Laplacian with respect to x and y. By substituting (1) into (3), the problem can be decomposed into the steady and the unsteady problems.

Then the steady wave field is solved so that

$$\frac{1}{2}\overline{\nabla}\Phi\cdot\overline{\nabla}(\nabla\Phi)^2 + K_0\Phi_z = 0 \quad \text{on } z = \zeta_s \quad (4)$$

$$\Phi_n = 0 \quad \text{on } S_H \quad (5)$$

are satisfied on the exact steady free surface $z = \zeta_s(x,y)$. S_H means the wetted surface and $K_0 = g/U^2$. A RPM developed by *Jensen et al.(1986)* is used to solve this problem

numerically. The nonlinear free surface condition (4) is satisfied by iteration scheme and the radiation condition by shifting the collocation points one panel upward.

Assuming small amplitude of the incident wave and ship motions, we can linearize the free surface condition for ϕ_j around the steady free surface $z = \zeta_s(x, y)$ obtained by solving the previous steady problem. The final form can be written as follows with corresponding body boundary condition (*Newman (1978), Bertram (1990)*):

$$
\begin{aligned}
&-K_e\phi_j + i\tau[\nabla\Phi\cdot\nabla\phi_j + \overline{\nabla}\Phi\cdot\overline{\nabla}\phi_j] \\
&+\frac{1}{K_0}\left[\overline{\nabla}\Phi\cdot\overline{\nabla}(\nabla\Phi\cdot\nabla\phi_j) + \frac{1}{2}\overline{\nabla}\phi_j\cdot\overline{\nabla}(\nabla\Phi)^2\right] + \phi_{jz} \\
&-\frac{\dfrac{\partial}{\partial z}\left[\dfrac{1}{2}\overline{\nabla}\Phi\cdot\overline{\nabla}(\nabla\Phi)^2 + K_0\Phi_z\right]}{K_0 + \nabla\Phi\cdot\nabla\Phi_z}\left(i\tau + \frac{1}{K_0}\nabla\Phi\cdot\nabla\right)\phi_j = 0 \\
&\qquad\qquad \text{on } z = \zeta_s \qquad (6)
\end{aligned}
$$

$$
\phi_{jn} = \begin{cases} n_j + (U/i\omega_e)m_j & (j = 1 \sim 6) \\ -\phi_{0n} & (j = 7) \end{cases} \quad \text{on } S_H \qquad (7)
$$

where $K_e = \omega_e^2/g$, $\tau = U\omega_e/g$ and

$$
\begin{aligned}
&(n_1, n_2, n_3) = \boldsymbol{n}, && (m_1, m_2, m_3) = -(\boldsymbol{n}\cdot\nabla)\boldsymbol{V}, \\
&(n_4, n_5, n_6) = \boldsymbol{r}\times\boldsymbol{n}, && (m_4, m_5, m_6) = -(\boldsymbol{n}\cdot\nabla)(\boldsymbol{r}\times\boldsymbol{V}), \\
&\boldsymbol{r} = (x, y, z), && \boldsymbol{V} = \nabla\Phi
\end{aligned}
$$

m_j, $\boldsymbol{V}$ and partial derivatives of Φ in (6) and (7) must be evaluated by using the steady nonlinear wave field satisfying (4) and (5).

If we express the double-body flow by φ and put $\Phi = \varphi + \phi_s$, eqs.(4) and (6) lead to the double-body flow formulations such as

$$
\begin{aligned}
&\frac{1}{2K_0}\overline{\nabla}\varphi\cdot\overline{\nabla}(\overline{\nabla}\varphi\cdot\overline{\nabla}\varphi) + \frac{1}{K_0}\overline{\nabla}\varphi\cdot\overline{\nabla}(\overline{\nabla}\varphi\cdot\overline{\nabla}\phi_s) \\
&\quad + \frac{1}{2K_0}\overline{\nabla}(\overline{\nabla}\varphi\cdot\overline{\nabla}\varphi)\cdot\overline{\nabla}\phi_s + \frac{\partial\phi_s}{\partial z} = 0 \quad \text{on } z = 0 \qquad (8) \\
&-K_e\phi_j + 2i\tau\overline{\nabla}\varphi\cdot\overline{\nabla}\phi_j + \frac{1}{K_0}\overline{\nabla}\varphi\cdot\overline{\nabla}(\overline{\nabla}\varphi\cdot\overline{\nabla}\phi_j) \\
&\quad + \frac{1}{2K_0}\overline{\nabla}(\overline{\nabla}\varphi\cdot\overline{\nabla}\varphi)\cdot\overline{\nabla}\phi_j + \frac{\partial\phi_j}{\partial z} = 0 \quad \text{on } z = 0 \qquad (9)
\end{aligned}
$$

and if simply $\varphi = -x + \phi_s$, it becomes the uniform-flow formulation.

Once the velocity potentials are obtained on the ship surface by solving the problems, hydrodynamic pressure and/or forces can be evaluated by it. The steady pressure and the wave elevation are calculated by

$$
p_s = \rho\frac{U^2}{2}[1 - (\nabla\Phi)^2] \qquad (10)
$$

$$
\zeta_s = \frac{1}{2K_0}[1 - (\nabla\Phi)^2] \quad \text{on } z = \zeta_s \qquad (11)
$$

where ρ is the density of the fluid.

The unsteady pressure $\Re[pe^{i\omega_e t}]$ is given as follows (*Timman & Newman (1962)*):

$$
p = -\rho(i\omega_e + U\boldsymbol{V}\cdot\nabla)\phi - \rho\frac{U^2}{2}\sum_{j=1}^{6}\xi_j(\boldsymbol{\beta}_j\cdot\nabla)(\boldsymbol{V}\cdot\boldsymbol{V}) \qquad (12)
$$

where $\boldsymbol{\beta}_j = \boldsymbol{e}_j$ for $(j = 1, 2, 3)$ and $\boldsymbol{\beta}_j = \boldsymbol{e}_{j-3}$ for $(j = 4, 5, 6)$. $\boldsymbol{e}_j (j = 1, 2, 3)$ are the unit vectors of x, y, z axes. The second term of right hand side in eq.(12) indicates the dynamical restoring force due to the unsteady motion within the steady flow field.

Substituting the incident-wave velocity potential and scattered potential into the unsteady potential ϕ in eq.(12), the wave exciting force E_j acting in j-th direction is given by

$$
\frac{E_j}{\rho g A} = i\frac{\tau}{\nu}\iint_{S_H}\left(1 + \frac{1}{iK_0\tau}\boldsymbol{V}\cdot\nabla\right)(\phi_0 + \phi_j)\, n_j\, dS \quad (j = 1 \sim 6) \qquad (13)
$$

where $\nu = U\omega_0/g$. Considering the radiation potential $\phi_j (j = 1 \sim 6)$ as ϕ in eq.(12), the added mass and damping coefficients A_{ij}, B_{ij} acting in the i-th direction due to the j-th motion are computed by

$$
\begin{aligned}
-\frac{A_{ij}}{\rho} + i\frac{B_{ij}}{\rho\omega_e} &= \iint_{S_H}\left(1 + \frac{1}{iK_0\tau}\boldsymbol{V}\cdot\nabla\right)\phi_j\, n_i\, dS \\
&\quad - \frac{1}{2(K_0\tau)^2}\iint_{S_H}(\boldsymbol{\beta}_j\cdot\nabla)(\boldsymbol{V}\cdot\boldsymbol{V})\, n_i\, dS \qquad (14)
\end{aligned}
$$

The ship motions ξ_j can be determined by solving a simultaneous equation of the form

$$
\sum_{j=1}^{6}[-\omega_e^2(M_{ij} + A_{ij}) + i\omega_e B_{ij} + C_{ij}]\xi_j = E_i \quad (i = 1 \sim 6) \qquad (15)
$$

Here M_{ij} is the mass matrix associated with the body mass, and C_{ij} is the matrix of restoring forces. The details are shown in the text written by *Newman (1977)*.

The diffraction wave $\Re[\zeta_7 e^{i\omega_e t}]$ is calculated by

$$
\zeta_7 = \frac{-i\tau/\nu}{1 + \dfrac{1}{K_0}\nabla\Phi\cdot\nabla\dfrac{\partial\Phi}{\partial z}}\left(1 + \frac{1}{iK_0\tau}\nabla\Phi\cdot\nabla\right)\phi_j \quad \text{on } z = \zeta_s \qquad (16)
$$

The influence of the steady flow is introduced through the terms multiplied by $1/K_0$.

3 Numerical method

The RPM applied in this study is a desingularized panel method developed by *Jensen et al.(1986)* and extended to the unsteady problem by *Bertram (1990)*.

The steady and unsteady potentials, Φ and ϕ_j, are both expressed by the source distributions on the body surface S_H and the free surface S_F,

$$
\left.\begin{matrix}\phi_s(P) \\ \phi_j(P)\end{matrix}\right\} = -\iint_{S_H+S_F}\left\{\begin{matrix}\sigma_s(Q) \\ \sigma_j(Q)\end{matrix}\right\} G(P, Q)\, dS \qquad (17)
$$

where $G(P, Q) = 1/4\pi\sqrt{(x - x')^2 + (y - y')^2 + (z - z')^2}$. The body surface and the free surface are discretized into a finite number of constant panels, and the source panels on S_F are shifted one panel above the free surface to make the method desingularized. Numerical solutions for steady and unsteady problems are obtained so that a corresponding set of the free surface condition and the body boundary condition is satisfied at collocation points. The collocation points on S_H coincide with the geometric center of each panel and those on S_F are shifted one panel upward in order to force the radiation condition numerically. This numerical radiation condition is valid only when waves do not propagate to the forward direction of the ship, that is, $\tau < 0.5$ from a practical point of view (*Iwashita et al.(1993,1994)*).

4 Results

At first the present method is applied to a Wigley model for the validation, and some of the results are shown in Figs.2 $\sim$ 5. Fig.3 shows a good convergence of the numerical solution and Fig.4 shows that the present RPM is applicable only for $\tau > 0.5$. We can see in Fig.5 a significant influence of the steady nonlinear wave field.

Numerical computations are carried out also for a Series-60 ($C_b = 0.8$) model. It is confirmed in Fig.8 that the steady wave field can be predicted in quite good accuracy by the present method. On the other hand, pretty large discrepancies are still observed in Fig.9 between computations and experiments presented by *Ohkusu & Wen (1996)*. At ordinate 9 the computed result underestimates the experiment about 50 % in magnitude and this result is consistent with the result that we have obtained for the wave pressure, *Iwashita et al. (1993, 1994)*.

5 Conclusions

(1) The present RPM based on the desingularized method is confirmed to be effective to solve the unsteady problem taking account ot the nonlinear steady wave field.

(2) Consideration of the nonlinear steady wave field improves the estimation accuracy of diffraction wave qualitatively. However the improvement is not so remarkable at the bow part.

(3) The present method underestimates the diffraction wave about 50 % in amplitude. This is consistent with numerical and experimental results on wave pressure reported by *Iwashita & Ito(1998)*.

Acknowledgments

This work was sponsored by Fundamental Research Developing Association for Shipbuilding and Offshore, and by Grant-in-Aid for Encouragement of Young Scientists, Grant-in-Aid for Scientific Research (B) from Ministry of Education, Science, Sports and Culture of Japan.

References

BERTRAM, V. (1990), *Fulfilling Open-Boundary and Radiation Condition in Free-Surface Problems Using Rankine Sources*, Ship Technology Research, Vol. 37/2

IWASHITA, H., BERTRAM, V. (1997), *Numerical Study on the Influence of the Steady Flow in Seakeeping*, 12th WWWFB, Marseille

IWASHITA, H., ITO, A., OKADA, T., OHKUSU, M., TAKAKI, M., MIZOGUCHI, S. (1993), *Wave Forces Acting on a Blunt Ship with Forward Speed in Oblique Sea (2nd Report)*, J. Soc. Naval Arch. Japan, Vol. 173 (in Japanese)

IWASHITA, H., ITO, A., OKADA, T., OHKUSU, M., TAKAKI, M., MIZOGUCHI, S. (1994), *Wave Forces Acting on a Blunt Ship with Forward Speed in Oblique Sea (3rd Report)*, J. Soc. Naval Arch. Japan, Vol. 176 (in Japanese)

IWASHITA, H. (1998A), *Influence of the Steady Flow in Seakeeping of a Blunt Ship through the Free-Surface Condition*, 13th WWWFB, The Netherlands

IWASHITA, H., ITO A. (1998B), *Seakeeping Computations of a Blunt Ship Capturing the Influence of the Steady Flow*, Ship Technology Research, Vol. 45/4

JENSEN, G., MI, Z.-X., SÖDING, H. (1986), *Rankine Source Methods for Numerical Solutions of the Steady Wave Resistance Problem*, 16th Symp. on Nav. Hydrodyn., Berkeley

JOURNÉE J. M. J. (1992), *Experiments and Calculations on four Wigley Hullforms*, Faculty of Mechanical Engineering and Marine Technology, Ship Hydrodynamic Lab., Delft University of Technology

NEWMAN, J. N. (1978), *The Theory of Ship Motions*, Advances in Applied Mechanics 18

NEWMAN, J. N. (1977), *Marine Hydrodynamics*, The MIT press

OHKUSU, M., WEN, G. C. (1996), *Radiation and Diffraction Waves of a Ship at Forward Speed*, Proc. 21st Symp. Naval Hydro. , Trondheim

TIMMAN, R., NEWMAN, J.N. (1962), *The Coupled Damping Coefficients of a Symmetric ship*, JSR 5/4

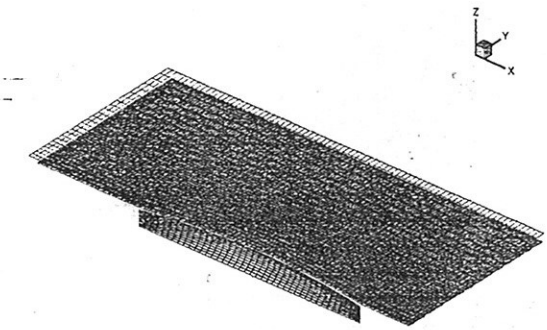

Fig.2 Computation grid of a Wigley model (400 and 1360 panels for S_H and S_F)

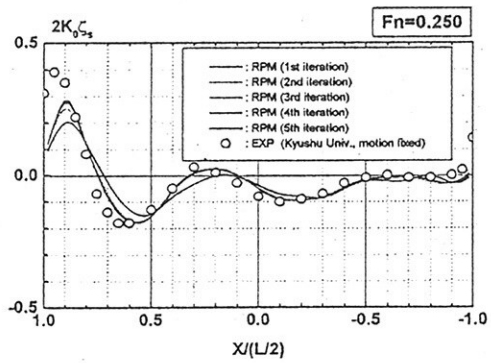

Fig.3 Steady wave along ship-side at $F_n = 0.25$

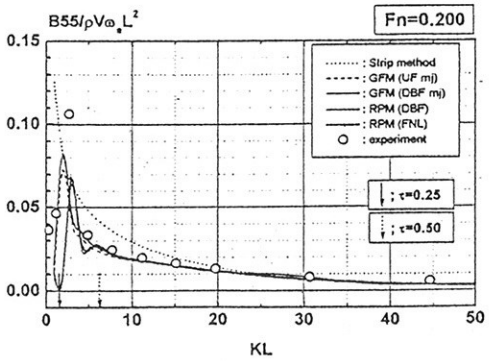

Fig.4 Damping coefficient B_{55} at $F_n = 0.2$

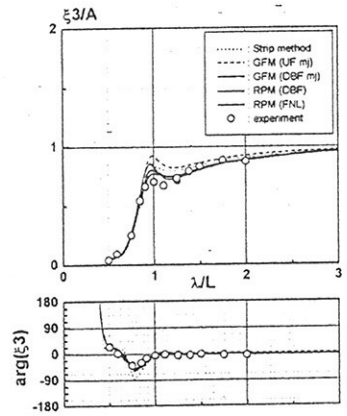

Fig.5 Heave motion at $F_n = 0.2$, $\chi = 180$degs.

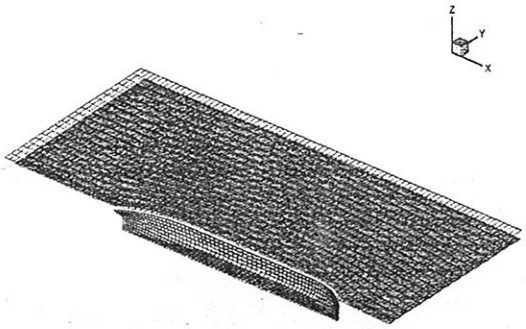

Fig.6 Computation grid of a Series-60($C_b = 0.8$)
(650 and 2125 panels for S_H and S_F)

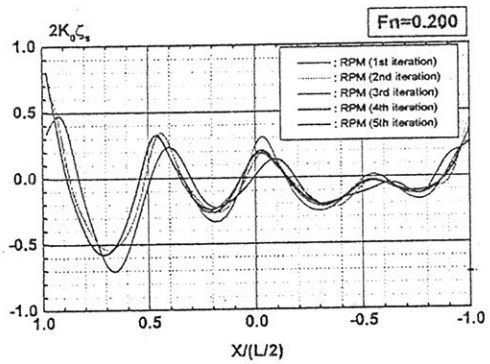

Fig.7 Steady wave along ship-side at $F_n = 0.2$

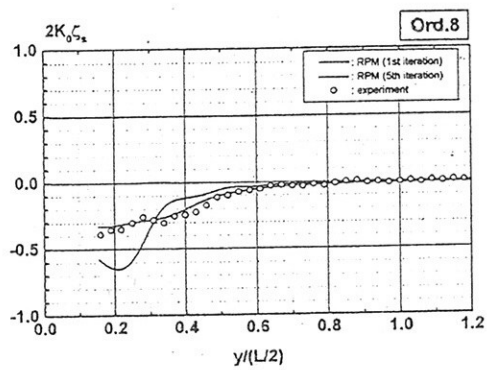

Fig.8 Steady wave along transverse axis at $F_n = 0.2$

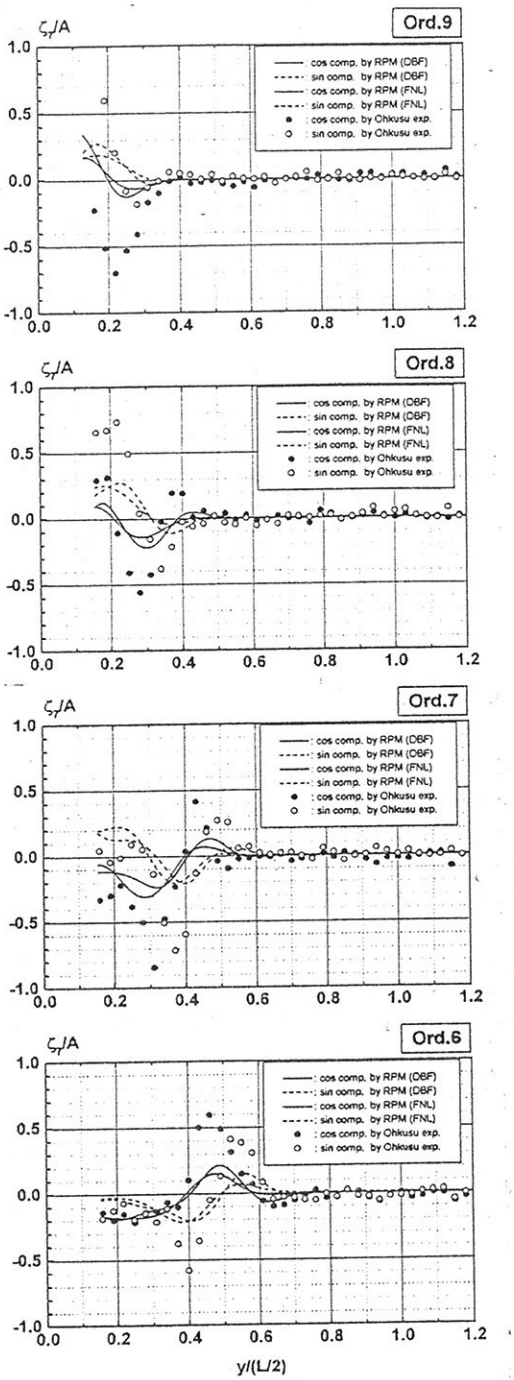

Fig.9 Diffraction waves of Series-60 along transverse axes
at $F_n = 0.2$, $\lambda/L = 0.5$, $\chi = 180$ degs.

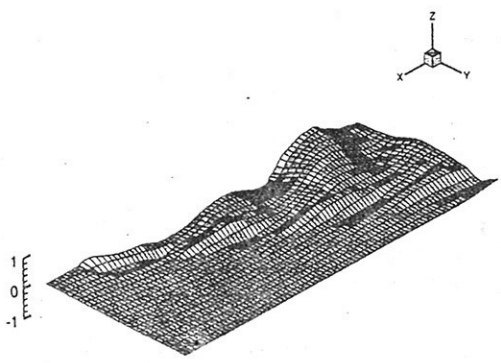

Fig.10 Diffraction wave around a ship
at $F_n = 0.2$, $\lambda/L = 0.5$, $\chi = 180$ degs. and $t = 0$

Domain Decomposition in Steady, Viscous-Flow Computations

Eric van der Maarel
MARIN, Netherlands
(H.T.M.v.d.Maarel@marin.nl)

1 Introduction

Application of tools from Computational Fluid Dynamics(CFD) in ship hydrodynamics is becoming common practice more and more. A natural consequence is the advent of requests for the application of CFD tools in the analysis of flow around more and more complex geometries. For viscous-flow numerical computations this introduces the need for more advanced ways to handle geometry-related matters in CFD methods.

Traditionally, for viscous-flow computations in 3-dimensional space, a discretisation of the fluid domain, is obtained through the generation of a 'structured' grid, consisting of hexahedral elements, along the structure (e.g., the hull of a ship). A necessary property of this grid is the application of a strong stretching (or rather compression) at appropriate places in order to have sufficient resolution in the boundary layer. Such a stretching needs to be even stronger when the fluid-flow system uses a turbulence model without the application of the law-of-the-wall and going to real ship Reynolds numbers.

Tightly associated with this approach is the notion of the 'quality' of the grid generated. The definition of the quality of a grid is strongly dependent on the properties of the fluid-flow code, for which such a grid has been generated in the first place. In general, it is related to the condition of the system of equations set up in the fluid-flow program and to the robustness of the method used to solve this set of algebraic equations.

Usually the grid quality degenerates for highly skewed grids larger deviations from orthogonality of the grid and perhaps cell aspect ratios. These aspects in grid generation are becoming more difficult to overcome with increasing complexity of the geometric shape. Usually for generally smoothly shaped forms generating a 'good quality' 3D grid is not too hard to do. Problems may arise for bluntly shaped bodies, such as e.g. the after body of typical tanker, and for geometries with strongly curved shapes, such as near the skegs at twin-skeg hull forms. Such problems are mainly related to the inability to create a grid of good quality around the geometry. Thus, one is often forced to use a grid of poor quality, with and is faced with convergence problems and maybe results of locally insufficient resolution

The situation as drawn above is typical for a system where the grid around the geometry is generated in a single-block structure. Here, enforcing a grid of sufficient quality is some part of the domain, in general may lead to insufficient quality in another area. This becomes more so in situation where the geometry itself is of a more complex nature.

One way to alleviate this situation is to subdivide the fluid-flow domain of interest into several parts and to arrange grids to be constructed in each subdomain (or block) almost independently from each other. Dependent on the amount of independence used, this requires the flow solver acting on the grid to be able to handle the various systems. For slightly independent grid generation the final system of grids of all subdomains may be reconstructed to a single block, without sacrificing the good properties of each block in the set of blocks. Another situation that is more likely to occur, is where the grids in the various blocks cannot be merged to give a single block grid, e.g., when grid lines across block interfaces do not match (in location and maybe in number as well), so-called non-conforming grids. Non-conforming grids can be used in a structure where the blocks have no overlap at all and still are fully covering the the domain. The most flexible situation however, is obtained when the

system is allowed to have overlapping blocks with non-conforming grids. Then, the only requirement that relates to interaction of the grids in the blocks, is that the system of grids has to fully cover the fluid domain of interest.

2 Domain Decomposition

For MARIN's RANS code for steady, viscous-flow computation around hull form structures, PARNASSOS [1], we have been working on embedding the basic solver in a multi-block domain-decomposition environment. The approach has an initial goal to be able to do fluid-flow computations, using the basic solver in its new environment of a (small) set of non-overlapping blocks, with initially a set of conforming grids.

PARNASSOS is intended to do steady state Navier-Stokes computations for a single-block domain. It has been extended to support more kinds of boundary conditions, and therefore can be used as the solver in each block of a set of blocks, resulting from a decomposition of the domain.

The crucial aspect in such a set-up is the mechanism in which the data for each block is coupled to the data in other blocks. For each block (subdomain) the boundary data is provided by either neighboring blocks (along block interfaces, interface boundaries) or by the problem's definition itself (along the boundary of the domain) If a neighboring block provides boundary conditions, in general these will depend on the local solution of the Navier-Stokes problem. This solution itself is obtained through the iteration process and dependent on the boundary conditions supplied for that domain, thus leading to boundary conditions that are not fixed on interface boundaries, during the iteration process which solves the (discretised) Navier-Stokes equations. For a fully implicit solver therefore, an iteration process to solve the fluid-flow problem for such a set of subdomains, consists of at least two levels. One is the inner level which aims at solving the (discretised) equations per block. This process itself is likely to consist of a number of nested iteration processes itself, but can be looked at as the single process which solves the a subproblem in a subdomain. The outer level iteration process aims at introducing the coupling between the solutions for the various blocks. It is implemented by exchanging data between blocks. Thus, in each iteration step on the outer level, the local subproblems in each block are redefined through a change in boundary conditions applied by communication of data between the blocks, providing each block with updated boundary conditions.

3 1D Analysis

From literature on domain-decomposition methods for elliptic equations, it is known that the convergence of the outer level iteration strongly depends on the data communicated between the blocks, or put differently, on the subsequent redefinitions of the subproblems. Given a 1-dimensional problem

$$Lu = f,$$

for $u = u(x)$ unknown and $f = f(x)$ given functions of the independent variable x in some domain $\Omega \subset \mathbb{R}$ and boundary conditions

$$Bu = g,$$

for g given and for $u(x)$ on $x \in \partial\Omega$, the boundary of Ω. Decomposition of Ω in two subdomains Ω_k, $k = 1, 2$, leads to a set of two subproblems denoted by

$$\begin{aligned} Lu_k &= f_k, \\ B_k u_k &= g_k, \end{aligned}$$

where the subscript $k = 1, 2$ indicates the kth subproblem and subdomain. In the boundary condition for this subproblem g_k may depend on the solution on the other neighboring domain. A well-known

method to define such a set of subproblems in each outer-level iteration makes $g_k^{(n)}$ for iteration n dependent on the approximate solution at iteration level $n-1$. Thus we can have

$$\begin{aligned} Lu_k^{(n)} &= f_k, \\ B_k u_k^{(n)} &= g_k^{(n)}, \end{aligned}$$

where

$$g_k^{(n)} = g(u_k^{(n-1)}).$$

At discretisation of the equations, e.g., with a finite volume or finite difference method on a uniform grid, the nodal values of approximate solutions can be indicated with $u_i^{(n)}$, for the first subdomain and $v_i^{(n)}$ for the second subdomain, both at iteration level n. With m cells per subdomain and l cells in the overlap, some general interface equations are given by

$$\begin{aligned} u_m^{(n)} + \alpha u_{m-1}^{(n)} &= v_l^{(n-1)} + \alpha v_{l-1}^{(n-1)}, \\ v_0^{(n)} + \beta v_1^{(n)} &= u_{m-l}^{(n-1)} + \beta u_{m-l+1}^{(n-1)}. \end{aligned}$$

A domain-decomposition method with interface equations as given above is called a Generalized Schwarz Alternating Method (GSAM) [2]. The convergence rate of the outer iteration is known to strongly depend on the choice of α and β. An example is given in Fig. 1 for the Poisson equation and standard five point finite-difference discretisation. This figure gives the convergence factor of the outer iteration as a function of $\alpha = \beta$ and overlap hl (with fixed mesh width $h = 0.1$).

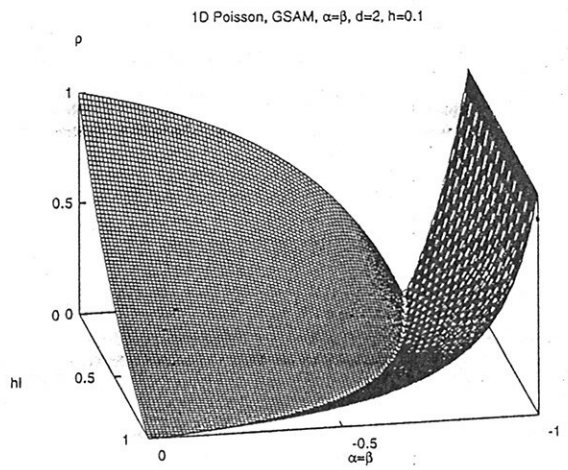

Figure 1: Convergence factor for Poisson equation with mesh width $h = 0.1$.

An analysis for the steady convection-diffusion equation reveals insight into the convergence behavior of the outer iteration process for fluid-flow problems. Since a convection-diffusion problem is not symmetric with regards to the convection direction, the parameters α and β can be chosen independently. Furthermore, the results will depend on the diffusion in the system, indicated by the cell-Péclet number Pe. For the second-order accurate, fully one sided generalized QUICK scheme for the convection (parameter $\lambda = -1/2$), central difference for the diffusion, two nodal points of overlap and $\alpha = \beta$, the asymptotic convergence rate as a function of cell-Péclet and parameters is shown in Fig. 2. Optimal convergence behavior is obtained for $\beta = 0$ at sufficiently large Pe. However, a serious degradation of convergence occurs for small Pe. In this region an optimal value for α may be applied. The optimum for α depends on Pe and the convergence factor ρ is quite sensitive to the value of α near its optimum.

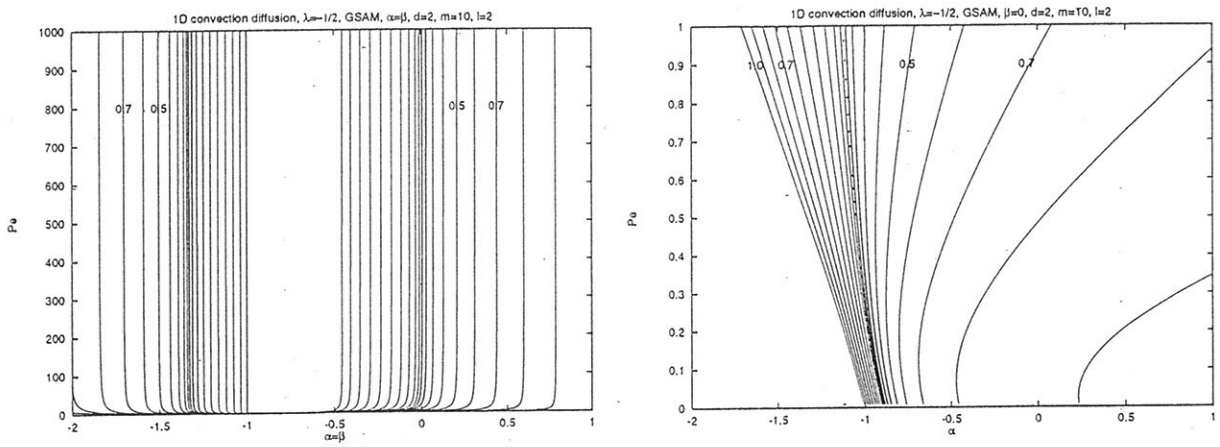

Figure 2: Iso lines of convergence factor $\rho \leq 1$ for GSAM with second-order generalized QUICK discretisation, $\lambda = -1/2$, with 2 subdomains, 2 cells overlap (minimum).

4 Results

Here we present some results for some actual computations with PARNASSOS and the domain-decomposition method for the turbulent flow along the stern of the Wigley hull at $\mathrm{Re} = 10^6$. The hexahedral grid consists of 65 nodes in the main flow direction, 51 in normal direction and 21 in girth-wise direction. The grid was split in normal direction at grid plane number 41 counted from the hull, giving a decomposition with two subdomains. The overlap is constructed by copying the required geometric data from the neighboring block, across the interface. The local cell-Péclet number based on the total viscosity, normal velocity and cell size in normal direction is in the order of 1. An impression of the topology and some convergence result are shown in Fig. 3. The convergence history shows maximum pressure difference over both blocks versus the number of blocklevel iteration, for the cases $\alpha = \beta = 0$ and $\beta = 0$, $\alpha = -0.4$, applied to all components of the velocity vector and the pressure.

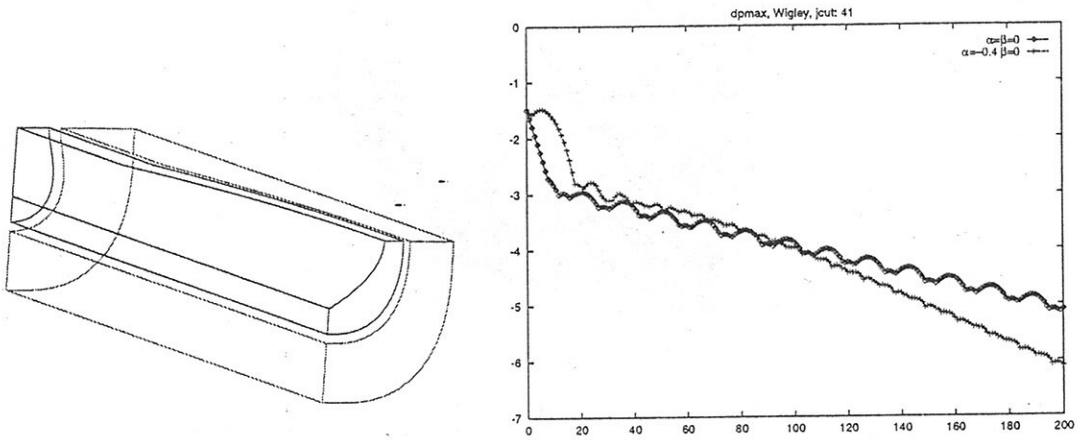

Figure 3: Topology and convergence for Wigley hull at $\mathrm{Re} = 10^6$.

References

[1] Hoekstra, M. and Eça, L., PARNASSOS: An efficient method for ship stern flow calculation. In proceedings of the *Third Osaka Colloquium*, Osaka, Japan, pp. 331–357, 1998.

[2] Tang, W.P., *Generalized Schwarz splittings*, SIAM J. Sci. Stat. Comput., 13, pp. 573–595, 1992.

Numerical simulation of viscous flow and free surface around ship using RANS solver Finflo

Jerzy Matusiak, Helsinki University of Technology, Ship Laboratory

1 Introduction

In 1995, the research project was started aiming at the development of method capable to solve the problem of viscous flow and free surface around ship. Reynolds-averaged Navier-Stokes (RANS) solver called FINFLO (Siikonen et al 1994, Siikonen 1996), developed at the Laboratories of Aerodynamics and Applied Thermodynamics of Helsinki University of Technology, was chosen as the platform of the method. The solution method of original FINFLO utilises a finite-volume formulation, employs structured multiblock grids and it is based on a compressible flow assumption. An upwind-type spatial discretization of third-order accuracy without the use of flux limiter and implicit time integration are applied. The pseudocompressibility feature was incorporated in the code in order to cope with the flows of liquids.

2 Ship flows with no free surface

2.1 Double-hull flow of HSVA tanker

First naval application of FINFLO was a computation of viscous flow of two versions of the so-called HSVA tanker (Mystery). The double hull model was used in this investigation and the results were compared to the model scale results obtained in wind tunnel and in towing tank. Several turbulence models were used. The best results in terms of flow pattern at stern were obtained using the Menter's k-ω turbulence model. Double-model resistance coefficient is given in Table 1.

Table 1 Double-model resistance coefficient of the HSVA-1 tanker. Comparison between the measured value of Cetena and the FINFLO computations (Saisto&Sundell 1996, Schweighoffer&Hellsten 1999)

	C_V*10^3	ΔC_V*10 [%]
Measured, Cetena $C_V = (1+k)\,C_F$	4.11	-
Computed, Menter's SST turbulence model	4.29	4.4
Computed, Menter's RCSST turbulence model	4.32	5.1
Computed, k–ε *turbulence model*	3.96	-3.7
Computed, Cebesi-Smith turbulence model	4.02	-2.2

The limiting streamlines obtained with two turbulence models are compared to the flow visualization results in Fig. 1.

1.2 Fully turbulent flow over a flat plate for a large range of Reynolds numbers

Schweighoffer (1997) has evaluated by Finflo the fully turbulent flow over a flat plate for a large range of Reynolds numbers. The results of this investigation in terms of frictional resistance coefficient are presented in Fig. 2. A clear difference of slope of ITTC-57 correlation line is noted. At large Reynolds numbers (ship scale); C_F of ITTC-57 correlation line is very close to the results of computations and ESD data. At Reynolds numbers corresponding to model scale, C_F of ITTC-57 correlation line is approximately 4 % higher than that of ESD data and 8% higher than the computed values.

3 Free surface hull flows

The wave surface η generated by ship hull is evaluated making use of the kinematic boundary condition

$$\frac{d\eta}{dt} = w = \frac{\partial \eta}{\partial t} + u\frac{\partial \eta}{\partial x} + v\frac{\partial \eta}{\partial y}, \tag{1}$$

where u, v and w are x-, y- and z-components of flow velocity. The bulk flow is computed with a dynamic pressure set to zero at the deformed free surface. At each iteration cycle of bulk flow evaluation, the free surface is evaluated using expression (1). This is done using a third order upwind finite difference scheme and explicit time integration. The deforming grid technique is used. In other words, at each iteration cycle the computational grid is adjusted according to the deformed free surface. An example of grid deformation is presented in Fig. 3.

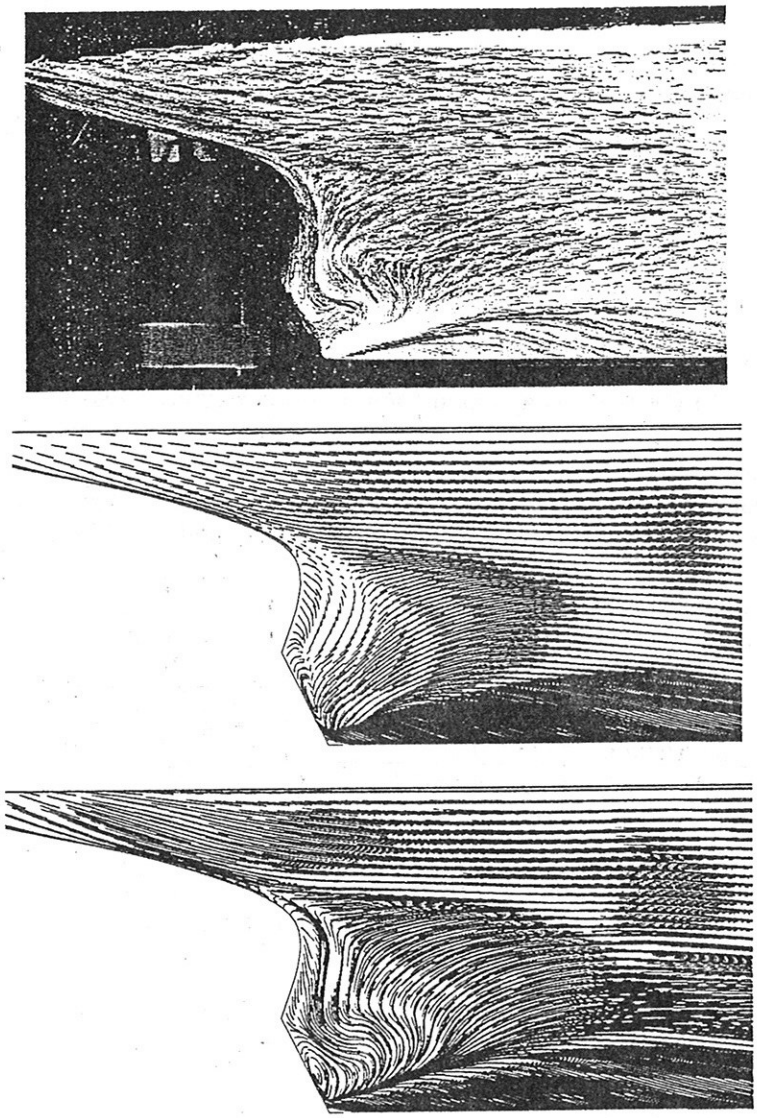

Fig. 1 HSVA-1 tanker. Experimental flow visualization results (top) compared to the limiting streamlines obtained by Finflo computations with k–ε (middle) and k-ω RCSST turbulence models (Schweighoffer&Hellsten 1999).

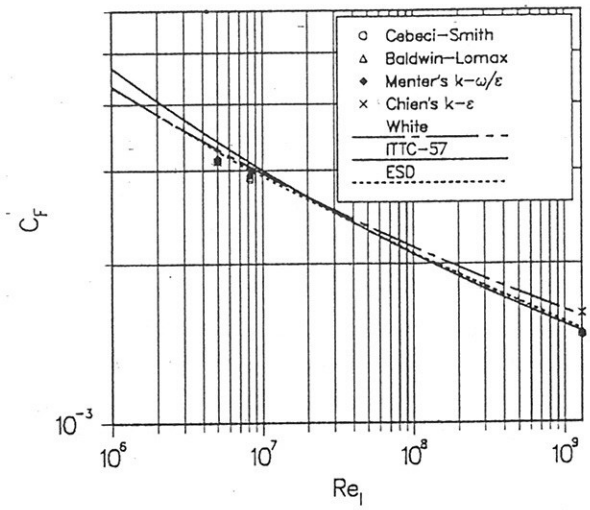

Fig. 2 Mean skin friction coefficient C_F, derived from Finf2d calculations for Cebeci-Smith, the Baldwin-Lomax, Menter's k-ω/ε (SST) and Chien's k–ε turbulence models. Comparison to the turbulent theory according to White, the ITTC-57 model-ship correlation line and semi-experimental Engineering Science Data, ESD (Schweighoffer 1997)

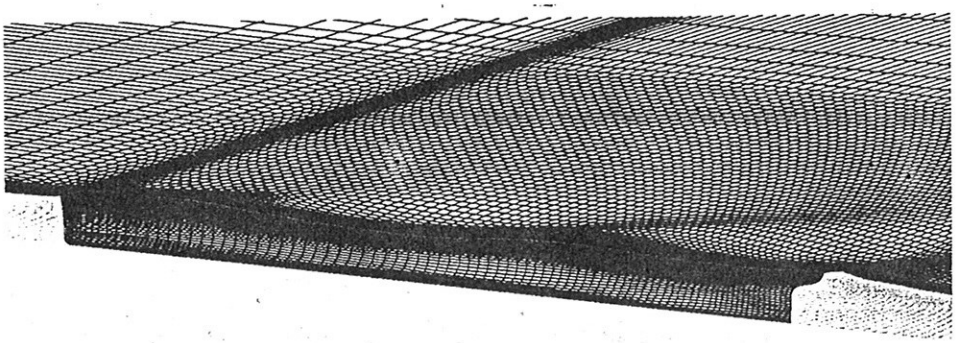

Fig. 3 Deformed grid of the Series 60 ship model.

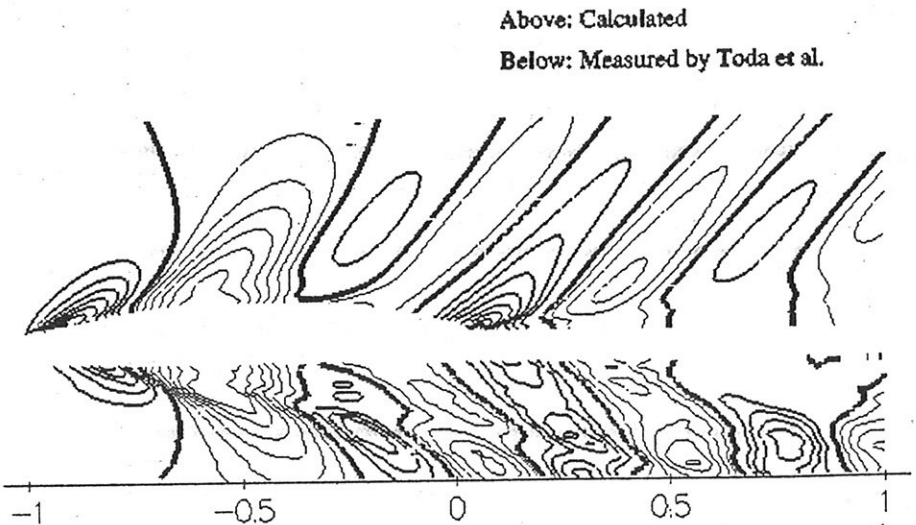

Fig. 4 Wave field of Series 60 C_B= 0.6 ship model. Fn = 0.316, Rn = 2.564•10^6 (Piippo 1998).

The contour plot (computed and measured) of the free surface near the Series 60 ship model is presented in Fig. 4. Other ship models, which were used in validating the method, were the Wigley model, the HSVA tanker and a model of containership known as Hamburger-case. In all cases, the error of computed total resistance was within the 10% when compared to the

measured values. Detailed flow survey was conducted and compared to the measured values for Series 60 case (Piippo 1998). The general trend of the computed results is to obtain wave field that is somewhat more regular and dampened when compared to the measured values. This discrepancy is more pronounced for low Froude numbers.
The deforming grid approach has proven to cope with rapid geometry changes such as caused by a transom stern. In Fig. 5 computed wave field generated by a model of containership Hamburger-case having a transom stern is presented.

4 Present and future work

Two features, important for modern fast vessels, are being developed. The first one is a treatment of a surface piercing bow bulb. The other one is an evaluation of ship dynamic trim and sinkage. The treatment of appendages and a simultaneous evaluation of hull a propulsor flows are being developed as well. Another topic of near future research is evaluating of hull flows at ship scale.

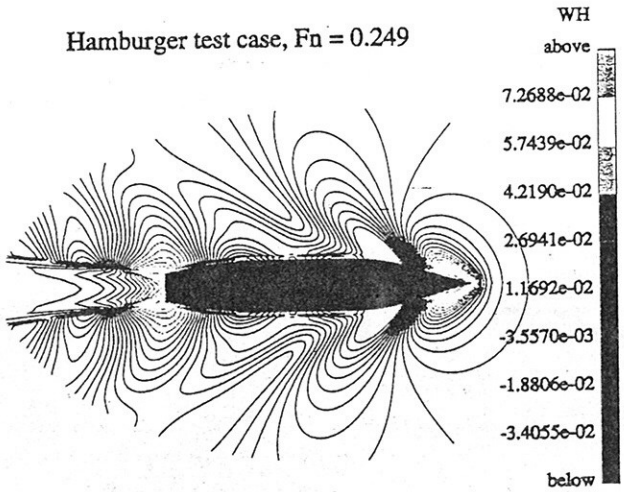

Fig. 5 Computed wave field of Hamburger-case. Rn = 13.2•10^6. Number of the iteration cycles at the first grid level = 14800. 818505 cells in O-O type grid.

5 References

Piippo, H. 1998 Computation of Steady Flow of Series 60 Ship Model. Helsinki University of Technology, Ship Laboratory, Master thesis.

Saisto, I. & Sundell, T. 1996 Computation of the viscous flow field around ship hulls. Symposium of Maritime Institute of Finland. VTT Symposium series, No 168, Integrated numerical and experimental methods in ship design, Technical Research Centre of Finland, Espoo 1996.

Schweighoffer, J. & Hellsten, A. 1999 Computations of the viscous flow field around the HSVA-1 tanker using two versions of the k-ω turbulence model. Helsinki University of Technology, Laboratory of Aerodynamics, Series B, Report B-51, Espoo 1996, Finland.

Schweighoffer, J. 1997 Evaluation of the fully turbulent flow over a flat plate for a large range of Reynolds numbers. Helsinki University of Technology, Ship Laboratory, Master thesis.

Siikonen, T. 1996 FINFLO User Guide, Version 2.2, Helsinki University of Technology, Laboratory of Applied Thermodynamics.

Siikonen, T. et al 1994 Transonic flow over a delta wing using a k-ε turbulence model. In Proceedings of the 19th ICAS Congress, pages 700-710, Anaheim, Sep 1994, ICAS Paper 94-2.3.4.

Comparison of Three Turbulence Models for the Study of the Wake Past a Ship Hull

Roberto Muscari, Riccardo Broglia & Andrea Di Mascio
INSEAN
Via di Vallerano, 139 - 00128 Roma - ITALY

1 INTRODUCTION

The flows to be computed in naval hydrodynamics are such that the only feasible simulations can be carried out by the Reynolds-averaged Navies-Stokes equations (RANSE). In fact, the Reynolds number is $O(10^6 \div 10^7)$ for towing tank tests, and $O(10^8 \div 10^9)$ for full-scale flows. Therefore, an important issue to be addressed is the choice of the turbulence model. Several choices are possible but none can be said to be the best solution for all cases. Given the complexity of the flow structure, the Reynolds stress models would be the most appropriate, but they have not yet been developed as much as the classical eddy viscosity models, and are rather expensive in terms of storage and CPU time. In practical applications, the most popular models are those based on the eddy viscosity concept. In order to have more information on the behaviour of these models, we have computed the flow past a model of the american combatant ship DDG51 (INSEAN Model 2340) for which extensive experimental data are available. We have considered three eddy viscosity models in our analysis: the algebraic model by Baldwin and Lomax (Baldwin [1978]), the one-equation model by Spalart and Allmaras (Spalart [1994]) and the $\kappa - \varepsilon$ model by Chang, Hsieh and Chen (Chang [1995]).

In section 2 we give a brief description of the mathematical model and the numerical integration technique, whereas the discussion on the results is in section 3. In the last section some conclusions are drawn.

2 MATHEMATICAL AND NUMERICAL MODELS

The incompressible turbulent flows past a rigid body in steady straight motion is described by the RANSE. When only the average steady state is to be computed, the pseudo-compressible formulation (Chorin [1967]) may be exploited. The use of this approach allows the straightforward extension of numerical integration techniques for compressible flows to the incompressible case. The governing equations are, in non-dimensional form:

$$\frac{\partial p}{\partial t} + \beta \frac{\partial u_i}{\partial x_i} = 0 \qquad ; \qquad \frac{\partial u_i}{\partial t} + \frac{\partial u_i u_j}{\partial x_j} + \frac{\partial p}{\partial x_i} - \frac{\partial \tau_{ij}}{\partial x_j} = 0 \qquad i = 1,2,3 \tag{1}$$

where x_i is the i-th coordinate, u_i is the i-th component of the velocity vector, β is the pseudo-compressibility factor, $\tau_{ij} = \mu_t \left(\frac{\partial u_i}{\partial x_j} + \frac{\partial u_j}{\partial x_i} \right)$ is the stress tensor, $\nu_t = \frac{1}{\mathsf{Re}} + \nu_{\mathsf{TURB}}$ is the global kinematic viscosity, Re is the Reynolds number and ν_{TURB} is the turbulent viscosity, calculated by means of one of the turbulence models cited in the Introduction. Finally $p = \frac{P}{\rho} + \frac{x_3}{\mathsf{Fr}^2}$, P being the pressure and Fr the Froude number.

The mathematical model has to be completed with initial and boundary conditions. On solid walls, no–slip condition is enforced, (i.e. $u_i = 0$ for $i = 1,2,3$), whereas no condition on the pressure is required. At the free surface, normal and tangential stresses must be enforced

$$p + \tau_{ij} n_j n_i = \frac{h}{\mathsf{Fr}^2} \qquad \tau_{ij} n_j t_i^l = 0 \tag{2}$$

where n_i is the i-th component of the normal unit vector and $t_i^l \quad l = 1,2$ are the i-th components of two unit tangent vectors, and where the stresses due to air and to surface tension are neglected. Moreover, the unknown free surface elevation $h = h(t, x_1, x_2)$ is determined by enforcing that the boundary is a material surface

$$\frac{\partial h}{\partial t} + u_1 \frac{\partial h}{\partial x_1} + u_2 \frac{\partial h}{\partial x_2} = u_3 \tag{3}$$

Numerical integration technique

For the numerical solution of the model (1), we have used a second-order accurate finite volume scheme; the convective fluxes were discretized by a ENO type scheme, whereas a centred scheme was used for the viscous terms. A multi-stage Runge-Kutta algorithm with local time stepping was applied to update the solution, and the convergence rate was improved by a Full Multigrid algorithm. The details of the numerical scheme can be found in (Di Mascio [1998]).

Turbulence models

The turbulence models considered in this work are all based on the eddy viscosity concept. The reader is referred to (Baldwin [1978]) for a description of the Baldwin and Lomax (BL) model, to (Spalart [1994]) for the Spalart and Allmaras (SA) model, and to (Chang [1995]) for the Chang, Hsieh and Chen (CHC) model. However, it is worth noting that SA and CHC are both strictly "local", in the sense that the coefficients in the equations depends only on quantities that can be computed from the velocity field and its first order tensor in each point, and from the distance from the nearest wall. This property is not shared by BL, for which the evaluation of the wall shear stress at the intersection of the "normal" to the wall is required. This aspect makes the use of BL rather difficult when dealing with complex geometries or unstructured grids.

3 RESULTS

The results shown in this section are obtained for the flow past the INSEAN Model 2340 (see fig. 1) whose length is 5.72 m . The flow is characterised by $\mathrm{Fr} = 0.28$ and $\mathrm{Re} = 1.2 \times 10^7$. The details of the experiments are given in (Olivieri [1999]), whereas for more comments and results the reader is referred to (Muscari [1999]). All the solutions were computed with a 5-block grid;

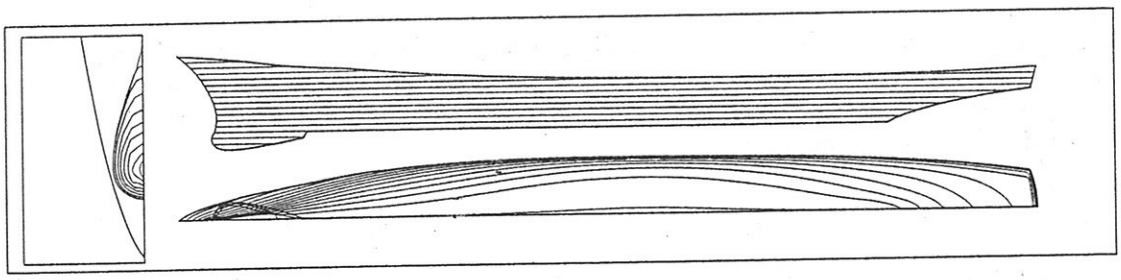

Figure 1: INSEAN 2340 (or DTMB 5415) combatant hull.

the total number of grid points is about 1'079'000 . The size of the cells near the wall was such that $y^+ \leq 1$ in the first grid point.

The general features of the flow are depicted in figures 3-2. Figure 3 shows the wave system generated by the hull. The area around the stern has been expanded to show the streamlines in the wake of the hull (figure 2). As can be noticed, a significant separation occur for this flow condition.

Let us now examine some numerical aspects of the simulations. As already pointed out, we use a multigrid technique to accelerate convergence, the finest grid being of about 1'079'000 points. On each grid, save the finest, 250 iterations are performed. Converged solution was reached, as can be seen for example in figure 4, where C_T, for all turbulence models, are plotted against iterations. For the second (coarse) and third (medium) grid, an ultimate value for the C_T is reached well before passing to the finer grid.

Finally, we present some results on the convergence properties of the scheme. In table 1 the convergence order p is computed through

$$p = \frac{1}{\ln 2} \ln \left[\frac{C_\mathrm{T}^{4h} - C_\mathrm{T}^{2h}}{C_\mathrm{T}^{2h} - C_\mathrm{T}^{h}} \right] \tag{4}$$

	Baldwin-Lomax			Spalart-Allmaras			Chang-Hsieh-Chen		
	C_V	C_P	C_{TOT}	C_V	C_P	C_{TOT}	C_V	C_P	C_{TOT}
Coarse	0.293	0.482	0.775	0.295	0.484	0.779	0.193	0.488	0.681
Medium	0.293	0.250	0.543	0.298	0.255	0.553	0.222	0.233	0.455
Fine	0.297	0.175	0.472	0.299	0.181	0.480	0.246	0.174	0.419
Extrapolated	—	0.139	0.441	0.300	0.145	0.445	0.361	0.156	0.412
Experimental			0.425			0.425			0.425
Conv. Order	-3.64	1.629	1.708	1.590	1.630	1.630	0.27	2.11	2.65
Uncer. %	—	25.9	7.0	0.2	24.8	7.9	31.8	11.5	1.7

Table 1: C_V, C_P, $C_T \times 10^2$ and convergence orders.

It can be seen that, probably a further refinement of the grid is required to reach the asymptotic range and hence the theoretical value $p = 2$. In the table can also be found the Richardson's extrapolation of the C_T, that is $C_T^R = \frac{2^p C_T^h - C_T^{2h}}{2^p - 1}$, where p is the computed convergence order. This value has to be compared with the experimental one $C_T^{EXP} = 4.25 \times 10^{-3}$. In this respect, the best prediction is given by the CHC model which approximates the experimental value within 3.1%, but BL and SA give also very good approximations. In the table is also reported the "uncertainty", i.e. the error on the finest grid with respect to the extrapolated value. It can be seen that, for the BL and SA, the pressure component is still far from grid convergence, while the viscous component is almost unaffected by grid refinements. For the CHC we have a lower C_P uncertainty, but a much higher C_V uncertainty. Because of the two components have opposite trends, the the C_T seems to have reached a fairly good grid convergence.

4 CONCLUSION

Three turbulence models are used for the study of the flow past a model of the american combatant ship DDG51 (INSEAN Model 2340). In terms of total drag coefficient, all models offer very good performance, with the experimental value approximated by less than 5%. The convergence analysis shows that the order of the scheme is near the theoretical one, despite some evident problems with the pressure calculation.

References

Baldwin B.S., Lomax H. (1978). "Thin-Layer Approximation and Algebraic Model for Separated Turbulent Flows", AIAA Paper 78-257.

Spalart P. R., Allmaras S. R. (1994). "A one–equation turbulence model for aerodynamic flows", La Recherche Aérospatiale, vol. 1, pag. 5.

Chang K. C., Hsieh W. D., Chen C. S. (1995). "A modified low-Reynolds-number turbulence model applicable to recirculating flow in pipe expansion", J. Fluids Eng., vol. 117, pag. 417.

Favini B., Broglia R., Di Mascio A. (1996). "Multigrid Acceleration of Second Order ENO Schemes from Low Subsonic to High Supersonic Flows", Int. J. Num. Meth. Fluids, vol. 23, pag. 589.

Chorin A. (1967). "A Num. Method for Solving Incomp. Viscous Flow Problems", J. Comp. Phys., vol. 2, pag. 12.

Muscari R., Broglia R., Di Mascio A. (1999). "Comparison of Three Turbulence Models for the Study of the Wake Past a Ship Hull", JAKOM '99, Fukuoka, Japan.

Olivieri A., Pistani F., Penna R. (*in preparation*) "Experimental investigation of the flow around a towed fast displacement ship hull model".

Di Mascio A., Broglia R., Favini B. (1998). "Numerical simulation of free–surface viscous flows by ENO-type schemes", ICHD '98, Seoul, Korea.

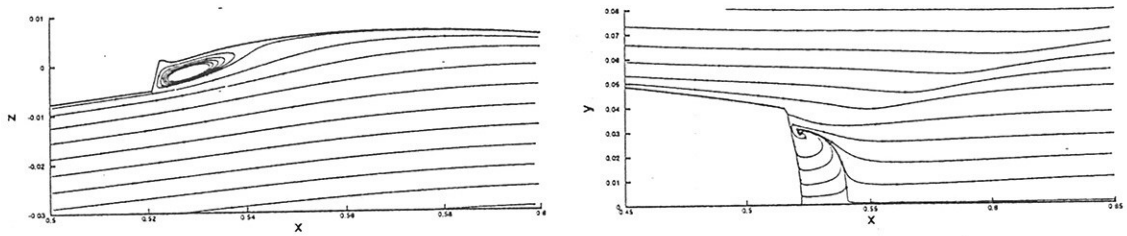

Figure 2: Streamlines in the $x_2 = 0$ (left) and the $x_3 = 0$ (right) planes.

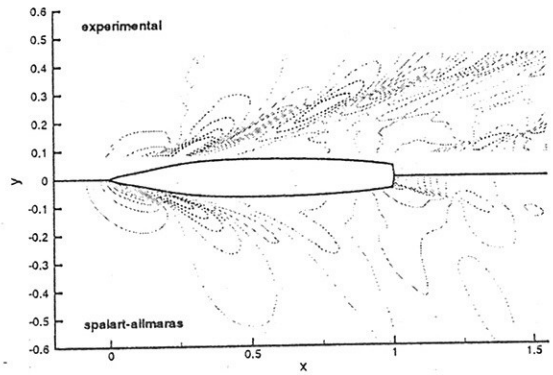

Figure 3: Wave system past the hull.

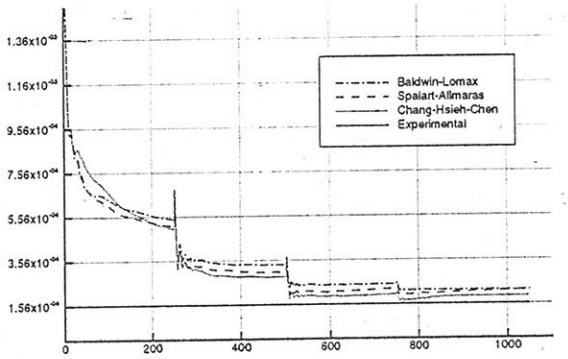

Figure 4: Total drag coefficients vs. iterations.

Stabilisation and Simulation of Non-Linear Free-Surface Flows using High Order Algorithms

Iain Robertson and Spencer Sherwin
Department of Aeronautics,
Imperial College of Science Technology and Medicine,
Prince Consort Road, South Kensington, London, SW7 2BY

1 Introduction

Numerical techniques have been widely adopted to solve non-linear free-surface motion around submerged and surface piercing complex structures. The finite element technique, in particular, has been found to be very efficient in the solution of free-surface problems. To simulate the flow we use a high order hp/Spectral finite element code, $\mathcal{N}\varepsilon\kappa\mathcal{T}\alpha r$, [1]. The hp/Spectral technique is capable of very rapid convergence rates, typically $\epsilon \propto h^p$ where h is the mesh size and p the polynomial order, which coupled with the ability to handle complex geometries make it a very powerful tool to aid the simulation of gravity waves.
A common problem with many discretisation techniques is the use of a smoothing technique to inhibit the formation of the free-surface saw-tooth pattern, which indicates an unstable system. This inherent instability is characteristic of linear and non-linear flow. In this paper we formulate a semi-discrete solution system to examine the spatial discretisation effects on the stability of linear gravity waves and recognise methods to counter these instabilities. These methods are then applied to the solution of non-linear motion.

2 Inviscid Free-Surface Governing Equations

We consider a Cartesian coordinate system, where the free-surface is described by $z = 0$, where z points vertically upwards and the free-surface height can be represented as $z = \zeta(x, t)$. The flow field is evaluated by solving the the Laplacian

$$\nabla^2\phi = 0 \tag{1}$$

where $\mathbf{u} = \nabla\phi$ and $\nabla.\mathbf{u} = 0$. The linearised dynamic boundary condition is formulated from the Eulerian momentum equation with all second or higher terms removed and the kinematic boundary condition ensures that there is no fluid flow through the free-surface. The linearised dynamic and kinematic conditions are therefore,

$$\frac{\partial\phi}{\partial t} = -g\zeta\,, \tag{2}$$

$$\frac{\partial\phi}{\partial z} = \frac{\partial z}{\partial t}, \tag{3}$$

evaluated on $z = 0$.

3 Stability Analysis of Spatial Discretisation

We start our analysis by considering two basic mesh configurations. The first is a structured, symmetric mesh and the second a structured, asymmetric mesh both shown in figure 1. We compare the meshes in order to investigate the effects of different spatial discretisations on the stability of the computations. Using the hp/spectral element solver $\mathcal{N}\varepsilon\kappa\mathcal{T}\alpha r$ to compute linear flow, the two meshes gave differing results for long time studies. The symmetric mesh was stable over long periods of time, whilst the asymmetric quickly displayed the familiar saw-tooth pattern. For an initial free-surface disturbance of $\zeta = 0.1\cos(\pi(x + 0.5))$ the profiles of the free-surface for the respective grids can be seen in figure 1. This instability was largely irrespective of the time discretisation scheme or length of time-step used. Therefore the temporal discretisation was not affecting the stability of the solution.

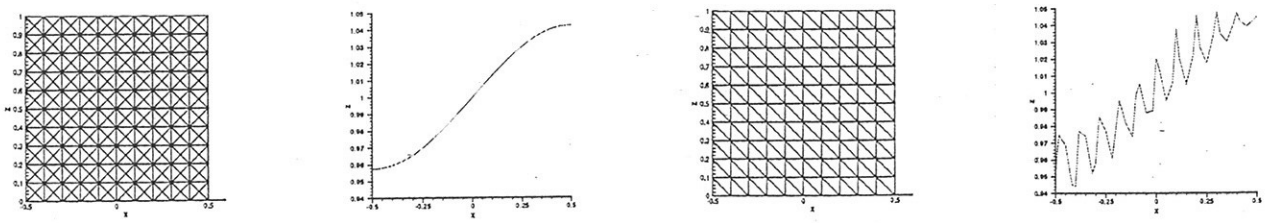

Figure 1: Symmetric and asymmetric mesh for stability analysis and their corresponding free-surface profiles at T = 1.4

3.1 Formulation of Semi-discrete Eigenvalue Stability Analysis

In order to investigate the stability of the numerical problem we formulate a semi-discrete system by decomposing the Laplacian, $\mathbf{L}$, into its interior and free-surface boundary components, i.e.

$$(\nabla v, \nabla \phi) = \mathrm{L}\phi = \begin{bmatrix} \mathrm{L}_{ii} & \mathrm{L}_{ib} \\ \mathrm{L}_{bi} & \mathrm{L}_{bb} \end{bmatrix} \begin{bmatrix} \phi_i \\ \phi_b \end{bmatrix} = 0 \ , \tag{4}$$

where the subscript i refers to the interior of the domain and b the free-surface boundary. The first row of this system can be rearranged to obtain

$$\mathrm{L}_{ii}\phi_i + \mathrm{L}_{ib}\phi_b = 0 \Rightarrow \phi_i = -\mathrm{L}_{ii}^{-1}\mathrm{L}_{ib}\phi_b \ , \tag{5}$$

which expresses the interior degrees of freedom in terms of the free-surface boundary degrees of freedom. The differential of ϕ in the z direction can similarly be represented by an operator $\mathbf{D}$ such that

$$\frac{\partial \phi}{\partial z} = \mathrm{D}\phi = \begin{bmatrix} \mathrm{D}_{ii} & \mathrm{D}_{ib} \\ \mathrm{D}_{bi} & \mathrm{D}_{bb} \end{bmatrix} \begin{bmatrix} \phi_i \\ \phi_b \end{bmatrix} \ . \tag{6}$$

Following the above method we find an expression for the differential on the boundary to be

$$\left.\frac{\partial \phi}{\partial z}\right|_b = \mathrm{D}_{bi}\phi_i + \mathrm{D}_{bb}\phi_b \ . \tag{7}$$

Substituting (5) into (7) we find a relationship for the differential in terms of the boundary values of the velocity potential, i.e.

$$\left.\frac{\partial \phi}{\partial z}\right|_b = -\mathrm{D}_{bi}\mathrm{L}_{ii}^{-1}\mathrm{L}_{ib}\phi_b + \mathrm{D}_{bb}\phi_b \tag{8}$$

$$= \left[\mathrm{D}_{bb} - \mathrm{D}_{ib}\mathrm{L}_{ii}^{-1}\mathrm{L}_{ib}\right]\phi_b = \mathrm{N}_\mathrm{D}\phi_b \ , \tag{9}$$

where N_D can be thought of as a discrete Dirichlet-Neumann operator. By combining (9) with the linear free-surface boundary conditions we can now form the semi-discrete form of the linear free-surface motion

$$\begin{bmatrix} \phi_b \\ \zeta \end{bmatrix}_t = \begin{bmatrix} 0 & -\mathrm{gI} \\ \mathrm{N_D} & 0 \end{bmatrix} \begin{bmatrix} \phi_b \\ \zeta \end{bmatrix} \ . \tag{10}$$

The eigenvalues of the operating matrix dictate the stability of the scheme, if they have a positive real value the system is unstable.

3.2 Spatial Discretisation Comparison

We used the spatial discretisation analysis to compare the eigenvalues of the 10×10 symmetric and asymmetric meshes. The analysis was undertaken with $p = 3$ and the corresponding eigenvalues can be seen in figure 2 . As is clearly shown the asymmetric spatial discretisation causes an unstable solution. Further investigation on different meshes, figure 4, indicates that the instabilities are due to symmetry being lost locally, i.e. when a horizontally asymmetric element is included in the domain.

3.3 Mechanisms for Stability

3.3.1 Removal of high modes

We follow a procedure advanced by Moore [2], who theorised that the incorrect phase relation of the discretised system means that high frequency modes can have the same phase speed as low frequency modes permitting the system to resonant. To remove the instability he removed the higher modes and using the *hp* technique we can apply a similar technique. Figure 3 shows the resulting purely imaginary eigenvalues for computations using polynomial order 2 with the removal of the highest mode.

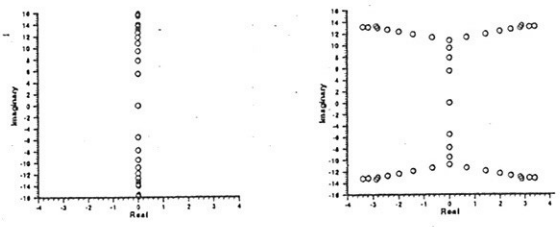

Figure 2: Eigenvalues for symmetric (left) and asymmetric 10×10 meshes

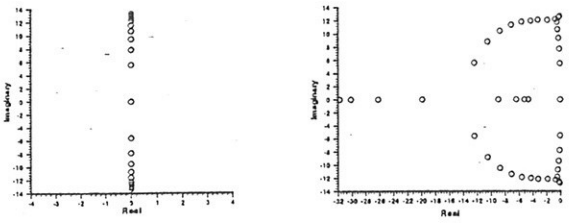

Figure 3: Eigenvalues for asymmetric mesh with removal of highest mode (left) and addition of diffusive term respectively

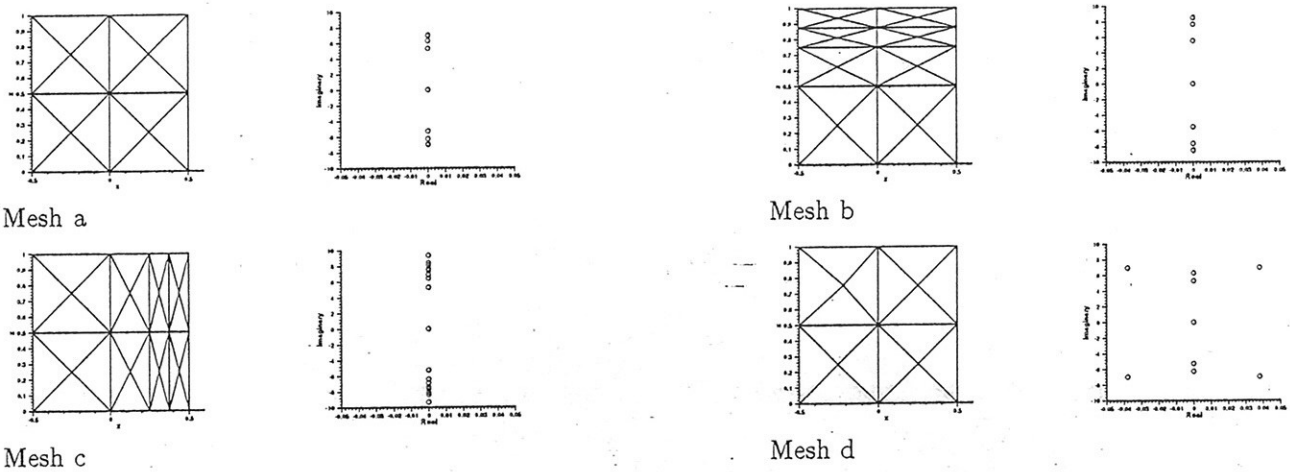

Mesh a

Mesh b

Mesh c

Mesh d

Figure 4: Comparison of eigenvalues of spatially semi-discrete system for contrasting meshes

3.3.2 Addition of a diffusive term

Artificial diffusion is commonly used in compressible flow simulation to remove numerical instabilities and is attractive in finite element methods due to the ease with which it can be implemented. To this end we consider adding a diffusive term to the kinematic boundary condition to try to enforce stability. The kinematic boundary condition then becomes

$$\frac{\partial \zeta}{\partial t} = \frac{\partial \phi}{\partial z} + \mu \frac{\partial^2 \zeta}{\partial x^2}, \tag{11}$$

where μ is some constant large enough to ensure stability. μ must be dependent on h and p to ensure convergence, therefore we choose $\mu = C\sigma^{\alpha p}$, where C and α are constants and σ is proportional to the asymmetry of the spatial discretisation [5]. The resulting eigenvalues can be seen in figure 3. As a result of the large mode removal needed to ensure a stable solution, typically half the modes, we choose to implement the added diffusive term method in our calculations.

4 Results

To test the added diffusive term method we ran a simple sloshing test case, consisting of a 10×10 asymmetric mesh with the free-surface having an initial displacement described by $\zeta = 0.1\cos(\pi(x+0.5))$. The profile of the free-surface after T = 1.14s is shown in figure 5, the saw-tooth pattern in figure 1 has been replaced by a smooth solution. Figure 5 compares the time history of a point on the free-surface undergoing maximum displacement for varying p and μ. It can be seen that as p increases μ decreases, thereby increasing the accuracy of the solution. The diffusive term method was incorporated into a non-linear free-surface code in the same manner as for the linear case. Correlation is sought by investigating wave motion contained within a box which is undergoing forced sinusoidal translational motion described by $d = a\cos\omega t$ where d is the displacement, $a = 0.002$ and ω is close to the natural frequency of the motion, ω_0. The results can be seen in figure 6. Agreement between the computational solution and a linear analytical approximation [3, 4] is very good especially close to start up, though as the amplitude grows non-linear characteristics of higher peaks and troughs are captured by the computational results, but neglected by the linear analysis. The computational code was then expanded to three dimensions, using domains including complex surface piercing geometries. Figure 7 shows waves travelling from right to left and interacting with a surface piercing circular cylinder.

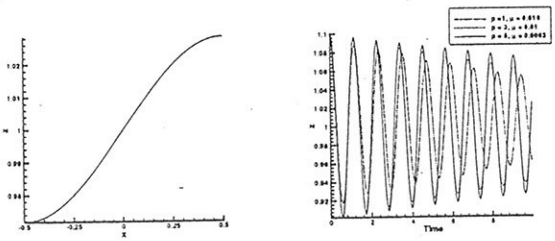

Figure 5: Free-surface profile at T = 1.14 with $p = 3$ and $\mu = 0.01$ and time history of free-surface

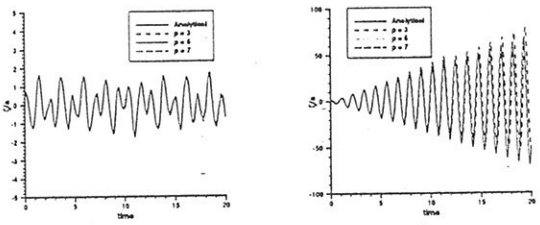

Figure 6: $\omega = 0.5414\omega_0$ and $\omega = 0.9999\omega_0$

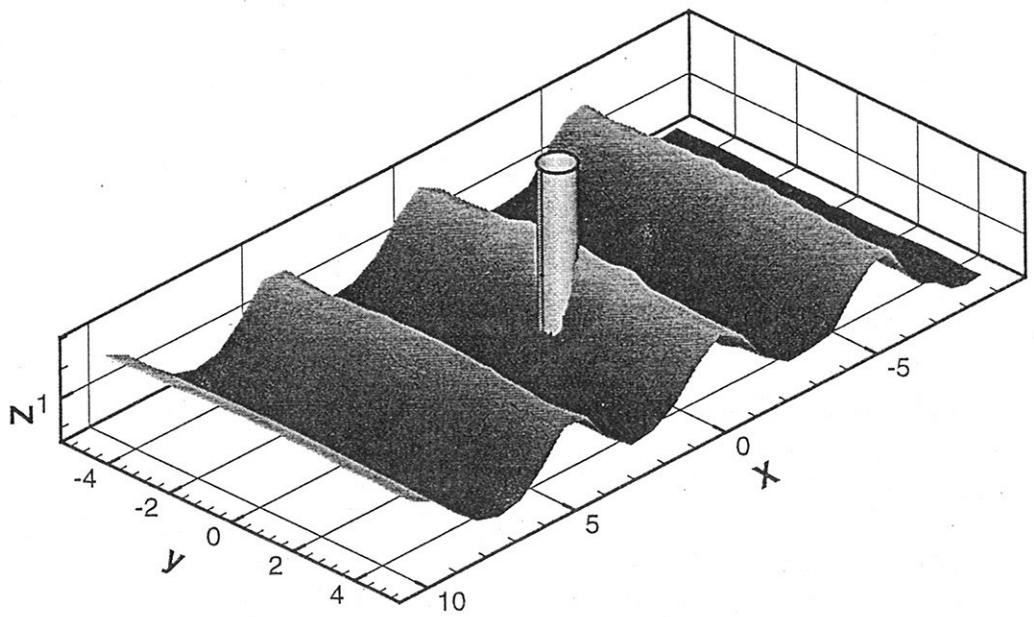

Figure 7: Waves from a wave-maker encountering a surface piercing circular cylinder

5 Future Work

Immediate future work includes validating the 3D code and developing a parallel version of the code. Furthermore, we are looking into the possibility of decoupling the free-surface with the interior domain. We would then use the Navier-Stokes equations to evaluate the interior, whilst having a non-linear free-surface.

References

[1] GE Karniadakis and SJ Sherwin. *Spectral/hp Element Methods for CFD.* Oxford University Press, 1997.

[2] DW Moore. Resonances introduced by discretization. *IMA J. Appl. Math.*, 31:1–11, 1983.

[3] OM Faltinsen. A numerical non-linear method of sloshing in tanks with two dimensional flow. *Journal of Ship Research*, 18(4):224–241, 1978.

[4] GX Wu, QW Ma, and R Eatock Taylor. Numerical simulation of sloshing waves in a 3d tank based on a finite element method. *Awaiting publication*, 1998.

[5] I Robertson and S Sherwin. Free-surface flow simulation using *hp*/spectral finite elements. *Awaiting publication*, 1999.

"Documented Solutions"
The ONR Computational Ship Hydrodynamics Validation Project

Edwin P. Rood
Office of Naval Research

RoodE@onr.navy.mil
703-696-4305
FAX: 703-696-2558

Naval needs require high resolution predictions of the turbulent free surface flow around surface ships. Traditional approaches employ towing tank measurements and correlation, based on previous experience, to obtain the expected full scale flow. The emergence of computational methods suggests the use of a numerical complement to the traditional towing tank approach. The numerical complement would permit rapid exploration of design space around a validated design point, and potentially permit the scale up of model data to full scale. Descriptions of various computational methods, including potential flow and viscous flow approaches, have been presented previously (Rood, et al., 1996a). It is argued in that paper that the required prediction variables necessitate including viscous effects in the governing equations. Hence predictions are sought using Reynolds-Averaged Navier-Stokes (RANS) equations applied to the flow. The equations are discretized, and solutions are obtained on massively parallel supercomputers. Today, very complex flows are routinely computed and displayed with inspiring effect in terms of visual presentations of contours of pressures and velocities. Notwithstanding the attractiveness of the appearance of many solutions, there is widespread recognition of the need for validation of the computational predictions. Although the idea of producing validated predictions is readily accepted, the actual implementation of this costly process is not so easily embarked upon.

It is very important that the RANS code developer understand the process for having RANS software accepted by the user community in a meaningful manner. Users are very skeptical of the claims of RANS methods, and proper conditioning of the software as it is matured can pave the way for easier acceptance of the product. In particular, users want to be assured that the software is credible and that turnaround can be achieved in a reasonable period. Users would like to see this information displayed in a rigorous manner.

Several years ago, the Office of Naval Research (ONR) embarked upon the development of a paradigm for the methodical validation of RANS computational methods (Rood, 1996b). That paper describes a strategy for implementing a process to arrive at validated software ready for use by the ship designer. The ONR strategy employed a surface combatant geometry (DTMB Model 5415 Surface Combatant) for the purposes of validating computational ship hydrodynamics. The implemented strategy consists of five parts: downselection of software, dissemination of software and documentation, aggressive application, complementary computational ship hydrodynamics and towing tank investigations, and scaling. ONR has been implementing that strategy with increasing intensity over the past several years. That particular project will come to a close for steady straight ahead conditions within the next two years, as it moves toward validating unsteady RANS predictions for motion caused by waves and for roll motion.

The emergence of computational RANS methods received a push forward when the Departement of Defense in 1997 awarded a Challenge Project supercomputer time grant for "Time-Dependent Computational Ship Hydrodynamics". This project is one of only 19 awarded by the

High Performance Computing Modernization Office, and is meritorious in its objective of predicting the time dependent hydrodynamic flow around a turning surface combatant, the US Navy DDG-51 destroyer. Progress in performing this computation is extraordinary, and is described by Rood (1997, 1998a, 1998b, 1999). The computations are complex because of the need to properly determine the large free surface deformations for the combatant, and because of the transom stern geometry producing a large change in the longitudinal flow. The problem is similar to the backward-facing step, with the addition of three-dimensional geometry and the deforming boundary, for which the location must be determined as part of the solution. Currently RANS computations are being performed on the SGI Origin 2000 (195 MHz, 128 processors, 65 GB memory) and the Cray T3E(450 MHz, 816 processors, 200 GB memory). Through the use of parallelization, clock time for a computation for the flow around a combatant has been reduced from 40 hours (one week) to eight hours (overnight). This reduction in clock time makes the computational approach a credible candidate to complement traditional towing tank measurements from the perspective of the ship designer. Other principle new technologies enabling the application of validated computational ship hydrodynamics are the implementation of production methods for measuring the propelled subsurface turbulent flow (LDV) and the free surface temporal deformations (free-surface probe). Today both predictions and measurements have been completed for the propelled flow around the DDG-51 at model scale, and preparations are being made to scale the results to full scale Reynolds number for comparison with at-sea experiments.

A verification and validation workshop in March 1998 produced initial comparisons of high resolution RANS computations and predictions. For the first time, rigorous computations were performed to produce a test matrix for the measurements in the towing tank. This workshop proved instrumental in focusing user attention on the validation process, and served to attract interest from industry in applying the software to new naval ship designs. Recently ONR has increased the intensity of the validation effort in response to a growing need from industry and from Navy evaluators regarding a series of revolutionary new hull forms in which the propulsor and the hull are fully integrated.

These new integrated propulsor/hull configurations are outside of the historical database of information for estimating ship performance. The need is to first develop an understanding of the flow around these ship geometries, and then to build a reliable model database that can eventually be correlated to full scale results. Using traditional towing tank "build and test" scenarios, the process will take decades. Hence there is the need, and opportunity, to develop a numerical complement to the traditional towing tank process. The roadmap presented by Rood (1996b) defines a systematic complementary physical/numerical investigative process for enhancing traditional towing tank evaluations. The process features calibrated computational ship hydrodynamics that complete and extend sparse towing tank data, and provide a means for scaling results. That process has been implemented by ONR, and the progress is outlined, and refinements to the process are described in this paper.

The paradigm that is being established builds on the strategy in the Rood (1996b) paper, and is based on numerical verification, experimental validation, and archival documentation. These three features are combined in a product called the "documented solution". This product is a new addition to the strategy for implementing RANS methods. The documented solution is a meaningful record of the processes to obtain the computational prediction and the experimental validation for a particular geometry and flow condition. No longer is the software, in its entirety, considered to be validated; the concept now is that of a validated solution, the documented solution. Clearly, a large number of successful documented solutions approaches the notion of validated software. In principle the documented solution can be used to "train" persons to apply computational ship hydrodynamics, and can be used as starting points in a design. The proper

balance between numerical and experimental uncertainty in obtaining the validation is obtained by following the guidance of Stern, et al. (1999). The concept of the documented solution appears to be a key factor in the growing acceptance of computational methods to complement traditional towing tank measurements. The user community is willing to entertain documented solutions as a proof of credibility, although there is some concern that it may be an unwarranted extension of the "optimized" software, in which factors are set to produce a solution for a configuration, but which are not applicable to a very wide set of problems.

A team of academic, government laboratory, and shipyard users has been assembled to complete the process of implementing computational ship hydrodynamics as a complement to traditional towing tank measurements for the case of steady flow. The team is being supported by the "ONR Surface Combatant Accelerated Hydrodynamics S&T Initiative". This program has produced a significant change in the preliminary design process for novel ship types. The goal of the program is to produce a set of documented solutions by the end of 2000.

Rood, E.P., "Modern Computational Ship Hydrodynamics: Reynolds-Averaged Navier-Stokes (RANS)", SNAME Transactions, 1996a, (with R. Beck and A. Reed).

Rood, E.P., "Validation Strategy for 'RANS' Computational Ship Hydrodynamics", 2nd International Conference on Hydrodynamics, Hong Kong, 1996b.

Rood, E.P., "Time-Domain Computational Ship Hydrodynamics", Proceedings of the DoD HPCMP Users' Group Meeting, San Diego, 1997.

Rood, E.P., "Time-Domain Computational Ship Hydrodynamics: Features of the Flow Around the DDG-51", Proceedings of the DoD HPCMP Users' Group Meeting, Houston, 1998a.

Rood, E.P., "Transient and Periodic Turbulent Hydrodynamic Flows for Surface Ships: A DoD Challenge Project Milestone", AIAA Paper 98-2931, 1998b.

Rood, E.P., "Complementary RANS and LES Computations for DDG-51 and Transition to DD-21 Acquisition", Proceedings of the DoD HPCMP Users' Group Meeting, Monterey, 1999.

Stern, F., Wilson, R., Coleman, H., & Pāterson, E., Verification and Validation of CFD Simulations, Proceedings of the 3rd ASME/JSME Joint Fluids Engineering Conference, FEDSM99-6913, 1999.

Numerical Ship Hull Optimization

M. Rossetti, D. Peri, E.F. Campana,
INSEAN - Via di Vallerano, 139 - 00128 - Roma (ITALY)

Introduction

In the context of naval hydrodynamics the attempt to automatically modify the shape of a ship hull, according to the response of some optimization scheme, trying to minimize some user defined objective function, has been only very recently performed with the aid of CFD information [2, 3, 4]. Lagrangian-Multiplier methods [1] have been largely used in these optimization algorithms while some authors prefer to implement Conjugate Gradient (CG) algorithms [3] or Sequential Quadratic Programming (SQP) [4]. Although some of these attempts seemed to be encouraging, there is still a lack of experimental verification of the success of the optimization procedure.

In this paper, recently presented in [5], a non-linear constrained optimization problem has been set up and solved on the base of the results obtained via CFD techniques. The non-interactive procedure has been developed to minimize a previously defined objective function related with the flow past a ship moving with steady forward speed in calm water.

Actually, several objective functions can be introduced in the optimization scheme e.g. the total resistance of the ship, the wave pattern generated by its motion, or a combination of both. Different type of geometrical constraints have been also taken into account, in order to obtain a final design which is feasible from the standpoint of construction.

Two strategies, and corresponding algorithms of numerical optimization, namely Sequential Quadratic Programming and non linear Conjugate Gradients, have been examined, and the features of the Variable Complexity Model in speeding up the optimization procedure have been also tested.

During the iterative procedure, the geometry is modified via a Bezier surface, controlled by a restricted number of points acting as design parameters.

The flow solver is based on a free surface linear potential panel code, incorporating a simple flat-plate approximation for the frictional resistance.

Two numerically optimized bow design, obtained with the CG and SQP optimization algorithms, have been developed to reduce total and wave resistance of a tanker ship at a speed of 16 knots.

Obtained numerical results have been validated against experimental data. The two optimized shapes have been tested in the INSEAN towing tank and measured data have been compared with those of the original design, showing the success in the optimization process.

1 Optimization algorithms

1.1 Optimization via SQP

The SQP algorithm [1] allows quadratic convergence for a non linear function subjected to linear and/or non-linear constraints. It solves a problem of the form:

$$\text{minimize} \qquad F(x), \text{ for } x \in R^n,$$

$$\text{subject to} \qquad l \leq \left\{ \begin{array}{c} x \\ A_L x \\ c(x) \end{array} \right\} \leq u,$$

where $F(x)$ is the objective function, x is the vector of the design variables A_L is the matrix of the linear constraints, $c(x)$ is the vector of the non-linear constraint functions, l and u are the lower and upper bounds vectors of constraints.

The search direction p is computed by solving a subproblem of the form

$$\text{minimize } g^T p + \frac{1}{2} p^T H p \quad \text{subject to } \bar{l} \leq \left\{ \begin{array}{c} p \\ A_L p \\ A_N p \end{array} \right\} \leq \bar{u},$$

where g is the gradient of F at the solution x, H is a Quasi-Newton approximation to the Hessian of the Lagrangian function, and A_N is the Jacobian matrix of c evaluated at x.

1.2 Optimization via CG

The conjugate-gradient method assumes that the search direction p at a step k is given by:

$$p_k = -g_k + \beta p_{k-1}$$

where β_k is a scalar quantity to be determined on the basis of the value of the gradient of the objective function and of the line search direction at the previous and current step. Several methods have been tested to compute β (Fletcher-Reeves, Polak-Ribière, Hestenses-Stifel). The results presented in this study are computed via a simple Steepest-Descent ($\beta = 0$) approximation of the CG and are shown in section 5.

2 Objective functions and their evaluation

The choice of a specific objective function is based on the needs of the user. Total resistance or wave resistance may be an easy choice for fluid-dynamicists, although ship designers may be more interested in quantities related to the

engine power or to the manteinance costs. In principle this may be accomplished without difficulties from the optimization algorithm viewpoint.

In the present study, several objective functions have been used to test the capability of the numerical method (total resistance, wave height or a combination of the two). In this paper results for the minimization of the total resistance and wave pattern are presented.

The objective function is computed via a linear potential panel code (WARP) commonly used at INSEAN for standard ship performance evaluation (details may be found in [6]). Frictional forces are evaluated via the ITTC formulation where a local Reynolds number is used for each element on the base of the local panel length and velocity. The total resistance is then given by:

$$R_t = R_w + R_f$$

and the wave pattern is minimized by minimizing:

$$\sqrt{\sum_i \eta_i^2}$$

where η_i is the wave elevation for the i^{th} panel.

3 Modification of hull geometry.

Since viscous effects are taken into account in an extremely simplified manner, the optimization has been restricted to the fore-body geometry below the waterline, including the bulb (shown as the highly refined block in figure 1).

Furthermore, the potential code used in the computation is based on a linearized free surface formulation, and the effect of the geometry above the waterline is not accounted for. However, an optimization of the underwater fore body seems feasible and results have shown realistic improved designs.

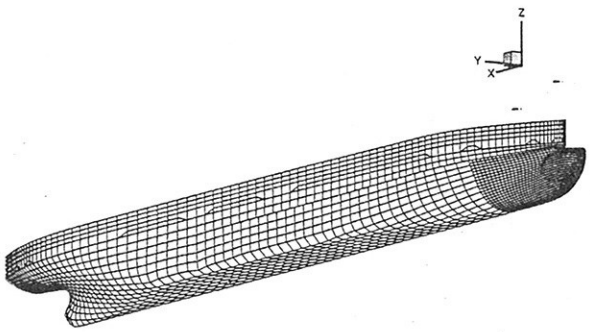

Figure 1: Hull grid showing fore-body optimization block.

Various attempts have been made to develop geometry modification algorithms: some of them acted directly on the grid points [2, 3], while more recently some used perturbation surfaces [4], or B-spline definition of hull geometry [8]. As a result of the numerical procedure, the modified geometry should join the original design without discontinuities and should be generally smooth. The number of design variables should be kept as small as possible to minimize the computations of the objective function gradient. Moreover the algorithm should be as flexible as possible in order to achieve the most number of possible solutions.

The above requirements have been obtained by using a Bezier patch that gradually reduces to a zero level while approaching the unmodified hull shape (figure 2). In this way, geometric continuity between grid boundaries is guaranteed and if the number of control points is kept sufficiently small, realistic geometries can be obtained that do not need major refinements prior to construction.

The patch is controlled by a *Bezier* frame of mxn nodes, which are related to the patch via

$$Y_B(u,v) = \sum_{i=0}^{n} \sum_{j=0}^{m} J_{n,i}(u)\, K_{m,j}(v)\, p_{i,j}$$

where Y_B are the coordinates of the *Bezier* surface, u and v are adimensional parameters along x and z directions, $p_{i,j}$ are the y coordinates of *Bezier* frame nodes and

$$J_{n,i} = \binom{n}{i} (1-u)^{n-i}\, u^i\,, \quad \binom{n}{i} = \frac{n!}{i!(n-i)!}$$

$$K_{m,j} = \binom{m}{j} (1-v)^{m-j}\, v^j\,, \quad \binom{m}{j} = \frac{m!}{j!(m-j)!}$$

The y positions of each control point (three in this example) form the design variables for which an optimum value is searched for. The patch is simply superimposed on the y offsets of the hull to obtain the modified geometry (figure 2) via

$$Y_{H_{mod}} = Y_{H_{orig}}(u,v) + Y_B(u,v)$$

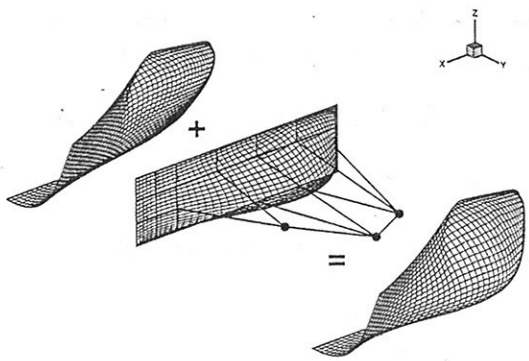

Figure 2: Original geometry (top left), *Bezier* surface (middle) and modified geometry (bottom right).

This procedure has mainly three advantages. Firstly, it is very flexible and it allows to obtain different hull shapes, as the *Bezier* frame can have a different number of control points both vertically and horizontally. Secondly, the number of design variables is kept small and hence the computational effort is minimized, and thirdly the smoothness is guaranteed in both directions.

The main disadvantages are that it may be difficult to apply this method to multi-block grids (at present it can only

be applied to ordered i,j single block grids) and it may be memory hungry. The linear constraints in fact are defined on each node of the hull grid, so there are at least as many constraints as the number of grid nodes. The total number of constraints may further increase as more than one constraint is set an each node, hence increasing the size of the matrix A.

4 Handling geometrical constraints

In order to achieve a realistic geometry, some constraints must be imposed to the possible solutions. These may involve constraints which are both linearly and non-linearly related to the design variables.

Various constraints have been tested during the procedure. The results presented in this paper for both methods linerally constraint the offset to

$$y_{min} \leq y_{new} \leq y_{max}$$

while the keel profile is fixed. To maintain an efficient panel geometry the maximum variation has been restricted to

$$\frac{1}{16} y_{old} \leq y_{new} \leq 2 y_{old}$$

One single non-linear constraint has been employed on the displacement variation $\delta\nabla = \pm 5\%$.

5 Results

The optimization process has been conducted for $F_N = 0.226$. Various runs have been performed with both optimization algorithms: the objective function for the SQP was the total resistance, while SD optimized the wave height. Different set of constraints have been tried which brought to different geometries. Here, for sake of brevity, only the two geometries that have been selected for tank testing are presented (figure 3): one obtained via the Steepest Descent (SD) algorithm, and one obtained via the SQP (from here on 'SD' and 'SQP' will serve to indicate also the two optimized geometries). With reference to the SD algorithm, a simple version of the Variable Complexity Model has been used, that is that part of the function evaluations have obtained by using simpler models, e.g. Double Model panel computation or slender ship theory. The number of design

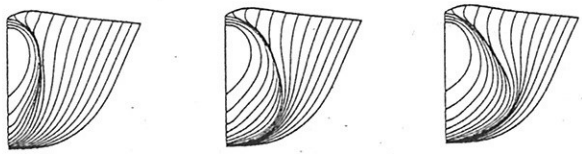

(a) Original (b) SD (c) SQP

Figure 3: Optimized geometries

variables for the two methods are 3x3 and 3x1 respectively. The computed percentage reduction in total resistance is -6.8% (SD) and -5.6% (SQP). The computed result show a general improvement in wave pattern (figure 4): both the second crest and the second through clearly show numerically computed lower values, and this behavior is continued further aft. Experiments follow the same trend for resistance (figure 5) and wave profile (figure 6).

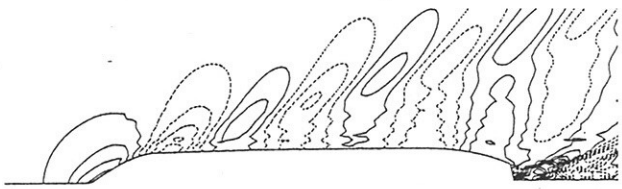

(a) Original

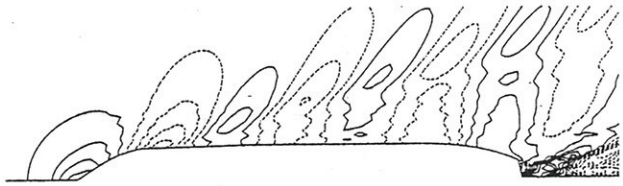

(b) Optimized by SD

(c) Optimized by SQP

Figure 4: Computed wave patterns for the original and the two optimized hulls. $F_N = 0.226$, $\eta/L = -0.010, -0.009, ... + 0.01$.

Table 1 shows the computed quantities with the relative percentage difference form the original. It can be seen that the major reduction is in wave resistance (-14%). The computed C_f is reduced for the SD model, and so its frictional resistance. This is due to the computation of the local

	Orig.	SD	δ%	SQP	δ%
Δ_{ship} (Kg)	19295	19414	0.6	19453	0.8
WSA (m^2)	5.524	5.549	0.5	5.561	0.7
C_w*E+03	2.076	1.779	-14.3	1.773	-14.6
C_f*E+03	3.253	3.199	-1.7	3.254	0.0
R_w (Kgf)	1.366	1.175	-14.0	1.174	-14.1
R_f (Kgf)	2.140	2.114	-1.2	2.155	0.7
R_t (Kgf)	3.167	2.951	-6.8	2.991	-5.6
$R_{t_{exp}}$ (Kgf)	3.00	2.93	-2.0	2.90	-3.0

Table 1: Computed quantities, experimental model resistance and percentage difference. All values refer to the model unless otherwise specifed.

Reynolds number, which permits larger surfaces to have a smaller frictional resistance depending on the values of the local velocities. However, the experimental percentage improvement in resistance is less than the one predicted nu-

merically (2% for the SD model, and 3% for the SQP). A probable reason could be that the calculation of the wetted surface is not sufficiently accurate, a phenomena that has been noted in previous works and reviewed in Larsson *et al.* [7]. Errors in the surface computation lead to inaccuracies in the computation of wave resistance and friction resistance (section 2). Both optimized models have a greater surface than the original, and present larger curvatures (figure 3). For these models therefore the effect of inaccuracy in the surface computation is more evident, being the number of panels the same as the one of the original geometry.

There could also be some effects due to dynamic trim and sinkage. During the optimization process models have been tested in fixed condition (i.e. trim or sinkage not allowed), while in the tank they were tested in free condition. The resistance is usually slightly higher for free condition. A single flow computation has been performed for both SD and SQP geometries with trim and sinkage allowed. Results are shown in table 2. If account is taken for the free condition, the percentage gain in resistance is smaller than in fixed condition (6.4 vs 6.8 for the SD, and 5.1 vs 5.6 for the SQP).

F_N	R_{or}	R_{SD}	$\Delta\%$	R_{SQP}	$\Delta\%$
0.198	2.275	2.161	-5.0	2.206	-3.0
0.226	3.283	3.071	-6.4	3.117	-5.1
0.255	4.880	4.593	-5.9	4.694	-3.8

Table 2: Computed values of resistance allowing trim and sinkage. Dimensions for resistance are Kgf.

As was expected, the gain in resistance is greater at the design speed, for both the numerical algorithms (figure 5). Nevertheless, the optimized shapes perform better than the original one for the whole set of tested velocities.

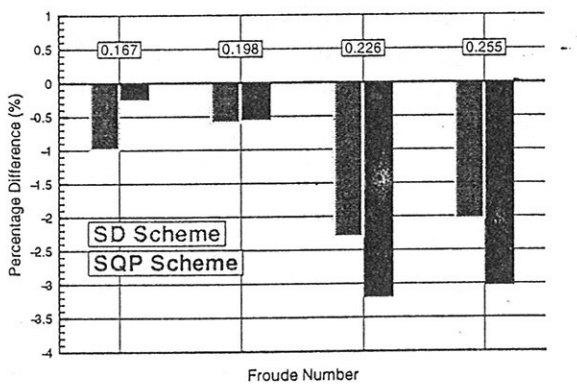

Figure 5: Measured resistance. The major improvement is at the optimization point ($F_N = 0.226$), although there are significant improvements also in other areas.

The experimental resistance of the SQP optimized model is lower than the one of the SD model (table 1), which is in contrast with the numerical predictions. This may be due still to inaccuracies in the computation of the wetted surface and hence wave resistance. The computed wave pattern tends to confirm this: the wave pattern of the SQP model

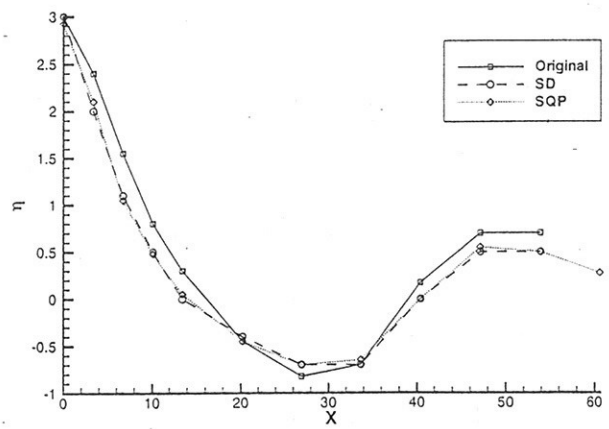

Figure 6: Experimental wave profile, $F_N = 0.226$. The reduction in wave amplitude is 18% (SD) and 21% (SQP).

seems to be slightly better than the one of the SD model (figure 4). This would indicate that the wave resistance for the SQP model is lower than the one for the SD model, an indication that is confirmed by the experiments. Also, because of the linearity in the free surface boundary condition, the positive effect of a reduction in the wave crest (SQP in figure 6) in terms of reduction in frictional resistance is not 'caught' by the code, as the wetted surface is computed only below the waterline.

References

[1] Gill P.E, Murray W. and Wright M.H., (1995) *Practical optimization*, Academic Press.

[2] Janson C., Larsson L. (1996) *A method for the optimization of ship hulls from a resistance point of view.* 21st Symp. on Naval Hydrodynamics, Trondheim.

[3] Wyatt D.C., Chang P.A. (1994) *Development and assessment of a total resistance optimized bow for the AE 36*, Marine Technology, vol. **31**, no. 2.

[4] Tahara Y., Himeno Y. (1998) *An application of computational fluid dynamics to tanker hull form optimization problem*, Third Osaka Colloquium, Osaka.

[5] E.F. Campana, D. Peri, M. Rossetti (1999) *Ships of the optimum shape*, SIAM - OP99, Atlanta, USA

[6] Bassanini, Bulgarelli, Campana, Lalli (1994) *The wave resistance problem in a boundary integral formulation*, Surveys on Mathematics for Industry, vol. **4**.

[7] Larsson L., Regnström B., Broberg L., Li D-Q, Janson C-E (1998) *Failures, Fantasies and Feats in the Theoretical/Numerical Prediction of Ship Performance*, 22nd Symp. on Naval Hydrodynamics, Washington D.C.

[8] Leer-Andersen M., Larsson L. (1999) *Non-interactive optimization of hull shapes with regard to minimizing wash wave height*, HIPER'99, Zevenwacht.

NUMERICAL SIMULATON OF VOITH-SCHNEIDER CYCLOIDAL SHIP PROPELLERS

M. Schuster, R. Schilling
Technische Universität München
Institute and Laboratory for Hydraulic Machinery and Plants
D-85748 Garching
Germany

SUMMARY

The flow through cycloidal ship propellers is characterized by three-dimensional highly turbulent patterns due to constantly changing kinematic boundary conditions. The locally varying acceleration of the rotor blades requires the numerical simulation approach to handle a rather complex computational domain. Part of the boundaries are moving in space and their accurate representation is essential to ensure a fully conservative computational procedure. The approach presented uses the integral form of the Navier-Stokes equations for an arbitrarily moving control volume. Special care is taken to also satisfy the space conservation law. For turbulence modeling the Smagorinsky subgrid scale model is implemented, where van Driest damping is employed in the near wall regions. To solve the equation system the widely used SIMPLE algorithm is applied to a collocated variable arrangement. The numerical domain is split into twelve subdomains and the computation is performed parallel on eight processor units. Two given test cases were simulated and showed good agreement with experimental data.

INTRODUCTION

Ships operating at special conditions involving safety of people, environmental issues or transportation of hazardous goods demand for propulsion systems providing a maximum of manoevrability. In this respect cycloidal propeller represent intelligent drive systems combining propulsion and steering in a single system.

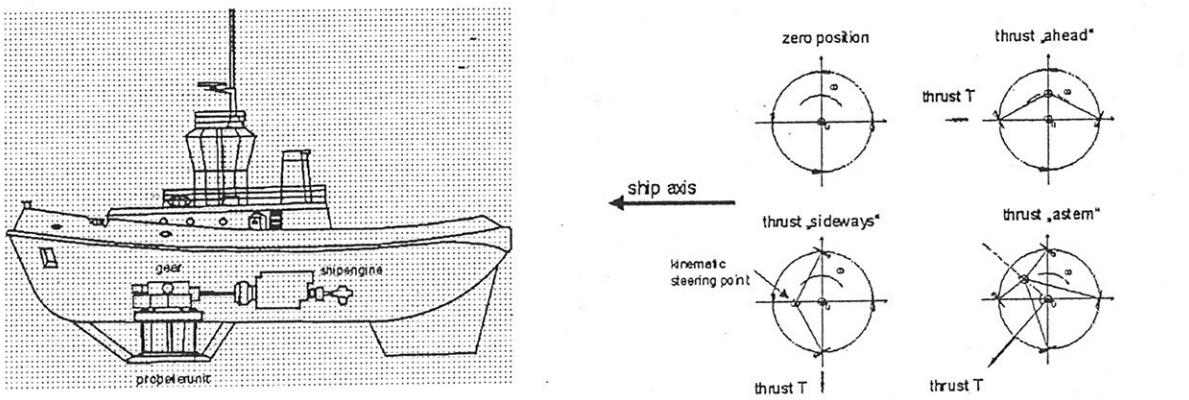

Figure 1: Sketch of a Water Tractor with cycloidal propeller and steering kinematics

For this kind of propeller a number of hydrofoils is rotated on a vertical axis, where their angles of attack during every revolution can be pivoted from 0 degrees to positive and again back to negative values. The direction of the zero position and the deflection of the hydrofoils can be varied in a fashion that precise and continuous thrust variation within 360 degree can be obtained; see fig. 1.

PROBLEM FORMULATION

In order to describe the incompressible fluid flow in moving coordinates, the integral form of the conservation law for space, mass, and momentum is used. For an arbitrarily shaped domain of the volume V bounded by a closed surface S the governing equations can be written as

$$\frac{d}{dt}\int_V dV - \int_S \mathbf{c}_n d\mathbf{S} = 0, \qquad (1)$$

$$\frac{d}{dt}\int_V \rho\, dV - \int_S \rho(\mathbf{c}-\mathbf{c}_n) d\mathbf{S} = 0, \qquad (2)$$

$$\frac{d}{dt}\int_V \rho\,\mathbf{c}\, dV - \int_S \rho(\mathbf{c}-\mathbf{c}_n)\mathbf{c} + p\mathbf{I} - \left(\mu\, grad\,\mathbf{c} + (grad\,\mathbf{c})^T\right) d\mathbf{S} = \int_V \mathbf{s}_c\, dV, \qquad (3)$$

where ρ represents the fluid density, $\mathbf{c}$ the fluid velocity, μ the dynamic viscosity, p the pressure, $\mathbf{I}$ the unit tensor, $\mathbf{c_n}$ the net velocity, and $\mathbf{s_c}$ the volumetric source term of momentum.

Special care is taken to also satisfy the space conservation law, eq. 1, which ensures a fully conservative computational procedure. Fully implicit temporal differencing makes the method stable for any time step. By applying the finite volume approach, the discretization of the convection and diffusion fluxes is carried out in a collocated variable arrangement. For the computation of mass fluxes through the faces of the control volumes the values of the velocity components at the face centers have to be determined. To avoid oscillations that may result from simple linear interpolation, a special interpolation practice is employed, as proposed by Khosla and Rubin [1] and implemented by many authors as Bauer [2], Orth [3], and Perić [5]:

$$F^{n+1} = F_L^{n+1} - \beta\left(F_H - F_L\right)^n \qquad (4)$$

F_L stands for an interpolation of a lower order scheme (e.g. "upwind") and F_H is a higher order approximation. The term in the brackets is calculated from values of a previous iteration, as indicated by the superscript 'n'. Its contribution to the implicit part is usually small, so this explicit treatment does not impair the convergence rate significantly. Multiplying the term in the brackets by the blending factor β regulates the explicit and implicit contribution. The use of this "Deferred Correction Scheme" damps oscillations and improves the diagonal dominance of the coefficient matrix. The coupling of pressure and velocity is performed via the SIMPLE algorithm. The use of the collocated variable arrangement on non-orthogonal grids demands the algorithm to be slightly modified. Here, a pressure-velocity coupling method for complex geometries, proposed by Majumdar [4] and Perić [6], has been implemented, where an additional pressure gradient term is subtracted from the velocity correction; see Ritzinger [7].

TURBULENCE MODELLING

For the computation of the turbulent flow and the reduction of computational cost with respect to a required, very fine temporal resolution of 10^{-5} s per time step, the commonly used Smagrorinski subgrid scale model (SGS) is applied. In this approach the SGS stress τ_{ij} is related to the resolvable velocity field by an eddy viscosity model, $\tau'_{ij} = -2\nu_T S_{ij}$, where the

large-scale strain tensor S_{ij} is defined by

$$S_{ij} = \frac{1}{2}\left(\frac{\partial \bar{u}_i}{\partial x_j} + \frac{\partial \bar{u}_j}{\partial x_i}\right) \qquad (5)$$

The subgrid scale eddy viscosity can be derived by dimensional arguments as

$$\nu_T = (C_S \Delta)^2 \sqrt{2 S_{ij} S_{ij}}\,, \qquad (6)$$

where Δ represents the filter length scale and C_s is the Smagorinski model parameter. This can be obtained by equating the subgrid-scale production and the dissipation in homogenous turbulence as shown by Pourquié [9]. The major advantage of this model is the use of an algebraic formula to calculate the eddy-viscosity from the resolved velocity field and therefore enables an efficient numerical procedure. In order to ensure the correct limiting behavior of the SGS stresses close to solid boundaries van Driest damping is introduced:

$$C_S = C_{S0}\left(1 - \exp\left(\frac{-y^{+}}{A^{+}}\right)\right)^2, \qquad (7)$$

where $y^{+} = y u_\tau / \nu$, $u_\tau = \sqrt{\tau_W / \rho}$, and τ_W denotes the shear stress at the wall. As mentioned by Ferziger [8] this modification is difficult to justify in the context of large-eddy simulation. However, it has proven to produce reasonable results in many application; see Perić [8] and Nagy [2].

BLOCK STRUCTURE AND PARALLELIZATION

To handle the complex geometry of the cycloid propeller the computational domain was split into twelve structured grid blocks; see fig. 2. Apparently the chosen approach of spatial domain decomposition is strongly governed by the geometry of the solution domain. Depending on available system resources a single subdomain, or optional, more than one grid

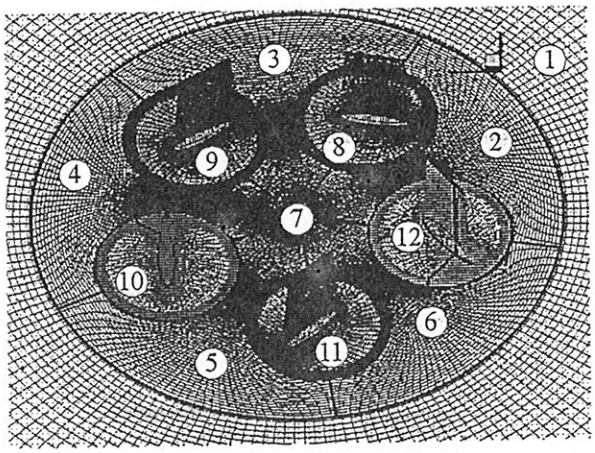

Figure 2: Decomposition of the propeller domain

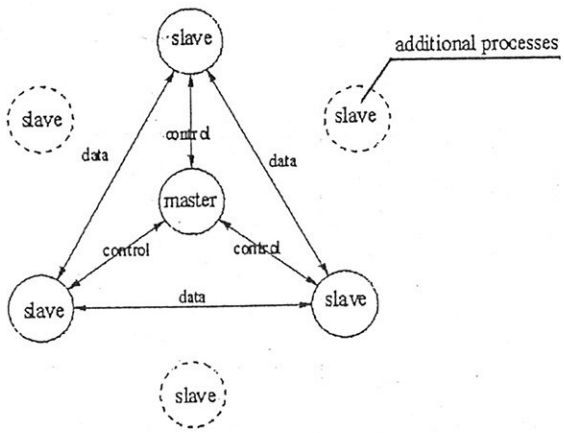

Figure 3: Data flow management of the Master-Slave concept

block may be assigned to one processor. Every block is represented by its own "Slave" process performing the flow calculation and exchanging boundary data with their adjacent neighbors. All Slaves are supervised by an "Master" process that only coordinates and

controls essential parameters, such as residuals and convergence criteria; see fig. 3. The data flow between the Slave processes essentially accounts for the communication cost of the parallelization. The control data exchange between Master and Slave processes plays a minor role. Especially, if the communication rate is high, the routing of the data will have a significant impact on the overall computational performance. Processes exchanging considerable amounts of information are favorably located on multi processor boards. This way the intercommunication will be directed via the internal bus system and thus considerably less time consuming than the data exchange via network cards and ethernet wires. Therefore, both proper process assignment and data stream routing are crucial to obtain a maximum of efficiency.

APPLICATION

This work focuses on the simulation of a five blade Voith-Schneider model propeller. To evaluate the presented approach two computed test cases were to be compared to measurements with respect to quantity and direction of the propeller's thrust:

test case 1: rpm n = 250 min^{-1}, pitch p = 0.56, advance $\lambda = 0.00$
test case 2: rpm n = 250 min^{-1}, pitch p = 0.78, advance $\lambda = 0.70$

The computations were performed on 4 Dual Pentium II 300 MHz PCs with a grid resolution of approximately $1{,}2 \cdot 10^6$ points. This provided detailed information about the distribution of pressure and velocity in the field. For both test cases the temporary pressure distribution in the field is depicted in fig. 5. Stream traces computed from the temporary flow field illustrate the nature of the two different points of operation. In case of the propeller operating with no advance complex three dimensional vortex structures seem to be shedding from the trailing edges of the hydrofoils as demonstrated in fig. 5a. When operating with an advance of $\lambda = 0.70$ these vortex structures seem to be suppressed and eventually vanish.

The unsteady integral values for the quantity and the direction of the thrust are plotted against time. All quantities exhibit periodically alternating behavior. As shown in fig. 6 thrust and its direction oscillate by a frequency of 20 Hz that corresponds to the frequency of the rotating propeller body times the number of hydrofoils attached. The mean value of each oscillation is located within the error range of its corresponding measured mean value. Therefore, the computed results are found to be in good agreement with the model measurements.

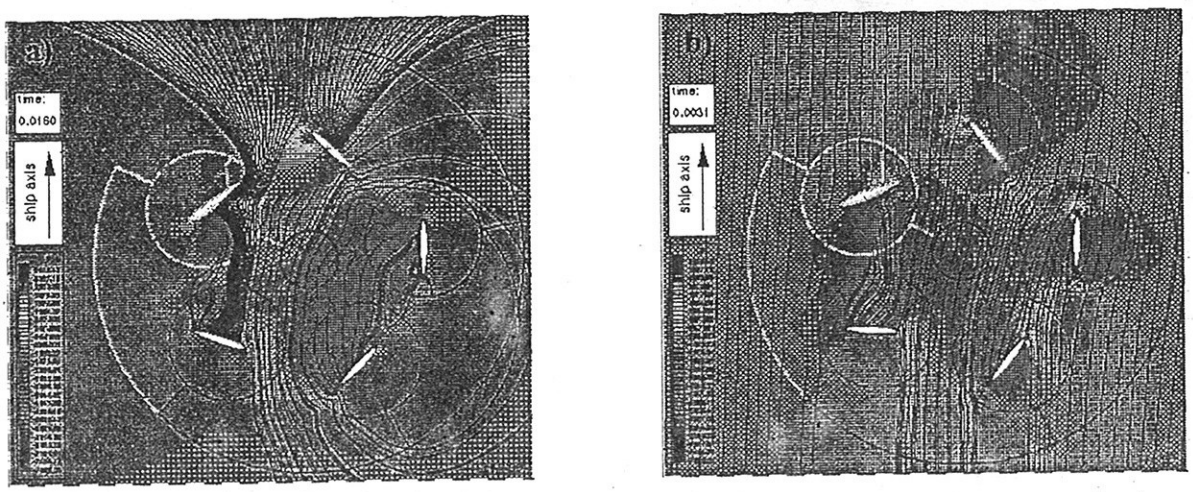

Figure 5: Stream traces of flow around the hydrofoils and contour plot. a) test case 1 – no advance b) test case 2 - advance $\lambda = 0.70$

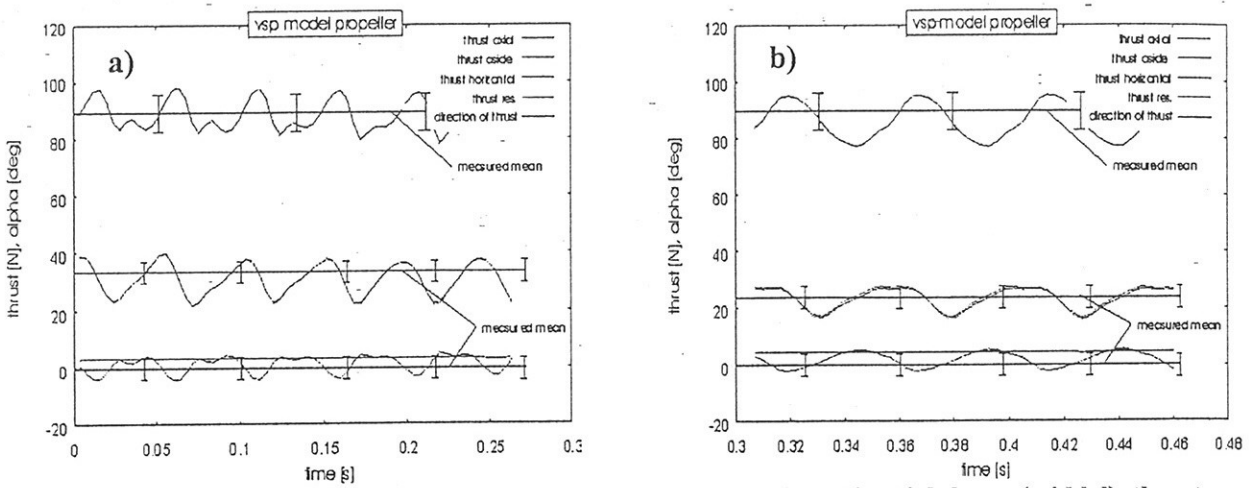

Figure 6: Computation of integral quantities – thrust angle (upper), axial thrust (middel), thrust sideways (lower), and horizontal thrust (lower flat) . a) test case 1 b) test case 2

CONCLUSION

The results of this study state that the finite volume approach presented allows the simulation of the flow through cycloidal ship propellers with sufficient accuracy for design and optimization purposes. A comparison of the computed characteristics with measurements shows good overall agreement with the trends. Due to the constantly changing flow conditions in the domain a comparatively expensive SGS turbulence model was chosen. By requiring a considerably high grid resolution this approach causes a significant computational effort. However, block structuring and parallelizing the task allowed to solve the flow problem on comparatively inexpensive Pentium processor units within a reasonable time. With respect to steadily increasing computer performance the concept presented should be further refined to simulate highly complex flow structures.

REFERENCES

[1] Khosla, P.K, Rubin S.G.: A diagonally dominant second-order accurate implicit scheme. Computers Fluids. Vol. 2, 207-209, 1974

[2] Bauer, H.J.: Überprüfung numerischer Ansätze zur Beschreibung turbulenter ellptischer Strömungen in komplexen Geometrien mit Hilfe konturangepaßter Koordinaten. Dissertation. Fakultät für Maschinenbau, Universität Karlsruhe, 1989

[3] Orth, A.: Mehrgittermethode zur Berechnung inkompressibler, stationärer Strömungen mit krummlinigen Berandungen. Dissertation, Fakultät für Bauingenieur und Vermessungswesen, TH Karlsruhe, 1991

[4] Majumdar, S.; Rodi, W.; Zhu, J.: Three-Dimensional Finite Volume Method for Incompressible Flows with Complex Boundaries. Transaction of the ASME, Vol. 114, 496-503, 1992

[5] Perić, M.; Scheurer, G.: CAST – A Finit Volume Method for Predicting Two-Dimensional Flow and Heat Transfer Phenomena. GRS Technische Notiz SRR-89-01, September 1989

[6] Perić, M.; Ferziger, J.H.: Computational Methods for Fluid Dynamics. 2. Aufl. Berlin Heidelberg New York: Springer Verlag, 1997

[7] Ritzinger, S., Simulation realer Laufradströmungen, Dissertation. Fachbereich Maschinenwesen, TU München, 1997

[8] Ferziger, J.H.: Large Eddy Simulation: An Introduction and Perspective. In O. Metais, J. Ferziger (eds.), New Tools in Turbulence Modelling. Berlin Heidelberg: Springer Verlag, 1997

[9] Pourquié, M. J. B. M.: Large-Eddy Simulation of a Turbulent Jet. PhD thesis. Delft University, 1994

[10] Nagy, T. K.: Large Eddy Simulation of Turbulent Plane Couette Flow. Masters Thesis. Norwegian Institute of Technology, 1997

Unsteady Wash Computation for a High Speed Vessel

Hironori YASUKAWA, *Nagasaki Experimental Tank, Mitsubishi Heavy Industries**

Introduction

Waves generated by a high speed vessel often influence the facilities of the port. To know the influences, it is necessary that the propagation and deformation of the waves are simulated including effects of the port bank and the sea bottom.

As the 1st step of the study on the simulation of the unsteady wash, the waves generated by the vessel with decelerated motion from constant speed in the towing tank are numerically analyzed. This is the similar situation to the wave propagation in the process that the vessel reduces the speed at the port. For the analysis, so-called the Mixed Eulerian-Lagrangian (MEL) method is adopted. Time domain analyses using MEL method have been carried out, for instance, by Qi and Mori(1989), Maskew(1991), Beck et al.(1993) and Li and Chwang(1997). However, the existing MEL method may not be suitable for simulating the wave propagation in long time since the computational time is too much at present.

To reduce the computational time, we employ the following techniques:

1. Basic equations: 2nd order non-linear free surface conditions are employed for reducing the computational time.
2. Time integration: a scheme based on Newmark's β method is used for keeping the robustness.
3. Matrix solver: a kind of iterative solver SOR method is used for quick matrix computation.
4. Panel arrangements: constant rectangular panels of free surface fixed in space is employed. The method presented by Nakatake and Ando (1996) is adopted for simplicity of the free surface treatment.

The unsteady wash generated by the high speed vessel in the towing tank was realistically demonstrated.

Basic Equations

Let us consider the numerical towing tank with the water depth h. The vessel in the tank is assumed to move with the speed $U(t)$ which varies as the function of time t. The coordinate system fixed in the space is employed. The x-axis is defined as direction from the ship stern to the bow, y-axis to port and z-axis vertically upward. The $x-y$ plane is the still water surface.

The perturbation velocity potential due to ship moving in the tank is defined as $\phi(x,y,z,t)$. Then, ϕ has to fulfill the following boundary conditions as:

$$\frac{\partial \phi}{\partial t} = -g\zeta - \frac{\partial^2 \phi}{\partial t \partial z}\zeta - \frac{1}{2}\left\{\left(\frac{\partial \phi}{\partial x}\right)^2 + \left(\frac{\partial \phi}{\partial y}\right)^2 + \left(\frac{\partial \phi}{\partial z}\right)^2\right\} \quad \text{on } z = 0 \tag{1}$$

$$\frac{\partial \zeta}{\partial t} = \frac{\partial \phi}{\partial z} + \frac{\partial^2 \phi}{\partial z^2}\zeta - \frac{\partial \phi}{\partial x}\frac{\partial \zeta}{\partial x} - \frac{\partial \phi}{\partial y}\frac{\partial \zeta}{\partial y} \quad \text{on } z = 0 \tag{2}$$

$$\frac{\partial \phi}{\partial n} = -U(t)n_x \quad \text{on } S_H \tag{3}$$

*3-48 Bunkyo-Machi, Nagasaki 852-8131, JAPAN, email: yasukawa@ngsrdc.mhi.co.jp

$$\frac{\partial \phi}{\partial n} = 0 \quad \text{on } S_W \tag{4}$$

The 2nd order non-linear free surface conditions expanded with respect to ζ, which means the wave height, around $z = 0$ are employed, eqs.(1) and (2). Eq.(3) is the boundary condition on the wetted hull surface at the still water S_H, and eq.(4) the boundary condition on the tank wall S_W.

Applying Green's theorem, the velocity potential ϕ is expressed as:

$$\alpha\phi(P) = -\iint_{S_H+S_F+S_W} \left[\frac{\partial \phi(Q)}{\partial n_Q} - \phi(Q) \frac{\partial}{\partial n_Q} \right] G(P;Q) dS \tag{5}$$

where

$$G(P;Q) = \frac{1}{\sqrt{(x-x_1)^2 + (y-y_1)^2 + (z-z_1)^2}} + \frac{1}{\sqrt{(x-x_1)^2 + (y-y_1)^2 + (z+z_1+h)^2}} \tag{6}$$

Here, $P = (x, y, z)$ is a field point and $Q = (x_1, y_1, z_1)$ the source point. α is a constant. S_F denotes the still water surface ($z = 0$). The 2nd-term of the right hand side of eq.(6) is the additional term to fulfill the bottom surface condition.

Numerical Scheme

The time integration with respect to the potential ϕ and wave height ζ are performed using Newmark's β scheme. The flow of the computation is as follows:

1. $\phi_t^{(k)}$ and $\zeta_t^{(k)}$ at k-th time step are assumed as $\phi_t^{(k)} = \phi_t^{(k-1)}$ and $\zeta_t^{(k)} = \zeta_t^{(k-1)}$
2. The approximate values of $\phi^{(k)}$ and $\zeta^{(k)}$ at k-th time step are calculated using these formulae:

$$\phi^{(k)} = \phi^{(k-1)} + \Delta t/2 \left(\phi_t^{(k-1)} + \phi_t^{(k)} \right) \tag{7}$$

$$\zeta^{(k)} = \zeta^{(k-1)} + \Delta t/2 \left(\zeta_t^{(k-1)} + \zeta_t^{(k)} \right) \tag{8}$$

   Here, Δt denotes the time interval.

3. ϕ on $S_F (z = 0)$ and ϕ_n on $S_H \& S_W$ are given from eq.(7) and the boundary conditions, respectively. Solving the matrix made by discretizing the eq.(5), $\phi_z^{(k)}$ on S_F and $\phi^{(k)}$ on $S_H \& S_W$ which are unknown values are obtained. The matrix was solved using a kind of iterative solver SOR method with under relaxation for quick computation.
4. The derivatives with respect to ϕ and ζ on S_F are numerically calculated from the values obtained.
5. The $\phi_t^{(k)}$ and $\zeta_t^{(k)}$ are calculated from the free surface conditions eqs.(1) and (2).
6. The $\phi_t^{(k)}$ and $\zeta_t^{(k)}$ obtained at step 5 is compared with the $\phi_t^{(k)}$ and $\zeta_t^{(k)}$ assumed at step 1. If remarkable difference between them is observed, the values at step 1 are replaced to those at step 5. And going back to step 2, this procedure is repeated until obtaining the converged solution. If obtaining the converged solution, a time step is added to the original k.

Computation

Computations are carried out for high speed vessel shown in Table 1. As the region of the numerical towing tank, $30L$ for the length, $3.2L$ for the half breadth and $100L$ for water depth are assumed. For computation on the half side, 2,400 panels for free surface, 240 panels for the vessel and 1,820 panels for the tank walls are used. The constant rectangular panels of the free surface fixed in space are used. Further, the method presented by Nakatake and Ando (1996) is adopted for simplicity of the matrix computation with respect to the free surface.

The vessel length L is assumed to be 1.0m in the computations. The vessel speed changes as the function of time in the computations as follows: the vessel accelerates from the rest, reaches constant speed F_n=0.638 after 1.0s, and runs with the constant speed until 9.0s. The speed reduction starts at 9.0s, and the vessel completely stops at 10.0s. The computation is continued until 20.0s. Time interval 0.025s is used in the computation.

Fig.1 shows the propagation of the waves generated by the vessel in the towing tank from 6s to 14s. Typical Kelvin wave pattern can be observed in the computations at 6s and 8s. At 10s, shift of the waves generated by the vessel to up stream starts just after stopping the vessel. Also the waves reflected by the tank side wall are remarkable at the rear region of the vessel. The bow-shape waves observed in front of the vessel propagate up stream (See the results at 12s and 14s). The wave length of the bow-shape waves is about $2.5L$ which roughly agrees with that of Kelvin waves generated by the vessel. There is a possibility that the up stream propagating waves which are generated when the vessel reduces the speed at the port influence the facilities of the port. The unsteady wash generated by the high speed vessel in the towing tank was realistically demonstrated.

At the workshop, I will present the comparison with the model experiments for verification of the present method.

Table 1: Principal dimensions of high speed vessel

L/B	7.50
B/d	4.58
C_b	0.45
$100\nabla/L^3$	0.175

References

Beck, R.F., Cao, Y., and Lee, T.-H.(1993): *Fully Nonlinear Water Wave Computations using the the Desingularized Method*, 6th International Conference on Numerical Ship Hydrodynamics, Iowa City.

Li, D. and Chwang, T. (1997): *Time Domain Analysis of Ship-Generated Waves in Harbour using a Fast Hierarchical Method*, 7th International Offshore and Polar Engineering Conference, Honolulu.

Maskew, B. (1991): *A Nonliner Numerical Method for Transient Wave/Hull Problems on Arbitrary Vessel*, SNAME Trans., Vol.99.

Nakatake, K. and Ando, J. (1996): *Rankine Source Method using Rectangular Panels on Water Surface*, 11th Workshop on Water Waves and Floating Bodies, Hamburg.

Qi, X. and Mori, K. (1989): *Numerical Simulation of 3-D Nonlinear Water Wave by Boundary Element Method – In the case of submerged bodies –*, J. of the Society of Naval Architects of Japan, Vol.165.

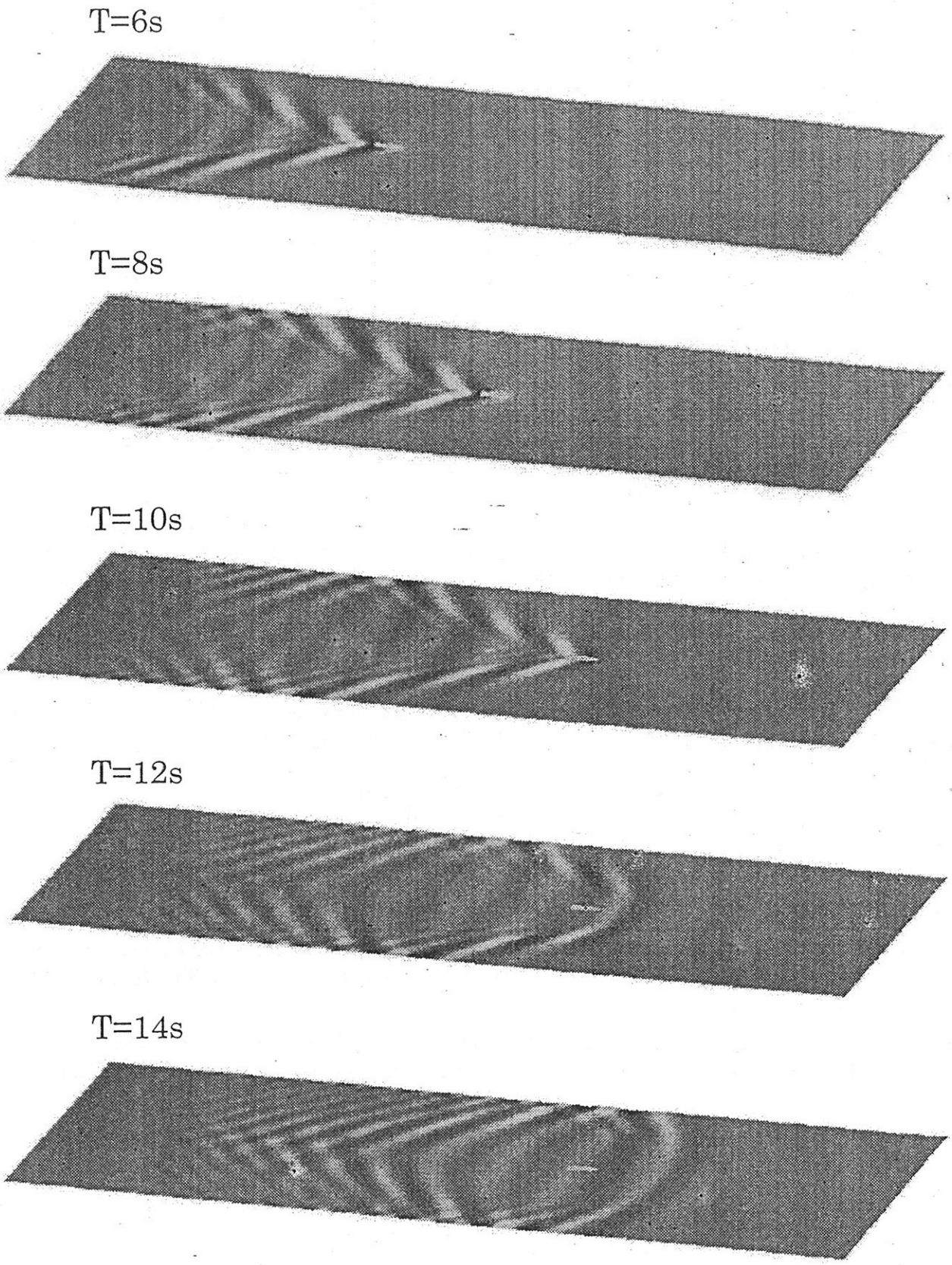

Fig.1 Propagation of the waves generated by high speed vessel in towing tank

3rd NUMERICAL TOWING TANK SYMPOSIUM (NuTTS'2000)

Tjarno and Gothenborg, Sweden, 10-13 September 2000

SPONSORED BY THE EUROPEAN COMMISSION UNDER THE TMR PROGRAMME

Topics:
- Nonlinear flows around marine structures (LES, RANSE, Euler with or w/o free surface)
- Free-surface flows around marine structures (3-d ship seakeeping, free-surface viscous flows)
- Related topics (validation experiments, numerical techniques, etc)

Deadlines:	Early feedback:	30 May 2000
	Abstracts received:	30 June 2000
	Notification of acceptance:	7 July 2000

Free of charge for eligible citizens of the EC and associated countries. Eligible are all citizens of Norway and Israel 35 years of age or younger and accepted as researchers or students in the field by the organiser. Preference of scholarships will be given to participants of former NuTTS events.

The event is supported by WEGEMT (www.wegemt.org.uk) and directly before the the Gothenburg'2000 workshop (www.iihr.uiowa.edu/gothenburg2000).

You are invited to participate in the above event. The objective of the event is to provide a forum for informal discussions among experts in the field and to disseminate latest results. Younger workers and Ph.D. students are especially encouraged to participate. We also encourage female colleagues to take an active role in the symposium.

The abstracts of the proposed talk will be directly reproduced in the proceedings. There will be no final full papers. Rather, the symposium is intended to give 'sneak previews' to full papers. Work in progress, encountered problems, etc. should be discussed in an open, informal atmosphere among colleagues.

The first page of the extended abstract should be headed with the title and authors' names and address in a compact form to economise on space. Extended abstracts should be limited to 4 pages in a field 17cm by 25cm per page. Copies of the extended abstract should be sent in good quality to the host.

The event will be held in a remote training facility in beautiful natural surroundings. Bus transport will organised on 10 and 13 September from/to Gothenborg. All participants stay and have meals together to maximize interaction and discussion. Participants may have to share double rooms due to limited availability of housing.

Prospective participants should fill in the attached form and return it to the host. An early reply will help us in organising the event better. For the early feedback, a tentative title or topic will suffice.

Volker Bertram, TUTECH, Lammersieth 90, D-22305 Hamburg, Germany
bertram@schiffbau.uni-hamburg.de
www.schiffbau.uni-hamburg.de/IFS/AB/AB-3-14/towtank2.html

Participants

Mustafa Abdel-Maksoud	maksoud@sva-potsdam.de
Giorgio Amati	g.amati@caspur.it
Marco Barcellona	marco@pcins1.insean.it
Volker Bertram	bertram@schiffbau.uni-hamburg.de
Frode Bloch	frode.bloch@upr.vickersmarine.com
Riccardo Broglia	r.broglia@insean.it
Ulderico (Paolo) Bulgarelli	upbulga@rios6.insean.it
Emilio Campana	e.campana@insean.it
Mario Caponetto	rolla-sp@bluewin.ch
Shiu-Wu Chau	chau@scorpio.usddc.org.tw
Andrea Colagrossi	andreac@rios13.insean.it
Giorgio Contento	contento@univ.trieste.it
Agostino De Marco	agodemar@unina.it
Andrea DiMascio	a.dimascio@insean.it
Fabricio D'Este	deste@univ.trieste.it
Bettar El Moctar	elmoctar@schiffbau.uni-hamburg.de
Paola Gualeni	gualeni@dinav.unige.it
Dieke Hafermann	dh@hsva.de
Haavald Holm	hholm@marin.ntnu.no
Alessandro Iafrati	a.iafrati@insean.it
Hidetsugu Iwashita	iwashita@naoe.hiroshima-u.ac.jp
Jacob Jensen	JSJ@oedan.dk
Maurizio Landrini	surfer@rios3.insean.it
Claudio Lugni	lugni@rios10.insean.it
Eric v. Maarel	H.T.M.v.d.Maarel@marin.nl
Federico Massaioli	f.massaioli@caspur.it
Jerzy Matusiak	Jerzy.Matusiak@hut.fi
Jennifer McDonald	MCDONAJL@ONR.NAVY.MIL
Marco Mulas	mulas@crs4.it
Roberto Muscari	roberto@rios11.insean.it
Sergio Parisi	sergio@pcins1.insean.it
Daniele Peri	d.peri@insean.it
Iain Robertson	i.robertson@ic.ac.uk
Ed Rood	roode@ONR.NAVY.MIL
Michele Rossetti	m.rossetti@insean.it
Martin Schuster	schuster@ibm13.lhm.mw.tu-muenchen.de
Fabricio Sessa	fabsessa@unina.it
Spencer Sherwin	s.sherwin@ic.ac.uk
Antonio Traverso	Antonio.Traverso@cetena.it
Hironori Yasukawa	yasukawa@ngsrdc.mhi.co.jp